UNIVERSITY OF THE WEST of SCOTLAND

Simulations and Experiments of the Nonlinear Behaviour of Acoustically Induced Flow Fields in High-Intensity Discharge Lamps

Jörg Claus Schwieger

A thesis submitted in partial fulfilment of the requirement of the University of the West of Scotland for the degree of Doctor of Philosophy

School of Engineering

April, 2016

Content of the thesis is partially published (in chronological order):

J. Schwieger, B. Baumann, M. Wolff, Arc shape of high-intensity discharge lamps: Comparison of simulation and experiment, 17^{th} *ICPPP*, Suzhou, China (2013)

J. Schwieger, B. Baumann, M. Wolff, F. Manders, J. Suijker, Influence of thermal conductivity and plasma pressure on temperature distribution and acoustical eigenfrequencies of high-intensity discharge lamps, *COMSOL Conf.*, Rotterdam, Netherlands (2013)

B. Baumann, J. Schwieger, M. Wolff, F. Manders, J. Suijker, Numerical investigation of symmetry breaking and critical behavior of the acoustic streaming field in high-intensity discharge lamps, *arXiv*, 1412.7032 (2014)

B. Baumann, J. Schwieger, M. Wolff, F. Manders, J. Suijker, 3D acoustic streaming field in high-intensity discharge lamps, *COMSOL Conf.*, Cambridge, UK (2014)

J. Schwieger, M. Wolff, B. Baumann, F. Manders, J. Suijker, Characterization of discharge arc flicker in high-intensity discharge lamps, *LS14*, Como, Italy (2014)

M. Wolff, J. Schwieger, B. Baumann, Optical characterization of photothermally induced arc flicker in high-intensity discharge lamps, 3^{rd} *IWPPP*, Erice, Italy (2014)

J. Schwieger, B. Baumann, M. Wolff, Arc shape of high-intensity discharge lamps: Simulation and experiment, *Int. J. Thermophys.*, 36(5):1327-1335 (2015)

J. Schwieger, M. Wolff, B. Baumann, F. Manders, J. Suijker, Characterization of discharge arc flicker in high-intensity discharge lamps, *IEEE Trans. Ind. Appl.*, 51(3):2544-2547 (2015)

B. Baumann, J. Schwieger, M. Wolff, F. Manders, J. Suijker, Numerical investigation of symmetry breaking and critical behavior of the acoustic streaming field in high-intensity discharge lamps, *J. Phys. D: Appl. Phys.*, 48(25):255501 (2015)

J. Schwieger, B. Baumann, M. Wolff, F. Manders, J. Suijker, Backcoupling of acoustic streaming on the temperature field inside high-intensity discharge lamps, *arXiv*, 1506.01507 (2015)

B. Baumann, J. Schwieger, M. Wolff, F. Manders, J. Suijker, Critical behaviour of the acoustic streaming field in HID lamps, 27^{th} *Int. NNV Symp. Plasma Phys. & Rad. Technol.*, Lunteren, Netherlands (2015)

J. Schwieger, B. Baumann, M. Wolff, F. Manders, J. Suijker, Backcoupling of acoustic streaming on the temperature field inside high-intensity discharge lamps, *Proc.* 33^{rd} *UIT Heat Trans. Conf.*, L'Aquila, Italy (2015)

J. Schwieger, B. Baumann, M. Wolff, F. Manders, J. Suijker, Backcoupling of acoustic streaming on the temperature field inside high-intensity discharge lamps, *J. Phys.: Conf. Ser.*, 655:012045 (2015)

B. Baumann, J. Schwieger, M. Wolff, F. Manders, J. Suijker, Nonlinear behavior in high-intensity discharge lamps, *arXiv*, 1510.03236 (2015)

B. Baumann, J. Schwieger, M. Wolff, F. Manders, J. Suijker, Nonlinear behavior in high-intensity discharge lamps, *J. Phys. D: Appl. Phys.*, pending publication (2016)

Abstract

High-intensity discharge (HID) lamps comprise a gas encapsulated in a transparent vessel, in which a light-emitting discharge arc is established. The lamp operation necessitates a driver that provides an energy-saving and cost reduction potential when the frequency of the alternating current is tuned from the commonly used low frequency range (50 Hz to 400 Hz) to a higher frequency range (20 kHz to 500 kHz).

However, such an operation can result in low frequency luminous fluctuations, lamp extinction or even destruction. The excitation of acoustic resonances in the high frequency range are the reason for the instable behaviour. The standing pressure waves induce forces with non-zero time average that arise from the bulk viscosity of the plasma. This so-called acoustic streaming effect generates a superimposed fluid flow, which associates the high frequency resonances to the low frequency flicker.

A stationary, three-dimensional finite element model of the arc tube of an HID lamp has been developed to investigate the light flicker phenomenon. The multiphysical model comprises the conservation of mass, momentum, energy as well as charge and incorporates the acoustic streaming effect to determine its influence on the fluid velocity, the temperature and the electric field.

Initially, the discharge arc under stable conditions has been simulated. The results have been compared with complementary, experimental investigations that measured the light intensity distribution and the electric potential drop. The inclusion of acoustic streaming in the simulation reveals a significant change of the flow field inside the vessel. The velocity field suffers a phase transition to an asymmetrical state at a critical acoustic streaming force. Furthermore, the simulations and the accompanying experiments show a jump phenomenon and a hysteresis that are similar to those of a Duffing oscillator with a softening spring. The results of the model and the experiment are in good accordance.

The model is able to predict at which frequencies light flicker can be expected. The results enable a considerably better understanding of the flicker phenomenon in HID lamps and facilitate the development of energy-efficient drivers.

Contents

List of Figures

List of Tables

Acknowledgement

I would like to express my great appreciations to my supervisor at the University of the West of Scotland, Klaus Spohr, who guided me throughout the entire process of the PhD program and gave me the opportunity to carry out this work.

Particularly, I would like to thank Bernd Baumann and Marcus Wolff of the University of Applied Sciences Hamburg for their advice and suggestions as well as for sharing their extensive knowledge with me. Their engagement in various matters and the fruitful discussions were valuable for the interpretation of the results and the quality of this work.

Freddy Manders and Jos Suijker were constantly interested in the progress of my work, always supported me with their expertise in many discussions and contributed to diverse solutions. Thank you for your help.

I am grateful to my colleagues from the Heinrich Blasius Institute for their continuous support, in particular to Henry Bruhns for his invaluable organisational help through the whole duration of the project.

I also like to thank the German Federal Ministry of Education and Research that has funded the research project under the reference number 03FH025PX2.

Furthermore, I thank the team of the graduate school and all doctoral students that have been supportive towards the entire course of my study, academically and beyond.

Last but not least I would like to thank my family, as without their constant encouragement, none of this would have been possible. I can always count on them, under any circumstances and in any situation I come across.

Declaration

No portion of this work referred to in this thesis has been submitted in support of an application for another degree or qualification to the *University of the West of Scotland* or any other university or institute of learning.

Nomenclature

a	prefactor
A	acoustic pressure amplitude
$\mathscr{A}$	excitation amplitude
c	speed of sound
c_i	degree of freedom
c_p	specific heat capacity at constant pressure
c_0	speed of light
d	perpendicular distance to the tube wall
d_{wall}	tube wall thickness
D	normalised damping coefficient
$\vec{E}$	electric field
$\vec{f}$	volume force
f_{ex}	excitation frequency
F	excitation force amplitude
g	gravitational acceleration
h	Planck's constant
H	time-dependent source term
$\mathscr{H}$	power density of heat generation
i	imaginary number
I	electric current
$\mathbf{I}$	identity matrix
$\vec{j}$	electric current density field
J_0	electric current density
k	Boltzmann constant
k_0	damping coefficient
k_1	linear spring constant
k_3	cubic stiffness parameter

K	modulus of compression
$\hat{l}$	loss factor correction term
l_{char}	characteristic length
L	acoustic loss
m	mass
M	molar mass
$\vec{n}$	normal vector
p	pressure
P	static pressure
P_{lamp}	nominal electric lamp power
$\vec{q}$	conductive heat flux
q_{rad}	radiation loss
Q	heat source
R	molar gas constant
$\mathscr{R}$	residual
R_{plasma}	electric resistance of the plasma
R_{spec}	specific spectral emission
s	exponential decay function
S	control parameter
$\mathbf{S}$	strain rate tensor
S_{c}	interior arc tube surface
S_{cc}	current-carrying surface
t	time
T	temperature
$\vec{u}$	fluid velocity
$\vec{v}$	sound particle velocity
V	electric potential
V_{c}	interior arc tube volume
w	weight function
x, y, z	Cartesian coordinates
x_0	static amplitude
$\hat{x}$	amplitude of oscillation
y_N	shape function
α	modulation depth
β	cubic stiffness parameter of Duffing oscillator
γ	heat capacity ratio

δ	boundary layer thickness
δ_{ij}	Kronecker symbol
ε	emissivity
ζ	critical exponent
η	dynamic viscosity
ϑ	tilt angle
κ	thermal conductivity
λ	wavelength
ρ	mass density
ρ_c	electric charge density
σ	electric conductivity
σ_{SB}	Stefan-Boltzmann constant
τ	time-scale
$\boldsymbol{\tau}$	viscous stress tensor
Φ_i	linear shape function
Φ	order parameter symmetry
Ψ	order parameter velocity
ω	eigen angular frequency
Ω	relative excitation frequency

Abbreviations

AC	alternating current
AR	acoustic resonance
AS	acoustic streaming
CAD	computer aided design
CMH	ceramic metal halide
CMOS	complementary metal-oxide-semiconductor
CRI	colour rendering index
DC	direct current
FEM	finite element method
FFT	fast Fourier transform
HDR	high dynamic range
HID	high-intensity discharge
LED	light-emitting diode
LTE	local thermal equilibrium

PCA	polycrystalline alumina
UV	ultraviolet
YAG	yttrium aluminium garnet

Chapter 1

Introduction

The quality of life in today's societies essentially depends on the availability of artificial light. In the working, living and leisure area, light sources enable an extensive independence on daytime and season of the year. Currently, approximately 30 to 33 billion electric light sources are daily operated that convert almost 20 % of the globally generated electric power into light [1–3]. Therefore, a significant potential exists to lower the energy consumption because already small efficiency improvements to current technologies result in substantial energy savings. Furthermore, the CO_2 emission of 550 million tons per year, that is identical to 70 % of the pollution of worlds passenger cars, could be reduced, or at least the growth could be diminished [3].

Beside these ecological factors, the quality of the generated light plays an important factor. Improvements of the energy efficiency of light sources should not impair the light quality. The variety of lamp types on the market offers luminaires for diverse application areas. By taking economical, ecological and qualitative effects into account, the best suitable light source can be chosen because each lamp type possesses a competitive advantage.

Visible light of electric lamps is generated by means of different phenomena that are systematized in Figure 1.1. Argon-tungsten and tungsten halogen lamps belong to the conventional lamps. In these lamps, a heated tungsten filament radiates incandescent light. When the wire is encapsulated in an argon atmosphere, higher operating temperatures and, therefore, higher efficiencies are achieved compared to a tungsten wire in an evacuated bulb because the inert gas retards the evaporation of tungsten [4]. A chemical reaction of iodine or bromine in a tungsten halogen lamp reattaches evaporated tungsten back onto the filament. This

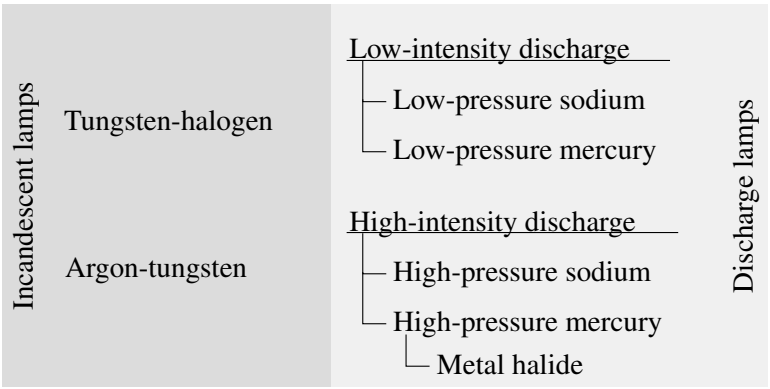

Figure 1.1. Classification of incandescent and discharge lamps [3].

enables operation at higher temperatures and leads to luminous efficacies of up to $33\,\mathrm{lm\,W^{-1}}$ [3]. The luminous efficacy is the ratio of the luminous flux, which is a measure of the perceived light of the human eye, to the electrical input power. The luminous efficacy of $33\,\mathrm{lm\,W^{-1}}$ corresponds to an electrical-to-visible conversion efficiency of approximately 5 %.

Low-intensity discharge lamps are filled with an inert gas and, additionally, contain trace elements of sodium and/or mercury. The electric current inside the glass tube establishes a low-intensity arc that emits ultraviolet (UV) light. The UV radiation excites the phosphor, that is deposited as a layer on the inner wall of the tube, and is converted into the visible wavelength range by fluorescence. To ignite the lamp and limit the electric current during normal operation, a driver is required. Linear fluorescent lamps reach a maximal luminous efficacy of $104\,\mathrm{lm\,W^{-1}}$ [3]. Its diffuse light is widely used for illumination of offices as well as in the retail and industrial sector [5]. The low-pressure sodium lamp attains a luminous efficacy of up to $200\,\mathrm{lm\,W^{-1}}$, which is the highest value of all artificial light sources [3]. The major drawback of these lamps is their poor colour rendering index (CRI) that is zero or even negative [3]. The CRI of an illuminant measures its ability to display the true colours of an object. The sun is used as a reference object with a defined CRI of 100. Hence, the colour of objects illuminated by low-pressure sodium lamps appears unnatural.

High-intensity discharge (HID) lamps include high-pressure sodium and high-pressure mercury lamps. These light sources emit visible radiation by energy exchanges of excited atomic states in a discharge arc. HID lamps are characterised by a static pressure inside the lamp that exceeds the ambient pressure during steady-state operation. The main constituent of the discharge arc distinguishes the sodium

from the mercury lamp. Additionally, these lamps usually contain metal halides to improve the light quality. Metal halide lamps are further divided into quartz metal halide and ceramic metal halide (CMH) lamps dependent on the tube material that envelops the discharge arc. The investigations in this work focus on a CMH type lamp, the *Philips* MASTERColour CDM-T Elite 35 W/930. The typical luminous efficacy of CMH lamps with a power under 150 W is 90 $\mathrm{lm\,W^{-1}}$ to 110 $\mathrm{lm\,W^{-1}}$, whereas special research lamps show luminous efficacies of up to 150 $\mathrm{lm\,W^{-1}}$ [6,7]. Compared to low-pressure sodium lamps, the colour appearance of CMH lamps is sunlike. Hence, these lamps reach a CRI of 95 to 98 [1,6–8].

HID lamps serve as illuminant in many applications. These lamps represent a considerable fraction of artificial light sources. In 2006, 25 % of the global electric-lighting energy was converted into light with HID lamps [3]. HID lamps combine high lumen output levels with high colour qualities. Therefore, these light sources are perfectly suitable for illumination of large outdoor areas like streets, car parks and stadiums as well as for indoor applications like industrial spaces, warehouses and retail spaces. These lamps are preferred for automotive headlight lamps as well as for television and film production because of the emitted neutral white light. The replacement of quartz with ceramic wall material allows miniaturisation of HID lamps down to 20 W and, consequently, enables substitution of halogen lights used for spot lighting in the retail sector. High power HID lamps, that are used as UV radiator for curing of ink and plastics or for water purification, are operated at 35 kW [9].

The main advantage of CMH lamps towards all other artificial light sources is their sunlike luminance [8]. These lamps can be build in compact size because of the short discharge arc. The light can easily be focused, which makes them suitable for optical systems. However, a bulky driver is necessary to ignite and operate the lamp at stable conditions. The electrical-to-visible conversion efficiency of commercially available lamps ranges from 35 % to 40 % [6]. In laboratory, a conversion efficiency of over 50 % could be reached with the aid of the arc straightening effect [7]. Additionally, the efficiency of 91 % to 97 % of the control gear has to be considered [7,10]. Moreover, these lamps have a long rated lifespan of typically 20 000 h [1,8,11] and are qualified for operation under adverse temperature conditions because the CMH lamp performance is relatively temperature-insensitive [3,12].

Drawbacks of HID lamps are the long start-up phase from ignition to full light level and the long cool-down phase [3]. Prior to re-ignition, the majority of metal

halides in the lamp has to condense to restart the plasma generation because the electron capture process can significantly increase the ignition voltage [13]. Additionally, the power of HID lamps cannot be completely dimmed, and the CRI as well as the luminous efficacy decrease in part load [3,10]. The diffusion of chemical species inside the arc tube of a vertically operated lamp in combination with the convection flow can cause axial demixing of the species [14–18], but this undesirable effect only occurs at direct current (DC) or low-frequency alternating current (AC) operation [19]. Demixing leads to unequally distributed light emission and results in colour separation and a lower CRI [17]. The convection flow itself originates from the gravitational force and local differences of the mass density inside the arc tube. The unevenly distributed temperature in horizontally operated lamps results in two negative effects: (1) overheating of the upper wall shortens the lifetime, and (2) the low temperature in the lower part decreases the vaporisation of metal halides [20]. Since discharge arcs for lighting are operated in closed vessels, acoustic resonances (AR) can be excited during AC operation. These resonances lead to light fluctuation, arc instability and arc tube explosions in the worst situation. In case of a lamp failure and when these lamps are not properly disposed, the mercury can be released into the environment.

For some years, the efficiency and light quality of light-emitting diodes (LED) has been rapidly developed so that these lamps revolutionise the global lighting market. When the p-n junction diode is operated in the forward direction, electrons and electron holes can recombine and release photons. The wavelength of the irradiated photons depends on the semiconductor material and its doping. The invention of the GaN diode, that emits blue light and was recently awarded with the Nobel Prize in Physics [21], facilitates production of white-light LEDs and considerably accelerated introduction of LEDs into the lighting market. The luminous efficacy currently reaches approximately $123\,\mathrm{lm\,W^{-1}}$ for warm white and $159\,\mathrm{lm\,W^{-1}}$ for cool white light in commercially available LEDs [22] and above $200\,\mathrm{lm\,W^{-1}}$ in research lamps [22,23]. The CRI is currently 92 [24]. Both characteristics have dramatically improved over the last 30 years and will be enhanced in the foreseeable future [22,25].

The superior luminous efficacy, long lifetime, natural colour rendition and low costs of discharge lamps were the reason for these illuminants to be the first choice for many applications. In the last years, the supremacy of discharge lamps ceased. In all aspects, LEDs are currently on the same level or are even advantageous compared to discharge lamps. Therefore, the market share of illumination solutions

with LEDs will further increase.

Nevertheless, the sunlike luminance, the compact size and the high colour quality of HID lamps will guarantee a market for these lamps in the future. Moreover, the supply of replacement lamps for existing lighting systems will maintain a worthwhile market. In the product life cycle concept, HID lamp systems evolve to the mature stage. This means that cost becomes the key focus of many development activities and that drivers for operating HID lamps are optimised to cheaper designs. Minimal driver costs and an increased efficiency can be achieved by operating the lamp at an AC with a frequency of approximately 300 kHz [26], but in this frequency range ARs, that lead to arc flickering, are particularly distinctive.

An alternative way to increase the efficiency of the established technology has been recently discussed in the literature [7,27]. Instead of avoiding operation in frequency regions in which ARs occur, the discharge arc can be excited in a way that it is stabilised. The excitation of specific acoustic modes results in flow fields inside the arc tube that counteract the convection flow in a horizontally operated lamp. The convection flow originally bends the discharge arc in opposed direction of gravitation, whereas the acoustically induced, counteracting flow straightens the arc. Simultaneously, the flow field can serve to reduce demixing of chemical species inside the arc tube. With the aid of this effect, conversion efficiencies of over 50 % can be obtained [7].

Furthermore, this arc straightening effect is particularly interesting with regard to mercury-free HID lamps. The mercury in the arc tube provides a sufficiently high electric resistance to keep the voltage drop over the short electrode distance at a constantly high level. In the high pressure and high temperature environment, the mercury vapour possesses the smallest electric conductivity of all suitable alternatives. Additionally, the small heat conductivity of the mercury minimises the heat losses. To relinquish mercury in HID lamps, it is therefore necessary to increase the electrode distance and, hence, to provide a sufficiently high electric resistance. When zinc instead of mercury is used, estimations have shown that an enlargement of the electrode distance by 25 % is required [28]. However, an enlargement leads to a longer discharge arc and, consequently, to a destabilisation of the arc. The arc straightening effect can counteract this destabilisation by inducing a stabilising flow.

The next chapter starts with a description of the investigated HID lamp. The function principles of the lamp components are outlined, and the light-emitting

plasma is defined and classified. Additionally, the function of the driver and its operating strategies are presented. Subsequently, the problem of acoustically induced discharge arc instabilities and influences thereon are addressed. The current state of research summarises experimental findings and simulation results on this problem that were discussed in the past. Chapter 2 ends with the detection and definition of the research gap and addresses the questions that arise from the gap.

In Chapter 3 the mathematical description of discharge arc physics, which is necessary to calculate the temperature field inside the arc tube, is presented. The concept of local thermal equilibrium (LTE), a method to describe the plasma in HID lamps, is introduced. Then, an approach to determine the acoustic pressure inside the arc tube is demonstrated. It solves the inhomogeneous wave equation with the aid of loss factors. The equations, used to simulate the acoustic streaming (AS) field that causes the discharge arc movements, are also given. Finally, the mathematical description of bifurcations and instabilities as well as the theoretical background of the Duffing oscillator is presented because the results of the simulations and the experiments (Chapter 5) show a bifurcating flow field, when it is acoustically excited. Additionally, strong similarities to the Duffing oscillator are detected.

The physical coefficients describing the behaviour of the plasma, the electrodes and the arc tube wall are presented in Chapter 4. Moreover, the experimental setup is explained, and the finite element method (FEM) as well as the simulation model are outlined. The experimental setup enables electric detection of frequency regions, in which the discharge arc behaves instable. Furthermore, an optical system is incorporated to record images of the discharge arc during stable and instable operating conditions. The model description covers the geometry simplifications, the boundary conditions and the finite element mesh. The simulation steps required to calculate the physical field variables in the case of a stable discharge arc and in the case of the acoustically excited arc are presented as well.

Chapter 5 presents the results of the simulations and the experiments. These are compared and discussed. The chapter is divided into five sections: The first section shows simulation results at stable operating conditions that are verified by accompanying experimental investigations. In the second section, AR frequencies and the acoustic response function are determined. The third section presents results of a sensitivity analysis. The fourth section demonstrates the impact of AS on the velocity field inside the arc tube, and the final section describes the backcoupling of this field on the temperature and other fields.

Finally, Chapter 6 summarises, discusses and concludes the results and provides suggestions for future work.

Chapter 2

High-Intensity Discharge Lamp

2.1 Function Principle

High-intensity discharge lamps belong to the electric gas discharge lamps. Figure 2.1 shows its setup and schematically depicts the discharge arc when the lamp is operated horizontally. In this lamp position, an upward bending of the discharge arc is induced because the buoyancy force leads to an upward directed fluid flow in the centre of the arc tube. The light is emitted by means of a discharge arc established between two electrodes. On the electrode surface, the electric current is transmitted from the electrode to the plasma. Pure tungsten is used as electrode material because it has a better lumen maintenance and a lower voltage rise over lifetime compared to thoriated tungsten electrodes [12]. The lumen maintenance is the ability to maintain the lumen output over the lamp lifetime; its inverse is called the lumen depreciation.

The discharge arc and the electrodes are encapsulated in a refractory envelope called arc tube. In case of the investigated low-wattage lamp, the tube is made of translucent polycrystalline alumina (PCA). Lamps with this ceramic material can continuously be operated at wall temperatures of over 1500 K, whereas lamps with quartz walls are limited to operation up to 1300 K [29]. Moreover, colour shifting over lifetime due to salt losses and high lumen depreciation are drawbacks of quartz walls as well [10]. The PCA enables construction of vessels with small sizes that follow the natural contour of the arc more closely so that the luminous efficacy could be increased. Mechanical, thermal and chemical issues prevent the use of yttrium aluminium garnet (YAG) as wall material for commercially available lamps [29]. YAG is only used for research purposes of optical measurements due

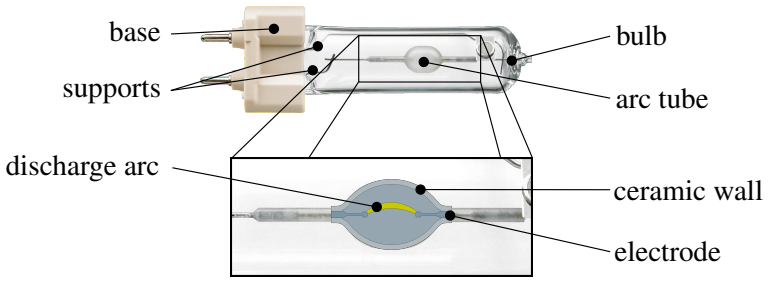

Figure 2.1. Setup of a low-wattage HID lamp (*Philips* MASTERColour CDM-T Elite 35 W/930).

to its transparency [30,31].

A gas inside the arc tube facilitates ignition of the lamp because it reduces the required breakdown voltage. After ignition, the initial discharge is heated up to temperatures at which the other ingredients of the arc tube evaporate [32]. The inert gas argon is used in the investigated 35 W lamp. The main ingredient in the lamp is mercury. Its partial pressure is 2.4 MPa at an absolute pressure of 2.8 MPa inside the arc tube when it is operated at its nominal power. Mercury decreases the electric conductivity and, therefore, increases the voltage drop between the electrodes and lowers the electric current. This results in typical voltage drops of 90 V to 100 V [3]. Furthermore, the high electric field strengths diminish the electrode erosion because the ion bombardment is reduced [32], which results in longer lamp lifetimes [33]. Therefore, mercury is also called buffer gas [34].

Light emissions of metal salts in the discharge fill the gaps in the visible spectrum of the mercury discharge to improve the light quality [32,35]. Pure metals would require very high plasma temperatures to work efficiently because they possess high vapour pressures. Therefore, metal halides, usually iodides, with a reduced vapour pressure compared to pure metals are used [29,32]. Some of these elements lead to an arc widening and others to an arc constriction [13,36]. Moreover, the halides are less aggressive to the envelope material [29,33]. Sodium-, thallium-, calcium- and cerium-iodine are included in the investigated lamp. Its temperature-dependent composition is presented in Section 4.2 and especially in Figure 4.2.

The volume between the arc tube and the outer bulb (see Figure 2.1) is evacuated to avoid diffusion of impurities, especially hydrogen, into the arc tube and to increase the temperature stability [4]. The outer bulb itself is a barrier for the UV radiation that is emitted by the discharge. The support structure positions the arc

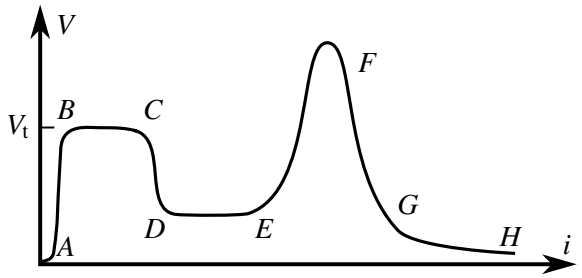

Figure 2.2. Current (i) voltage (V) characteristic of gas discharges [37].

tube in the centre of the outer bulb and connects the electrodes with the base.

Figure 2.2 qualitatively shows the correlation of the electric current and the voltage for different discharge types. The gas discharges are divided into different regions: (A) non-self-sustaining discharge, ($B-C$) Townsend dark discharge, ($D-E$) normal glow discharge, ($E-F$) abnormal glow discharge, ($F-G$) transition to arc and ($G-H$) discharge arc. V_t describes the electric potential for self-sustaining discharges. Low-intensity discharge lamps are operated in the region of glow discharge ($D-E$). Their relatively low electric current induces a weakly ionised gas in a non-equilibrium state because the electron temperature is much higher than the gas temperature [38]. Discharges in the region ($G-H$) are typically operated at high currents of 10^{-1} A to 10^5 A and low voltages of several tens of volts [37]. HID lamps are operated at these conditions. In combination with the high pressure, the plasma reaches thermodynamic equilibrium. Thus, the temperature of electrons and heavy species coincide (see Section 3.1).

Discharge arcs essentially differ from glow discharges in the mechanism of electron emission from the cathode. In the glow discharge, incident positive ions hit the cold metal surface of the cathode and induce the emission of electrons. This phenomenon, called secondary emission, is only important at ignition of discharge lamps [20]. During steady operation, the high current heats the cathode to approximately 3000 K so that a high current results from the intense thermionic emission [37]. To ignite the lamp, a special discharge ignition technique is required, e.g. a high voltage pulse. After the ignition phase, the discharge immediately becomes self-sustaining. Higher electric field strengths are necessary at the cathode than in the centre of the discharge arc to ensure the transition of the current into the plasma [39]. The required power is not converted into light [40]. The power in the discharge arc is transformed into ionisation, excitation or dissociation of plasma atoms or molecules and heat [38].

An electronic driver, also called ballast, is necessary for the operation of discharge lamps. It provides a high voltage of usually more than 2 kV to ignite the lamp and re-ignite the plasma each half-cycle if the lamp is driven by an alternating current [3,41]. Furthermore, a ballast is required because of the negative current-voltage characteristics of discharge arcs [41–43]: When the electric current slightly increases, a lower lamp voltage is needed to maintain the input power. The original voltage would be maintained without a driver so that the input power would increase [38] leading to light extinction or even lamp explosion.

Various operating strategies for the driver exist: DC drivers do not excite ARs inside the arc tube (see Section 2.2), but struggle with the cataphoretic effect [44,45]. This effect describes the motion of positively charged particles under an electric field so that particles with the same charge accumulate. This results in an undesired colour separation inside the arc tube. Low frequency AC drivers, that operate at frequencies of 50 Hz to 400 Hz [32], avoid the cataphoretic effect, but have low system efficiencies and are bulky [26]. High frequency AC operation requires knowledge of the frequency regions, in which AR driven arc instabilities occur. Very high frequency AC drivers operate at over 500 kHz [32], a frequency region in which ARs are dampened, but these drivers have high switching power losses [44,46,47]. Compared to DC drivers, AC operation diminishes demixing of the ions in the plasma [14–17,48,49] and reduces electrode erosion [44]. Other drivers make use of the power spectrum spreading control, that prevents excitation of ARs by operating below the power threshold necessary for an acoustic excitation [50,51]. Furthermore, a smart driver, that contained information about frequency ranges in which stable operation is possible, was tested [52].

Nowadays, low frequency electromagnetic drivers are used for commercial HID lamp operation [51]. Predominantly, square-wave instead of sine-wave drivers are used because of the lower material costs for the electric components [26,53,54]. A significant cost reduction, a reduced size and weight as well as a slightly improved efficiency can be achieved by operating these lamps on high frequency electronic drivers [42,44,55] or by increasing the high frequency current ripple superimposed on the basic square-wave current. The conversion efficiency of the high frequency electronic gear is 91 % to 97 % [7,10]. To minimise the costs of the driver components, the lamp should be operated at a frequency of approximately 300 kHz [26], but at this frequency it struggles with AR driven instabilities.

2.2 Acoustic Instabilities

Movements of the discharge arc are caused by the excitation of standing pressure waves inside the arc tube that result from periodic heating when operated at an AC. Therefore, these discharge instabilities are also called acoustic instabilities. If the discharge arc is acoustically excited, depends on the pressure distribution of the acoustic eigenmode so that arc movements cannot be detected at every acoustic eigenfrequency.

The shape of the discharge arc in the HID lamp depends on many factors: Arc tube geometry, electrode distance, absolute pressure inside the arc tube, type and amount of metal halides, mounting position, input power, etc. These factors influence the arc constriction, the arc length, the temperature distribution, the acoustic eigenmodes and their corresponding frequencies as well as many other physical fields. To increase the light quality and the conversion efficiency from electric power to visible light, the lamp can be operated at higher halogen pressures. However, this results in constricted arcs that are more susceptible to acoustic instabilities.

The tube wall serves to stabilise the discharge arc. When the arc position changes, the temperature gradient increases on one side while decreasing on the opposite side. This higher temperature gradient leads to an increased heat loss so that the discharge is cooled down and moves back to its original position [13]. Therefore, discharge arcs in HID lamps are also called wall-stabilised discharge arcs.

The previous chapter stated that the operation of HID lamps with a high frequency AC is advantageous with regard to energy efficiency, cost, weight and size of the electronic driver. However, operation at certain AC frequency ranges bears the risk of stimulating acoustic instabilities in the arc tube. Due to the Joule heating, a time-dependent heat source emerges in the plasma that is zero at zero-crossing of the electric current and maximal at the peak of the electric current. It generates acoustic waves that propagate through the arc tube. As the tube is finite, the acoustic waves are reflected at the walls, and the reflected waves interfere with the primary wave. Standing pressure waves are established at a resonance frequency. The phenomenon is called acoustic resonance (AR). The resonances can induce arc movements at low frequencies of approximately 10 Hz [56,57]. The time delay between electric excitation of a resonance and onset of AR instabilities for outdated HID lamps and for high power lamps is between 10 ms and 1 s [9,58]. Modern HID

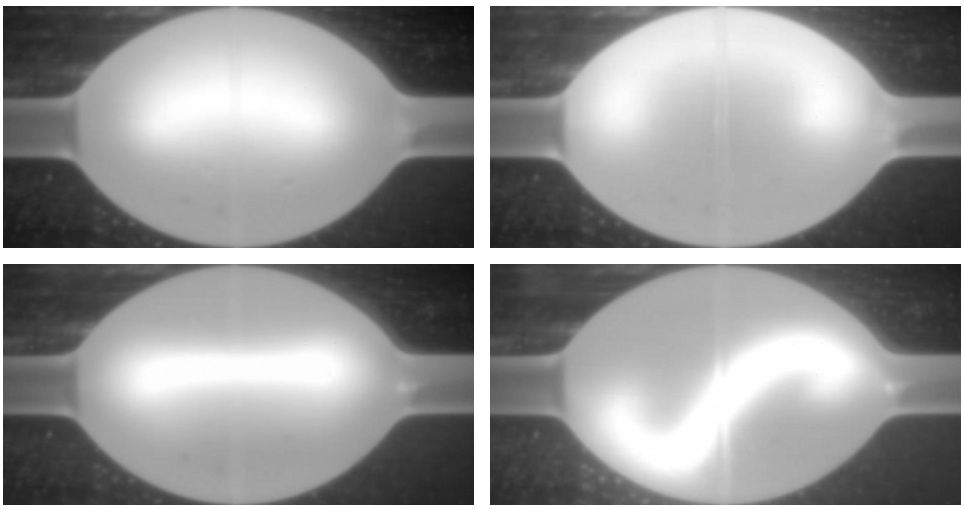

Figure 2.3. Brightness distributions during arc flicker of a horizontally operated lamp at four time instances.

lamps with a nominal power of 70 W show an onset time shorter than 1 ms [59]. Figure 2.3 exemplary shows four discharge arc positions during such an acoustic instability. These movements are associated with light intensity fluctuations. The discharge arc at the top left shows the arc under stable operating conditions. The distributions were measured with the experimental setup described in Section 4.4.

At stable operating conditions, only the gravitational force acts on the arc tube content. A fluid flow in the upward direction is caused by buoyancy. A straight arc can be observed without gravity [60]. When the AC frequency is tuned to an AR frequency, the AS phenomenon induces an additional force. The fluid flow and the temperature field change and alter the AR frequency. Then the operation frequency and the AR frequency differ, the AS force diminishes, and the discharge arc returns to its original position due to the wall-stabilising effects [61]. In this way, the AS phenomenon links the high frequency excitation signal to the low frequency flicker phenomenon [57,61]. A different AS force arises at each acoustic eigenfrequency. At some AR frequencies, the AS force is not strong enough to change the discharge path [61].

The frequency ranges, in which the discharge arc behaves instable, as well as the strengths of the instabilities depend on the lamp characteristics. Even differences in the acoustic eigenfrequencies caused by manufacturing tolerances, that lead to slightly different arc tube geometries and plasma compositions, were detected [43,52,62–64]. Therefore, the shape of the arc tube can be modified to

shift the AR frequencies or to reduce the strength of instabilities [58]. Furthermore, the lamp age influences the acoustic instabilities. The voltage drop between the electrodes of an aged lamp increases and, simultaneously, the electric current decreases to preserve a constant lamp power [65]. Some experimental measurements at lamps of different age show no significant shift of the acoustic eigenfrequencies [43,65,66], whereas others claim that the lamp age affects the resonance frequencies because the plasma composition and the electrodes change over time [44,52,55]. The AR frequencies in dimmed HID lamps shift to lower frequencies because the reduced input power leads to a temperature decrease [67].

2.3 Current Research on Acoustic Instabilities

More than 50 years ago, the first observations of arc instabilities in discharge lamps were reported [68,69]. These reports state that acoustic pressure waves inside the lamp cause arc instabilities. The observations lead to the hypothesis that standing acoustic pressure waves are the reason for the behaviour. This was supported by theoretical calculations because the switching frequency of the DC power supply in the experiment coincided with calculated acoustic eigenfrequencies. For the calculations, the homogeneous Helmholtz equation (see Section 3.2.1) in cylindrical coordinates subject to appropriate boundary conditions was solved [68,69]. In the last decades, research on the instability phenomena in discharge lamps focused on investigations of resonance frequencies, but the physical connection between the pressure waves and the light intensity fluctuations remained vague. In 2008, it was stated that the acoustic streaming phenomenon could link both processes [57,61]. Therefore, current research on acoustic instabilities in HID lamps focusses on the AS effect.

The AR phenomenon in HID lamps was experimentally investigated by many different detection methods. The simplest method, a visual inspection by eye, observed light intensity deviations and arc position changes of a vertically operated and, therefore, straight discharge arc [70]. To quantify the visual inspection, a simple optical system was proposed that observes the discharge arc from two sides [41]. A broadband photodiode measured the light intensity. The difference of this time-dependent photodiode signal with and without acoustic excitation is presented [41]. A photodiode measurement also enables the definition of a flicker level [71]. A more detailed optical investigation of resonances observed the discharge arc from two sides with 16 photodiodes in total [55,72]. When an HID lamp

is driven by a band-limited white noise signal and the emitted light is measured by a broadband photodiode, the AR frequencies can be determined by the optical response [73,74]. This technique can be applied to discharge lamps with a nominal power of 35 kW [9] and also works with pink noise [27]; an input signal with a frequency that is inversely proportional to the intensity of the signal.

Measurements of the electric power [62], the electric current [42,75], the voltage drop between the electrodes [43,71] and the electric resistance [52] enable quantification of acoustic instabilities as well. These four electric parameters are listed in ascending order with regard to the sensitivity to detect ARs, i.e. the electric resistance provides the highest sensitivity [52]. Furthermore, the time-dependent voltage drop at a specific eigenmode during arc flicker was evaluated [42]. Time-dependent experimental investigations and simulations on the voltage and the electric current signal demonstrate the influence of ARs on these signals [76]. Investigations of the power threshold necessary to excite acoustic instabilities were conducted at a high-pressure sodium lamp [62]. ARs can also be detected by sound measurements outside the lamp because the noise generated by the flickering discharge arc leads to oscillations of the arc tube [63,64]. It is even possible to excite ARs inside the arc tube by laser absorption [77].

Simulations of the AR effect in discharge lamps calculate the acoustic eigenmodes and their corresponding frequencies by solving the homogeneous wave equation. When the lamp is operated in upright position, so that the temperature field is rotationally symmetric, a two-dimensional (2D) axisymmetric model is sufficient to simulate the physical processes. Differential equations describe the conservation of mass, momentum, energy and charge. Thereafter, the 2D temperature field can be mapped onto the full three-dimensional (3D) geometry to determine all AR frequencies, and these can be compared to the experimentally determined resonance frequencies [67,78,79]. In horizontally operated lamps, acoustic eigenmodes were simulated with a temperature field that was predetermined by experiments [80].

To compute the absolute acoustic pressure in an HID lamp, the inhomogeneous wave equation has to be solved. This can be achieved by an eigenmode expansion that incorporates loss factors. The method was applied to a stationary 2D axisymmetric cylindrical model that represents the arc tube of an HID lamp [81]. Inside the cylinder, the temperature distribution was approximated by a parabolic shape function in radial direction. The result is the acoustic response that shows the acoustic pressure as a function of the frequency at a specified position inside the

arc tube. A similar method was used to solve the acoustic response function inside a more complex geometry [71]. Here, the 2D axisymmetric simulation additionally incorporates the electrodes and the tube wall. Instead of a predefined temperature field, the simulation solves the coupled equations for the conservation of mass, momentum, energy and charge.

Simulations of the AS effect inside the arc tube of discharge lamps mainly pay attention to the velocity and the temperature field. A time-dependent simulation demonstrates the severe effects of AS on both fields when the input power of 175 W oscillates by 30 % at the second azimuthal mode at 31.8 kHz [57]. The position of the maximal temperature inside the horizontally operated arc tube with a diameter of 6 mm changes by 1.4 mm. Additionally, the simulation predicts a periodic time of the arc movement of 80 ms to 100 ms. This was confirmed by experiments that showed arc motion on a time scale of 50 ms to 100 ms. The pressure oscillations induce an AS field, that interacts with the buoyancy-driven velocity field, and change the position of the arc. In the model, the classical set of conservation equations (mass, momentum, energy, charge) is extended by terms that account for the pressure dilatation and the viscous damping. The geometrical simple 2D model of the pure-mercury HID lamp describes an infinitely long arc tube. The geometrical simplification enables a reduction of the numbers of finite element nodes to under 1200 and, accordingly, a limitation of the computing time. A more detailed analysis of the velocity and the pressure oscillations reveals different kinds of streaming that occur in the arc tube during acoustic excitation [82]. These kinds of streaming are discussed in Section 3.2.2.

A 2D axisymmetric model of a high-pressure sodium discharge lamp, that includes the AS force in the momentum conservation equation, solves the stationary AS velocity field. The driving force bases on the acoustic pressure of the 8^{th} longitudinal mode [83] or 4^{th} longitudinal mode [84], respectively.

The AS effect is beneficial with regard to the luminous efficacy of the HID lamp at specific operating conditions [7,27]. The bent arc in a horizontally operated lamp can be straightened by an acoustically induced flow field. This arc straightening effect compensates the deformed temperature field so that the thermomechanical stress in the upper part of the arc tube wall can be reduced. When the simulation model that showed the flicker phenomenon due to AS [57], is driven with a swept power frequency instead of a pure sinusoidal signal at the second azimuthal mode, a different circular convection flow emerges that lowers the arc from its original position [27]. The results were experimentally verified by measurements of the arc

curvature. The impact of arc straightening on the whole lamp and driver system shows significant efficiency improvements [7]. Arc straightening in a 250 W lamp enables electrical-to-visible conversion efficiencies larger than 50 % at luminous efficacies of $155\,\mathrm{lm\,W^{-1}}$. The temperature of the upper part of the wall can be reduced by 150 K. Experiments, in which the discharge arc is acoustically excited by a modulated DC voltage, show an arc centring at specific switching frequencies [85]. It is stated that standing radial acoustic waves suppress the convection flow and are responsible for the lower arc deflection. In a 3D simulation of an HID lamp, it was also investigated how external magnetic forces can straighten the discharge arc [86].

2.4 Research Questions

The research aim is to further develop HID lamps. The work should investigate light fluctuations inside the arc tube caused by acoustic excitation. A comprehensive understanding of the underlying mechanism will enable improvements on the lamp design, which will be characterised by a significantly higher energy efficiency compared to state-of-the-art lamps.

A numerical model on the basis of the finite element method has to be created to simulate the plasma behaviour in the arc tube of metal halide lamps. This model should enable systematic investigations of the mechanisms that lead to the origin of the plasma instabilities. Particularly, the AS effect has to be implemented in the numerical model. Its influence on the behaviour of the discharge arc should be analysed. The investigations should incorporate considerations of the velocity field of the fluid flow inside the arc tube as well as investigations of the impact on the temperature and the electric field.

For a thorough understanding of the instabilities, accompanying experimental investigations have to be conducted. These investigations should be able to electrically and optically quantify the discharge arc at stable and instable operating conditions. Especially, changes during acoustic excitation of the arc tube content should be detected. The results of the experiments and simulations have to be compared and discussed.

The work will treat the following research questions:

- Can the AS effect qualitatively and quantitatively explain the arc flicker phenomenon in the HID lamp?

- Which simulation data and/or experimental parameters enable quantification of the AS effect?
- Why does not every AR excite visible discharge arc motions?
- How do geometries and materials in the HID lamp influence the physical fields inside the arc tube and the AR frequencies that deteriorate the light quality?
- Which experimental data (optical, electrical and acoustical) can verify the numerical results, and are the results of the experiment and the simulation consistent?

Chapter 3

Theory

3.1 Thermal Plasma

The theory of the thermal plasma describes the physical processes in the HID lamp, which serve to calculate the acoustic eigenmodes and the corresponding eigenfrequencies. Initially, the plasma is characterised, and the difference between thermal and non-thermal plasmas is clarified. In particular, an explanation is given, why just one temperature is sufficient to describe the plasma of the investigated lamp. Afterwards, the coupled partial differential equations, that enable the calculation of the temperature profile inside the arc tube of the HID lamp, are presented.

Plasma is an ionised gas. It is often referred to as the fourth state of matter because it has a higher molecule energy than a solid, a liquid or a gas of the same composition. Due to the electric charge of the free electrons and ions, plasma properties are different to those of the other states of matter. In contrast to a gas, a plasma is electrically conductive, internally interactive and strongly responsive to electromagnetic fields [87].

The degree of ionisation, the electron density and the temperature characterise a plasma. The temperature of plasma particles is defined by their energy. When an HID lamp is ignited, the energy of the electric field is initially accumulated by the electrons. These are accelerated up to their mean free path. When colliding with a heavy particle, only a small amount of kinetic energy is transferred. Hence, the electrons initially possess a higher temperature than the heavy particles. For this reason, a temperature classification of a plasma always indicates the highest (electron) temperature.

If the plasma is just weakly ionised, the temperature difference is convention-

ally proportional to $(\vec{E}/p)^2$ (electric field $\vec{E}$, pressure p) [87]. In thermal plasmas, also called hot plasmas, the temperature difference between electrons and heavy particles diminishes because the Joule heating equilibrates both temperatures. The collisions occur periodically so that the ratio of the electric field to the pressure decreases to small values. If, additionally, chemical equilibrium is reached and the temperature gradients are small, this quasi-equilibrium state is called local thermal equilibrium (LTE). The plasma in this state can be identified by a single, space-dependent temperature.

At a low plasma pressure or a low power, the temperature difference between electrons and heavy particles is so high that the thermal plasma is not in its equilibrium state any more. In these non-thermal or cold plasmas, the electrons possess the main part of energy, and the thermal motion of the ions is negligibly small. In many of these non-equilibrium plasmas, the electron temperature is significantly higher (approximately 10 000 K) than the temperature of the heavy particles in the gas (room temperature). At even lower energy levels, ions and electrons recombine and the plasma becomes a gas.

In non-thermal plasmas, the details of the discharge kinetics have to be incorporated to adequately described the physical quantities, such as the density of charged particles or the electric conductivity, whereas thermal plasmas are characterised by their temperature and pressure only [88]. For thermal plasmas, the Saha-Langmuir equation relates the degree of ionisation to the temperature and pressure [89,90].

The high pressure and high electric current enables to treat plasmas in HID lamps as quasi-equilibrium plasmas [91]. The LTE approach is suitable to describe the plasma [92], and this approach is commonly used in simulations of plasmas in HID lamps [71,81,93–95]. Due to the constant pressure at stable operating conditions, only the spatial temperature distribution is necessary to characterise the material properties. Consequently, the material parameters, e.g. the electric and thermal conductivity, the specific heat capacity and the net emission coefficient, only depend on the temperature. These parameters can be calculated with the aid of the Chapman-Enskog theory [96]. The results are presented in Section 4.2. Finite element simulations that compute both, the electron and the heavy species temperature, show decreasing temperature differences between electrons and heavy particles at an increasing pressure as well as at higher electric currents [91,97]. In these reports, pure mercury plasmas with a pressure less than 0.2 MPa were investigated.

In contrast to low pressure plasmas, plasmas with a pressure higher or equal 4.0 MPa do not require a separate calculation of electron and heavy particle tem-

peratures. The existing deviations from LTE can be included for important material properties, like the electrical conductivity of the plasma, only [98–101]. The results show that the deviations are limited to very restricted plasma regions near the electrode tips.

To calculate the acoustic eigenmodes and eigenfrequencies in the arc tube of the HID lamp, equations are required that describe the spatial temperature distribution. Therefore, the plasma is defined by coupled partial differential equations for the conservation of charge, energy, momentum and mass. All corresponding boundary conditions, material parameters and transport coefficients are specified in Section 4.2 and Section 4.3.2.

Interactions between the electrode and the plasma are neglected because these effects are of minor importance for the scope of this work. Such investigations either divide the plasma near the electrodes into subdomains to separately consider the different physical effects in the plasma sheaths [102–106] or study the electric current transfer from electrode to plasma in greater detail [30,107]. Simulations, that focus on the power balance at the interface of plasma and electrodes, use enhanced heat transfer models [33,38,98,100]. These models include cooling and heating by the electron current, heating by ion current and radiation cooling during the anode and the cathode phase. These phases only occur during AC operation and are characterised by attraction of negatively charged particles in case of the anode phase and positively charged particles in case of the cathode phase.

The HID lamp is provided with electric power that is partially converted into light. Therefore, an electric current is supplied to the electrodes. The continuity equation in electromagnetism

$$\frac{\partial \rho_\mathrm{c}}{\partial t} + \vec{\nabla} \cdot \vec{j} = 0 \tag{3.1}$$

is a first-order differential equation that describes the conservation of charge density ρ_c. The electric current density

$$\vec{j} = \sigma \vec{E} = -\sigma \vec{\nabla} V \tag{3.2}$$

can be expressed as the product of the electric conductivity σ and the electric field $\vec{E}$ that is the gradient of the electric potential V. The electric current

$$I = -\int_{S_\mathrm{cc}} \vec{j} \cdot \mathrm{d}\vec{S} \tag{3.3}$$

can be calculated by integrating the current density over the current-carrying surface S_{cc} of the electrode. Naturally, the electric current I depends on the electric input power and the electric potential drop between the electrodes.

The second-order partial differential equation of heat conduction

$$\rho c_p \left(\frac{\partial T}{\partial t} + \left(\vec{u} \cdot \vec{\nabla} \right) T \right) = - \left(\vec{\nabla} \cdot \vec{q} \right) + \boldsymbol{\tau} : \mathbf{S} - \frac{T}{\rho} \frac{\partial \rho}{\partial T} \bigg|_p \left(\frac{\partial p}{\partial t} + \left(\vec{u} \cdot \vec{\nabla} \right) p \right) + Q \tag{3.4}$$

has to be solved to obtain the temperature distribution T of the arc tube content, the electrodes and the arc tube wall of the HID lamp (mass density ρ, specific heat capacity at constant pressure c_p, fluid velocity $\vec{u}$). The left-hand side of the equation includes terms that represent the temporal change of the temperature and the convective heat flux. The right-hand side of Equation 3.4 incorporates the conductive heat flux $\vec{q} = -\kappa \vec{\nabla} T$ with the thermal conductivity κ. The second and third term on the right-hand side represent the viscous dissipation (viscous stress tensor $\boldsymbol{\tau}$, strain rate tensor $\mathbf{S}$) and the pressure work, which are negligible in HID lamps because of the low Mach and Prandtl numbers. In case of the electric discharge, the source term Q is the difference between the Joule heat $\sigma |\vec{E}|^2$ and the emitted radiation power q_{rad}. Equation 3.4 then simplifies to

$$\rho c_p \frac{\partial T}{\partial t} + \vec{\nabla} \cdot \left(-\kappa \vec{\nabla} T \right) + \rho c_p \vec{u} \cdot \vec{\nabla} T = \sigma |\vec{E}|^2 - q_{\mathrm{rad}}, \tag{3.5}$$

which is known as the Elenbaas-Heller equation. As the plasma is assumed to be in LTE, only one temperature for both, electrons and heavy particles, has to be calculated.

The fluid velocity, which is required to obtain the convective heat flux, is derived from the momentum conservation equation, a nonlinear second-order partial differential equation. In case of a compressible Newtonian fluid, the Navier-Stokes equation

$$\rho \frac{\partial \vec{u}}{\partial t} + \rho \left(\vec{u} \cdot \vec{\nabla} \right) \vec{u} = \vec{\nabla} \cdot \left[-P\mathbf{I} + \eta \left(\vec{\nabla} \vec{u} + \left(\vec{\nabla} \vec{u} \right)^{\mathrm{T}} \right) - \frac{2}{3} \eta \left(\vec{\nabla} \cdot \vec{u} \right) \mathbf{I} \right] + \vec{f} \tag{3.6}$$

describes the fluid flow field. As in the heat conduction equation, the left-hand side is composed of a term that describes the temporal change of the flow, and a term that accounts for the convection. The terms on the right-hand side include the hydrostatic effect (static pressure P, identity matrix $\mathbf{I}$), the Cauchy stress tensor (dynamic viscosity η) and the general volume force $\vec{f}$ that in the simplest case is

the gravitational force

$$f_l = -\delta_{l3}\rho g \tag{3.7}$$

(δ_{l3} Kronecker symbol: Index 3 corresponds to the z-direction, $g = 9.81\,\mathrm{m\,s^{-2}}$). Furthermore, the continuity equation for the mass density

$$\frac{\partial \rho}{\partial t} + \vec{\nabla} \cdot (\rho \vec{u}) = 0, \tag{3.8}$$

a first-order differential equation, and the ideal gas law

$$\rho = \frac{PM}{RT} \tag{3.9}$$

(molar mass M, molar gas constant R) are required to solve the set of equations.

In addition to the conservation laws, Planck's law is briefly described. The knowledge of Planck's law is necessary to compare the light intensity measurements of the stable discharge arc with simulation results of the temperature distribution. For a black-body radiator, Planck's law links the spectral radiance to the wavelength and the temperature. The black body is an idealised thermal radiation source. Consequently, the electromagnetic spectrum is defined by the temperature only. Compared to the black-body radiation, the emitted light from the HID lamp exhibits differences; an HID lamp is a selective radiator. The mercury and the metal halides show radiation peaks at specific wavelengths, whereas the black body shows a continuous spectral emission. The various states of metal halide ions (compare Figure 4.2) involve a huge number of selective radiation peaks in the visible wavelength range.The high-pressure inside the arc tube leads to a line broadening of the selective spectra so that the spectrum of the HID lamp approaches the continuous spectral intensity of the black-body radiator [38]. This allows to convert the temperature values of the simulation into a spectral radiance.

Planck's law describes the specific spectral emission [108]

$$R_{\mathrm{spec}}(\lambda, T) = \frac{2\pi h c_0^2}{\lambda^5} \left(\exp\left(\frac{h c_0}{\lambda k T} \right) - 1 \right)^{-1}, \tag{3.10}$$

which depends on the wavelength λ and the temperature T (speed of light c_0, Planck's constant h, Boltzmann constant k). To obtain the total emission in a wavelength range from λ_1 to λ_2, the function has to be integrated so that

$$R_{\mathrm{spec}}(\lambda_{1,2}, T) = \frac{2\pi k^4 T^4}{h^3 c_0^2} \int_{x_1}^{x_2} \frac{x^3}{\exp(x)} \mathrm{d}x \tag{3.11}$$

results [4]. Here, the substitutions

$$x_1 = \frac{hc_0}{\lambda_1 kT}, \qquad x_2 = \frac{hc_0}{\lambda_2 kT} \tag{3.12}$$

have been introduced. The bounds of integration are defined by the sensitivity of the camera that is used to record the images of the discharge arc. The camera specifications are presented in Section 4.4.

3.2 Acoustical Phenomena

3.2.1 Acoustic Resonance

The coupled equations described in the previous section serve to determine the temperature distribution T and the power density of heat generation $\mathscr{H}$ that equals the source term of the Elenbaas-Heller equation Q. These space-dependent quantities are necessary to calculate the acoustic eigenmodes, the corresponding eigenfrequencies and in particular the acoustic pressure amplitude.

A lamp operation with a periodic input power, that is caused by an alternating electric current, induces energy exchanges by elastic collisions between the charged particles and the neutral gas [61]. This leads to pressure oscillations of the gas filling with the same frequency as the electric input power. In case of pure AC operation, the frequency of power oscillations is twice the driving AC frequency. The pressure waves arise at the discharge arc, propagate through the vessel in the form of longitudinal waves, are reflected at the rigid wall and travel back in a different direction. When the excitation frequency is tuned to an acoustic eigenfrequency, incident and reflected waves interfere and standing acoustic pressure waves are established. This eigenmode contains pressure nodes, where the pressure equals the constant equilibrium pressure, and pressure antinodes, where the pressure oscillates at that eigenfrequency around the equilibrium pressure with its maximal amplitude. Velocity antinodes are located at pressure nodes and vice versa [61]. The mathematical relationship between both quantities is described by Equation 3.34.

The wave equation, a second-order partial differential equation, describes the propagation of waves through a medium. In case of the HID lamp, the heat density acts as a source term H for the generation of pressure waves p. Therefore, the

time-dependent equation can be described by [109]

$$\vec{\nabla}\cdot\left(\frac{1}{\rho}\vec{\nabla}p\right)-\frac{1}{c^2}\frac{\partial^2 p}{\partial t^2}=-\frac{\gamma-1}{c^2}\frac{\partial H}{\partial t} \tag{3.13}$$

with the speed of sound c and the heat capacity ratio γ. The time-dependent wave equation can be converted into the frequency domain by a Fourier transform (harmonic time dependency: $\exp(-\mathrm{i}\omega t)$). A Helmholtz equation

$$\vec{\nabla}\cdot\left(\frac{1}{\rho}\vec{\nabla}p\right)+\frac{\omega^2}{\rho c^2}p=\mathrm{i}\omega\frac{\gamma-1}{\rho c^2}\mathscr{H} \tag{3.14}$$

results. As the temperature inside the arc tube is not constant, the mass density ρ and the speed of sound

$$c=\sqrt{\gamma\frac{RT}{M}} \tag{3.15}$$

are space-dependent quantities as well*. This equation assumes that the gas behaves like an ideal gas. R is the molar gas constant, and M is the molar mass of the gas composite. The source term

$$\mathscr{H}=\sigma|\vec{E}|^2-q_{\mathrm{rad}} \tag{3.16}$$

equals the power density of heat generation, which is identical to the right-hand side of the Elenbaas-Heller equation (Equation 3.5).

The solution of the inhomogeneous Helmholtz equation can be expressed by a superposition of the pressure modes $p_j(\vec{r})$ with the amplitudes $A_j(\omega)$ of the j^{th}-mode [110–112]:

$$p(\vec{r},\omega)=\sum_j A_j(\omega)\,p_j(\vec{r}), \tag{3.17}$$

which separates the pressure into a space-dependent and a frequency-dependent part that can be calculated separately. The pressure modes and the eigen angular frequencies ω_j can be calculated from the homogeneous Helmholtz equation

$$\vec{\nabla}\cdot\left(\frac{1}{\rho}\vec{\nabla}p\right)+\frac{\omega^2}{\rho c^2}p=0 \tag{3.18}$$

with appropriate boundary conditions. Additionally, these modes have to be nor-

*Actually $c\rho^2$ is constant.

malised according to the condition

$$\int_{V_c} p_i^* p_j \mathrm{d}V = V_c \delta_{ij} \tag{3.19}$$

with the enclosed volume V_c. p_i^* is the complex conjugate of the acoustic pressure of the i^{th}-mode p_i. The frequency-dependent amplitudes are described by a Lorentzian function

$$A_j(\omega) = \mathrm{i}\frac{\mathscr{A}_j \omega}{\omega^2 - \omega_j^2} \tag{3.20}$$

that has singularities when the frequency approaches the eigenfrequency because of the non-consideration of acoustic losses. $\mathscr{A}_j$ is determined from an overlap integral of the acoustic mode and the source term:

$$\mathscr{A}_j = \frac{\gamma - 1}{V_c} \int_{V_c} p_j^* \mathscr{H} \mathrm{d}V. \tag{3.21}$$

If acoustic loss effects would be included in Equation 3.13 or Equation 3.14, complex solutions would result [110]. Therefore, sound absorption is included by a perturbation of the loss-free solution. Hence, the description of the amplitude is extended by a loss factor L_j [110,113]:

$$A_j(\omega) = \mathrm{i}\frac{\mathscr{A}_j \omega}{\omega^2 - \omega_j^2 + \mathrm{i}\omega\omega_j L_j}. \tag{3.22}$$

The total loss factor L_j comprises different kinds of losses. In this work, the effects caused by heat conduction and shear stress are taken into account. Both absorption mechanisms increase with the square of the driving frequency [65]. Further mechanisms, like cell or gas imperfections, are not considered because these are of minor importance [110]. The derivation of these loss factors can be found elsewhere [109]. The shear stress and heat conduction losses can further be separated into volume and surface losses [109].

The gas temperature in direct vicinity of the tube wall always possess the same temperature than that of the wall because the thermal conductivity of the wall is by a factor of approximately 10^3 higher in this region (compare Section 4.2). The gas behaves isothermally. In contrast to that, a pressure wave will adiabatically expand and contract the gas far off the wall. Figure 3.1 schematically shows the mechanism of heat exchange. In the transition zone between these two states, acoustic loss due to heat conduction arises. The thickness of this layer depends on the considered

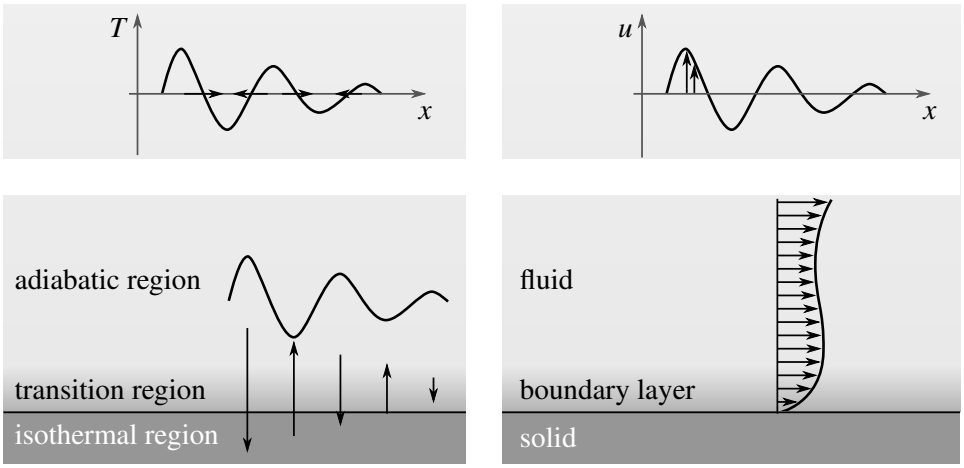

Figure 3.1. Visualisation of the four incorporated acoustic loss effects: Acoustic losses in the volume (top) and at the surface (bottom) as well as losses due to heat conduction (left) and due to shear stress (right) [111].

mechanism. Thermal losses occur in a layer of thickness

$$\delta_\kappa = \sqrt{\frac{2\kappa}{c_p \rho \omega_j}}, \tag{3.23}$$

whereas the thickness of the Prandtl boundary layer related to the surface loss due to shear stress is

$$\delta_\eta = \sqrt{\frac{2\eta}{\rho \omega_j}}. \tag{3.24}$$

The thermal surface loss at the interior walls of the vessel can then be calculated with a surface integral over the acoustic pressure of the j^{th}-mode

$$L_j^{S_\kappa} = \frac{(\gamma - 1)\,\delta_\kappa}{2V_c} \int_{S_c} |p_j|^2 \, \mathrm{d}S \tag{3.25}$$

on condition that the ratio of thermal conductivities $\kappa_{\text{wall}}/\kappa_{\text{gas}}$ is large. This is the case in the investigated HID lamp, whose conductivity of the wall is by a factor of more than 10^3 higher (compare Section 4.2).

The surface loss resulting from shear stress is derived from a similar surface integral

$$L_j^{S_\eta} = \frac{c^2 \delta_\eta}{2\omega_j^2 V_c} \int_{S_c} \left| \vec{\nabla}_t p_j \right|^2 \mathrm{d}S. \tag{3.26}$$

Here, $\vec{\nabla}_t p_j$ denotes the tangential component of the gradient of the acoustic pres-

sure mode p_j. In Prandtl's boundary layer, the fluid velocity drops from a certain value caused by the acoustic wave to zero at the wall. The velocity difference of neighbouring layers results in viscous friction.

Outside the boundary layer, Stokes-Kirchhoff loss reduces the amplitude of the acoustic pressure. The fluid viscosity leads to shear stress (Figure 3.1, top right). Hence, losses in the tube volume occur that can be described by [109,110]

$$L_j^{\mathrm{V}_\eta} = \frac{4}{3\rho c^2} \sum_i \omega_i \left(\frac{A_i}{A_j} \right)^* \frac{1}{V_\mathrm{c}} \int_{V_\mathrm{c}} \eta p_i^* p_j \mathrm{d}V. \tag{3.27}$$

For a constant viscosity, the sum in the equation would reduce to a single term because the eigenmodes p_j are orthogonal functions. Therefore, the viscosity

$$\eta = \bar{\eta} + \hat{\eta} \tag{3.28}$$

is split into a mean value $\bar{\eta}$ and a space-dependent part $\hat{\eta}$ that leads to a volume loss due to shear stress of

$$L_j^{\mathrm{V}_\eta} = \frac{4\bar{\eta}}{3\rho c^2} \omega_j + \hat{l}_\eta, \tag{3.29}$$

in which $\hat{l}_\eta$ describes a correction term for the space-dependent part.

The pressure waves in the tube are accompanied by temperature waves. The thermal conductivity of the gas generates a heat exchange between regions of different temperature. Figure 3.1 (top left) schematically depicts that the energy of the sound wave dissipates. Similar to the volumetric shear stress losses, the thermal conductivity

$$\kappa = \bar{\kappa} + \hat{\kappa} \tag{3.30}$$

is split into the mean value $\bar{\kappa}$ and the space-dependent part $\hat{\kappa}$. Consequently, the volume loss due to heat conduction is

$$L_j^{\mathrm{V}_\kappa} = \frac{(\gamma - 1)\,\bar{\kappa}}{c_p \rho c^2} \omega_j + \hat{l}_\kappa. \tag{3.31}$$

The solution of the volume loss factors without the correction terms $\hat{l}_\eta$ and $\hat{l}_\kappa$ shows that the losses linearly dependent on the frequency. The critical damping takes place at $L_j = 2$ and at a frequency of $f_\mathrm{crit} \approx 1\,\mathrm{GHz}$ [71]. A significant shift of f_crit by the correction terms is highly improbable. For the investigated frequency range (maximal 50 kHz), these terms in the Equations 3.29 and 3.31 can be neglected.

3.2.2 Acoustic Streaming

The acoustic streaming phenomenon in HID lamps can lead to undesired effects, but AS can also be constructively exploited for different acoustofluidic devices. Particularly in the chemical industry, pharmaceuticals, biotechnology and medicine, the effect is beneficial because it is possible to rapidly mix two solutions, agglomerate particles of a solution, clean surfaces, create droplets and pump liquids on a small (µm to mm) scale [114].

The excitation of ARs in HID lamps can lead to discharge instabilities, but the resonances themselves are not the reasons of these instabilities. Since the first reports on discharge instabilities in compact xenon arc lamps in 1963 [68,69], the connection between the occurrence of high frequency standing pressure waves and low frequency light intensity fluctuations mainly remained unexplored. The explanations were limited to universal statements, e.g. that the gas density oscillations distort the heat input and, hence, the discharge path [70]. It was even stated that so far no fundamental idea arose to link the ARs and the visible arc instabilities [63]. In fact, it was not until 2008 that a new hypothesis arose [57,61]. According to this, the fluid flow, which leads to the undesirable light flicker, could be explained with the aid of the AS effect.

It is well known that a fluid flow can generate sound when coming in contact with a solid. AS describes the opposite effect: Acoustic waves induce a non-zero mean mass flow. When a sound wave propagates through a volume, the fluid elements experience pressure and velocity oscillations. The time-average motion of a frictionless fluid would be zero, whereas in real fluids viscous losses generate net displacements of the particles so that a mean motion develops. The flow is the result of a second-order nonlinear effect that is generated by the attenuation of an acoustic wave. In the literature, different types of AS are characterised [115–117]: Boundary layer-driven streaming, Eckart streaming, Jet-driven streaming and travelling wave streaming.

- Boundary layer streaming
  In 1884, the first mathematical description of AS was derived by Rayleigh [118]. The investigations relate to experiments of Faraday [119] and Dvořák [120]. Rayleigh describes the air motion caused by a sound field between two parallel plates. The acoustic energy dissipates in the boundary layer of the plates due to the viscosity of the fluid. The results are counter-rotating streaming vortices outside the boundary layer of the fluid, whose size is of

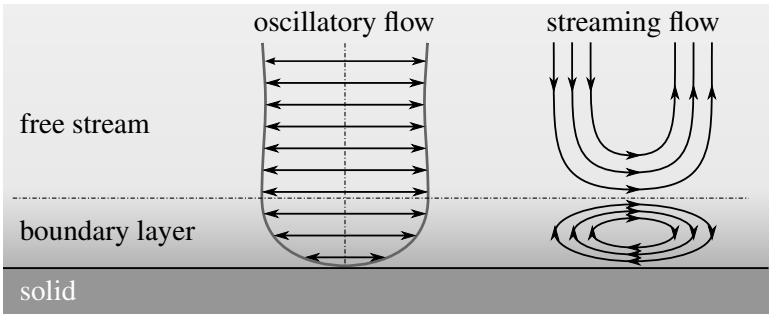

Figure 3.2. Boundary layer streaming.

the order of the wavelength of the standing pressure wave [121]. Nowadays, this type of streaming is called *Rayleigh streaming* or *outer boundary layer streaming*. A part of one of these vortices can be seen in Figure 3.2. The reason for the mass flow is the bulk viscosity of the filling gas that dampens the compressible fluid motion and, simultaneously, induces AS. The second order nonlinear effect arises from the convective terms of the governing momentum equations. In 1953, the mathematical description was extended by Nyborg [122] and corrected by Westervelt [123], who incorporated the Stokes drift that relates the Eulerian and the Lagrangian streaming velocity.

Next to the outer boundary layer streaming in the bulk of the fluid, an inner boundary layer streaming near the wall exists that is not included in the publication of Rayleigh. Schlichting mathematically described the vortex motion generated by an oscillating flow in the viscous boundary layer near a flat plate [124]. Therefore, this streaming is referred to as *Schlichting streaming*. Compared to the outer boundary layer streaming, the size of the inner boundary layer streaming vortices are much smaller than the wavelength of the stimulating flow [121]. In relation to the outside of the boundary layer, the dissipation inside the layer is large. A steep velocity gradient is established by the small thickness of the layer and the high velocity drop from its value in the bulk of the fluid to zero at the wall (no-slip condition of the boundary). In case of a standing wave, an oscillatory flow parallel to the surface is formed that causes a momentum flux, which is oriented from the pressure antinodes to the pressure nodes on the boundary. This generates a vortex in the boundary layer [114].

The oscillating flow as well as the resulting boundary layer streaming flow are depicted in Figure 3.2. The vortices inside the boundary layer rotate

in the opposite direction to those in the bulk of the fluid. The boundary layer thickness, that is also called viscous penetration depth, has already been described in Equation 3.24.

When a standing wave is excited in the arc tube of an HID lamp, boundary layer streaming occurs [61].

- Eckart streaming
  The second AS type is caused by the dissipation of acoustic energy outside the boundary layer or by the sound absorption due to the fluid viscosity. The amplitude of the acoustic wave decreases when travelling away from its source so that a steady momentum flux is generated that forms a fluid jet in the direction of propagation. Consequently, its size is much larger than the acoustic wavelength [121]. This AS is known as *Eckart streaming* [125] or *Quartz wind* because a quartz crystal is often used as the vibrating source.

- Jet-driven streaming
  Jet-driven streaming can be observed when a viscous fluid is periodically ejected out and sucked into an orifice. The fluid behaves differently during the inflow and outflow. The inflow pattern shows a flow that effectively sucks from all directions, whereas the outflow pattern shows a jet flow (see Figure 4 in [117]). Therefore, a mean toroidal flow is establish at an oscillatory flow.

- Travelling wave streaming
  The mechanism of travelling wave streaming is not characterised by an energy dissipation and, therefore, is different to the streaming types described so far. The non-zero net mass transport of travelling wave streaming is induced by a phase shift between the acoustic velocity and the density [117]. This AS is referred to as Gedeon streaming because of a theoretical treatise of this kind of AS in Stirling-type and pulse-tube thermoacoustic refrigerators from Gedeon in 1997 [126].

The AS force can either be derived mathematically with the method of successive approximations [118,122,127–130], in which the velocity, density and pressure in the momentum and continuity equation are considered up to the second order terms, or with the vorticity transport equation [115] in which the curl of the governing equations is considered. In case of the method of successive approximations, the first order field results in the wave equation for Newtonian fluids, and the time-independent velocity of the second order field is the quantity of interest.

The resulting force density to describe the motion

$$f_l = \frac{\partial \overline{\rho v_k v_l}}{\partial x_k} \tag{3.32}$$

is the divergence of the Reynolds stress tensor, which was initially derived by Lighthill [131]. The overline in this equation indicates time averaging over one period. Here, Einstein's sum convention has to be applied. The Reynolds stresses depend on the amplitude of the sound particle velocity $\vec{v}$, and the body force reflects diminutions of the acoustic wave. In case of the HID lamp, the source of the momentum conservation equation (Equation 3.6) is the sum of the gravitational and the AS force. The time averaging for harmonic waves simplifies Equation 3.32 to

$$f_l = \frac{1}{2} \frac{\partial \rho \hat{v}_k \hat{v}_l}{\partial x_k} \tag{3.33}$$

with the amplitude of the sound particle velocity $\vec{\hat{v}}$, which can be calculated from the acoustic pressure [132]:

$$\vec{v}(\vec{r}, \omega) = \frac{1}{\mathrm{i}\omega\rho} \vec{\nabla} p(\vec{r}, \omega). \tag{3.34}$$

The driving force of AS is the decreasing acoustic particle velocity in the viscous boundary layer near the wall. However, the calculation of the eigenmodes from the wave equation (Equation 3.14) does not account for the no-slip boundary condition. Therefore, the acoustic particle velocity has to be corrected with an appropriate factor $s(d)$ that is equal to zero at the wall and one in the bulk of the fluid so that the velocity is described by [133]

$$\hat{v}_k(\vec{r}, \omega) \rightarrow \hat{v}_k^*(\vec{r}, \omega) := \hat{v}_k(\vec{r}, \omega) s(d). \tag{3.35}$$

d is the perpendicular distance of the point $\vec{r}$ to the wall.

The exponential decay of the velocity is defined by [133]

$$s(d) = 1 - \exp\left(-(1+\mathrm{i}) \frac{d}{\delta} \right). \tag{3.36}$$

This function contains an oscillating and a damping factor. It is drawn in Figure 3.3 for different driving frequencies that influence the thickness of the boundary layer δ (Equation 3.24). Eventually, the sound particle velocity $\hat{v}_k$ is replaced by the modified velocity $\hat{v}_k^*$ in the force term f_l of the momentum conservation equation.

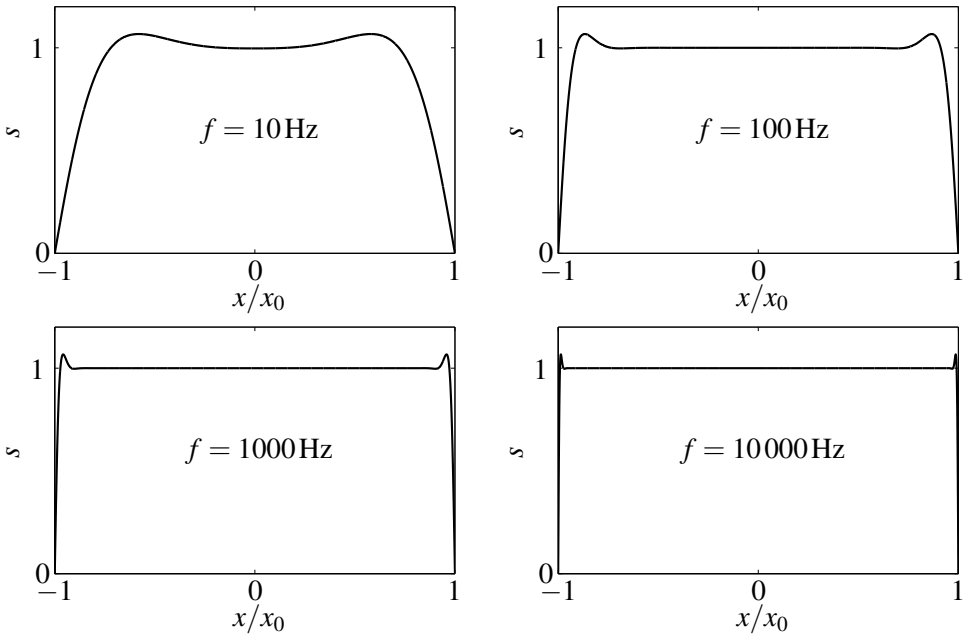

Figure 3.3. Profile of the acoustic particle velocity in a 1 mm wide channel at different driving frequencies. The dynamic viscosity is assumed to be $\eta = 10^{-6}\,\mathrm{Pa\,s}$ and the mass density $\rho = 1\,\mathrm{kg\,m^{-3}}$.

3.3 Bifurcations, Instabilities, Duffing Oscillator

A bifurcation describes a qualitative change of a nonlinear system. The behaviour of the system can change when a specific parameter, the *control parameter*, is varied. Especially, the stability of the solution can depend on the control parameter. The value of the parameter, at which the transition to an instability occurs, is called *critical point*.

In the following, exemplary bifurcations and instabilities are introduced that are derived on the basis of an incompressible viscous fluid. The dimensionless Navier-Stokes and continuity equation [134]

$$\vec{u}\cdot\vec{\nabla}\vec{u} = -\vec{\nabla}P + Re^{-1}\vec{\Delta}\vec{u} \tag{3.37a}$$

$$\vec{\nabla}\cdot\vec{u} = 0 \tag{3.37b}$$

describe the fluid velocity $\vec{u}$ and the pressure P. These generally depend on the Reynolds number ($Re = u l_{\mathrm{char}} \rho \eta^{-1}$) with the characteristic length l_{char}, the typical velocity u, the dynamic viscosity η and the mass density ρ. The Reynolds number serves as the control parameter for the fluid flow. If Re is varied, instability can

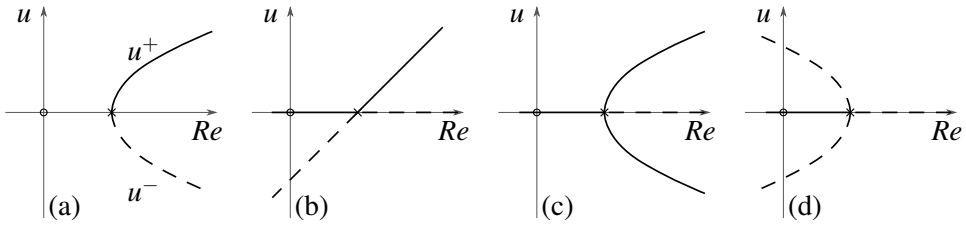

Figure 3.4. Different bifurcation types: Saddle-node (a) and transcritical (b) bifurcation as well as supercritical pitchfork (c) and subcritical pitchfork (d) bifurcation. The dashed line represents unstable solutions and the solid line stable solutions. The circle marks the point of origin and the cross the critical Reynolds number Re_{crit}.

set in and, hence, more than one solution can exist [135]. As the Reynolds number increases, the flow changes from a laminar to a turbulent flow. The transition does not occur abruptly, but is rather defined by many intermediate states. These states can qualitatively be described by simple algebraic or ordinary-differential equations, which represent local properties of bifurcations of the Navier-Stokes equations [136].

The simplest model to show bifurcations is the saddle-node bifurcation that is described by [134,137]

$$\frac{\mathrm{d}u}{\mathrm{d}t} = \dot{u} = (Re - Re_{\text{crit}}) - u^2. \tag{3.38}$$

The time-independent solutions of this equation show two solutions at $Re > Re_{\text{crit}}$, one solution at $Re = Re_{\text{crit}}$ and no solution at $Re < Re_{\text{crit}}$. At the bifurcation point Re_{crit}, two solutions u^+ and u^- appear. To test the stability of the solutions, its behaviour under the influence of small perturbations is investigated. The sign of $\dot{u}$ indicates whether the solution is stable ($\dot{u} > 0$) or unstable ($\dot{u} < 0$). Its result is highlighted in Figure 3.4 (a). The solution u^+ (solid line) is stable because small perturbations will decay as $t \to \infty$. In case of u^- (dashed line), the solution is unstable because small perturbations will grow as $t \to \infty$ or approach the solution u^+ when the solution is perturbed in opposite direction. Additionally, the cross in the diagram shows the critical Reynolds number and the circle marks the point of origin.

In the same way, a transcritical bifurcation [134,137]

$$\frac{\mathrm{d}u}{\mathrm{d}t} = \dot{u} = (Re - Re_{\text{crit}})\, u - u^2 \tag{3.39}$$

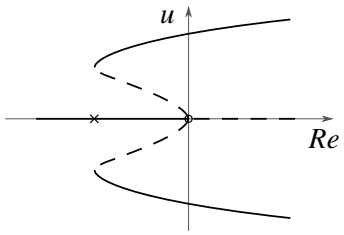

Figure 3.5. Bifurcation diagram of a subcritical pitchfork bifurcation including higher-order terms. The dashed line represents unstable solutions and the solid line stable solutions. The circle marks the point of origin and the cross the critical Reynolds number Re_{crit}.

can be investigated. Here, a change in the stability occurs when the control parameter is varied. In contrast to the saddle-node bifurcation, solutions for every parameter value exist. At the bifurcation point merely the stability changes from the solution $u = 0$ to $u = Re$. Figure 3.4 (b) shows the bifurcation diagram of the transcritical bifurcation.

The diagrams on the right-hand side of Figure 3.4 ((c), (d)) display both types of pitchfork bifurcations. These bifurcation types are common in problems with a symmetrical flow in a spatial symmetric geometry [136]. With a changing control parameter Re, symmetry breaking and, hence, pairs of asymmetric solutions occur. In case of the supercritical pitchfork bifurcation, the negative sign for the cubic term in [134,137]

$$\frac{\mathrm{d}u}{\mathrm{d}t} = \dot{u} = (Re - Re_{\text{crit}})\, u \pm u^3 \tag{3.40}$$

has to be taken, which acts as a restoring force and stabilises the solution. Only one instable path occurs for $Re > Re_{\text{crit}}$. For the subcritical pitchfork bifurcation, the positive sign of the cubic term destabilises the solution. The inverted pitchfork only possesses stable solutions at $Re < Re_{\text{crit}}$.

To model real physical systems, even higher-order terms had to be considered. For example, a fifth-order term in the subcritical pitchfork bifurcation [137]

$$\frac{\mathrm{d}u}{\mathrm{d}t} = \dot{u} = (Re - Re_{\text{crit}})\, u + u^3 - u^5 \tag{3.41}$$

stabilises the unstable branches so that stable solutions exist at large values of $|u|$ (see Figure 3.5). Five solutions exists in total at $Re_{\text{crit}} < Re < 0$; two instable and three stable. Two of the stable solutions are antisymmetric ($u_1 = -u_2$) and one is symmetric ($u_3 = 0$). The time-independent solution depends on the initial condi-

tion u_0. Additionally, the symmetric solution is only stable to small perturbations. Large perturbations lead to a jump of the solution to a qualitatively changed velocity u. The origin is said to be locally stable, but not globally stable. Moreover, the existence of multiple solutions show a hysteresis: When increasing Re from $-\infty$ to $+\infty$, the solution will jump at $Re = 0$ to one of the two large-amplitude branches. At decreasing Re, the solution does not jump at $Re = 0$, but only at Re_{crit}.

Bifurcations and symmetry breaking can also be observed in experiments. The entropy in these nonlinear dynamical systems decreases locally because it is transferred to the environment [138]. A famous example of symmetry breaking can be observed when an incompressible, viscous fluid is moved between two rotating cylinders. A laminar Couette flow forms at low rotating velocities of the inner cylinder (Figure 3.6, left). The azimuthal velocity of this laminar flow monotonically decreases from the inner to the outer cylinder.

Once the rotation speed of the inner cylinder is increased above a certain value, the flow significantly changes. The azimuthal flow is superimposed by toroidal vortices that rotate pairwise in opposite direction (Figure 3.6, right). These vortices are also named *Taylor vortices*, and the flow is known as the *Taylor-Couette* flow. At the transition from the laminar flow to the flow that contains Taylor vortices, the relationship between two opposing forces changes. In case of the Taylor-Couette flow, the centrifugal force exceeds the viscous force. The centrifugal force increases with the square of the velocity, whereas the viscous force only increases linearly with the velocity.

Moreover, the symmetry changes at the transition. Both, the laminar Couette flow and the flow with the Taylor vortices, are stationary flows and are rotationally invariant, i.e. the flow does not change over the angle of the cylinder ϕ. However, only the Couette flow is translational invariant over the cylinder height z, which means that the flow does not alter when it is viewed from different cylinder heights. Contrarily, the translational invariance of the Taylor vortices is limited. The same flow can be observed only at discrete heights of the cylinder that differ by the length L [135]. In other words, the Couette flow does not posses a velocity in cylinder direction whereas the flow with the Taylor vortices does.

The Rayleigh-Bénard convection is a further example that shows symmetry breaking. Here, a temperature gradient between the bottom and the free surface of a flat, horizontal fluid is applied. Above a certain temperature difference, convection cells are generated because the particle diffusion is not able to transport enough

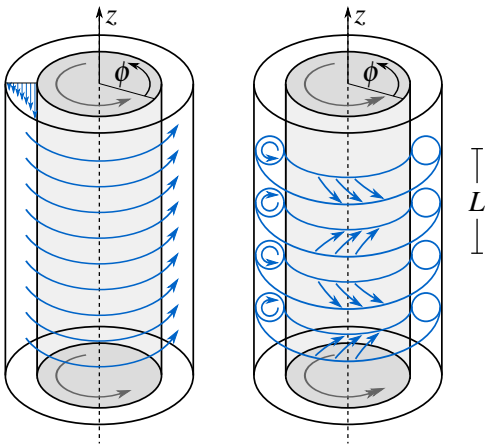

Figure 3.6. Taylor Couette flow: Laminar Couette flow appearing at low rotating velocities (left). Taylor vortices emerging at high rotating velocities (right).

heat from the ground to the surface any more so that an additional transport phenomenon is required. Both examples show that the fluid elements are affected by opposing forces and that the symmetrical state passes over into an unsymmetrical state.

A phase transition was also detected in the arc tube of HID lamps. These show bifurcation points that occur at the electric current transfer from the plasma to the cathode and describe the transition from the diffuse to the spot mode [139–141].

In the following, the Duffing oscillator, a nonlinear, damped, harmonically forced oscillator, is introduced. It was named after Georg Duffing, who was the first one that investigated such an oscillator in 1918 [142]. This classical paradigm enables illustration of the nonlinear behaviour, i.e. the jump phenomenon, the hysteresis effect and others.

The forced oscillator with a nonlinear spring

$$m\ddot{x} + k_0\dot{x} + k_1 x + k_3 x^3 = F\cos\omega t \tag{3.42}$$

contains the mass m, the displacement x, the damping coefficient k_0, the linear spring constant k_1, the cubic stiffness parameter k_3, the excitation force amplitude F and the excitation frequency $f_{\mathrm{ex}} = \omega/(2\pi)$. In case of $k_3 = 0$, the equation reduces to the forced linear oscillator with an eigenfrequency equal to $\omega_0 = \sqrt{k_1/m}$. At $k_3 > 0$, the system behaves as if a mechanical spring hardens when it is elongated. $k_3 < 0$ corresponds to a softening spring. These considerations are only

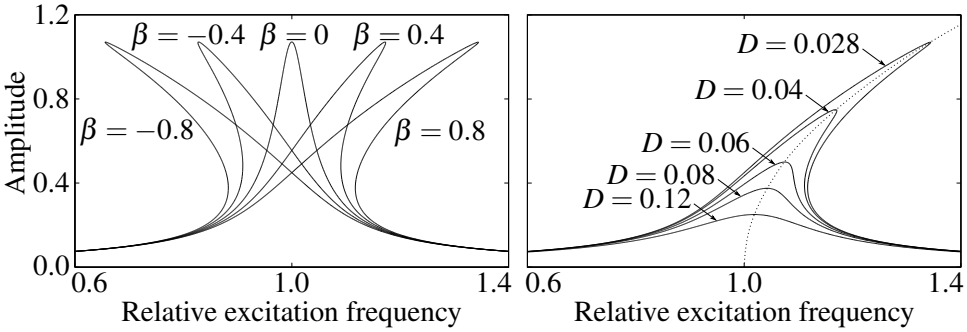

Figure 3.7. Resonance curves of the Duffing oscillator for $x_0 = 0.06$. On the left-hand side, the cubic stiffness parameter β is varied at $D = 0.028$. The diagram on the right-hand side shows resonances curves for different damping ratios D at $\beta = 0.8$. The backbone curve is marked as a dotted line.

valid for small deflections. The Duffing equation is often written in the non-dimensional form [143]

$$\ddot{x} + 2D\dot{x} + x + \beta x^3 = x_0 \cos \Omega\tau \tag{3.43}$$

with the normalised damping coefficient $D := k_0/\left(2\sqrt{k_1 m}\right)$, the relative excitation frequency $\Omega := \omega/\omega_0$, the static amplitude $x_0 := F/k_1$ and the time-scale $\tau := \omega_0 t$.

The solution of Equation 3.43 close to the eigenfrequency can be obtained by a perturbation analysis and with the assumptions of weak damping, weak nonlinearity as well as weak forcing. Consequently, the solution can be approximated by [144]

$$x_0^2 = 4\hat{x}^2 \left[D^2 + \left(\Omega - 1 - \frac{3}{8}\beta\hat{x}^2 \right)^2 \right] \tag{3.44}$$

with the amplitude of the oscillation $\hat{x}$. The resonance frequency is

$$\Omega_\mathrm{P} = 1 + \frac{3}{8}\beta a_\mathrm{P}^2 \tag{3.45}$$

and the peak amplitude is

$$a_\mathrm{P} = \frac{x_0}{2D}. \tag{3.46}$$

Equation 3.45 reveals that the stiffness parameter β changes the resonance frequency. It does not occur near the system's eigenfrequency as in the case of the linear resonator. Instead, the resonance of the Duffing oscillator is excited at a frequency far off the system's eigenfrequency.

Figure 3.7 (left) highlights the profound differences between the Duffing and

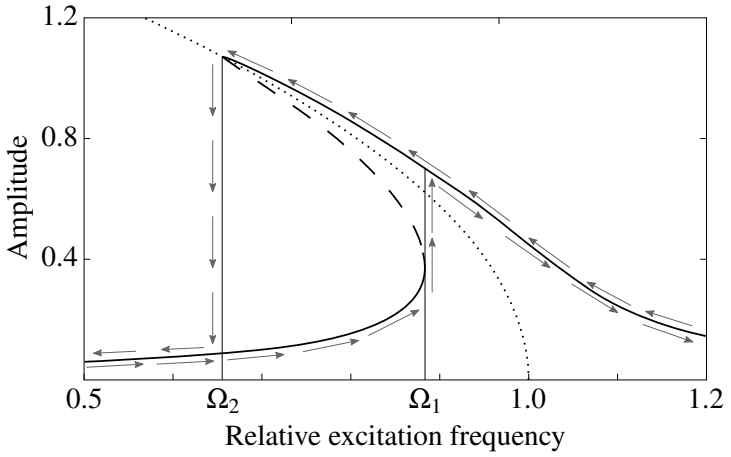

Figure 3.8. Amplitude response curve of the Duffing oscillator for $x_0 = 0.06$, $D = 0.028$ and $\beta = -0.8$. The arrows illustrate the jump phenomenon and the hysteresis. The solid and dashed line correspond to stable and unstable solutions, respectively. The dotted line marks the backbone curve.

the linear oscillator. $\beta = 0$ corresponds to the linear oscillator. It has a resonance frequency at $\Omega = 1$ and one solution for each excitation frequency. The Duffing oscillator ($\beta \neq 0$) has a resonance frequency at $\Omega \neq 1$ and can have multiple solutions. For a fixed excitation frequency, up to three real solutions for $\hat{x}$ exist depending on the parameter values of the Duffing equation (D,β). The nonlinearity causes a deflection of the peak values of the resonance curves either to lower excitation frequencies, when $\beta < 0$ (spring softening), or to higher excitation frequencies, when $\beta > 0$ (spring hardening). The magnitude of the deflection increases with the size of $|\beta|$. The different damping ratios in Figure 3.7 (right) emphasise their effect on the amplitude response curve. Additionally, the backbone curve is included that marks the maxima of the resonance curve. It can be derived from Equation 3.45:

$$a_{\mathrm{P}}(\Omega_{\mathrm{P}}) = \sqrt{\frac{8(\Omega_{\mathrm{P}} - 1)}{3\beta}}. \tag{3.47}$$

A typical behaviour of a nonlinear system is that the solution jumps between qualitatively different states. The arrows in Figure 3.8 illustrate the jump phenomenon and the hysteresis. For $\Omega > \Omega_1$ and $\Omega < \Omega_2$, only one solution exists. At $\Omega = \Omega_1$ and $\Omega = \Omega_2$, the solution loses stability and divides into two solution branches so that three solutions coexist for $\Omega_2 < \Omega < \Omega_1$; two stable and one unstable solution. A quasi-stationary change of the excitation frequency in the over-

hanging part of the amplitude response curve evokes the jump phenomenon. When decreasing the frequency from above Ω_1, the amplitude of the oscillation will follow the upper branch of the response curve. After passing the maximum at Ω_2, the amplitude will jump down to the lower branch and will follow this branch when the excitation frequency is further decreased. Analogously, at a slowly increasing frequency from below Ω_2 the solution will follow the lower branch and will jump to the higher amplitude branch at Ω_1. The dashed line in Figure 3.8 corresponds to an unstable solution.

The described jumps only occur at a quasi-stationary change of the excitation frequency. In a real system, the amplitude is not stationary because free oscillations are initiated when jumping between different branches [143]. These fade away after some time so that the new stationary amplitude is reached. As the upward and downward jumps occur at different excitation frequencies, this oscillator shows a hysteresis.

Moreover, in Figure 3.8 stable and unstable solutions are distinguishable. An unstable solution only exists theoretically; it has never been observed in an experiment [144]. Small perturbations of the unstable solution will cause an attraction to one of the stable solutions. The derivation to differentiate stable and unstable solutions is described elsewhere [144].

Chapter 4

Methods and Materials

4.1 Methodology

The methods of investigation have to detect, represent and/or simplify the complex mechanism in the arc tube that leads to a flickering of the light. A detailed knowledge of the physical processes is crucial to understand the underlying mechanisms and, finally, to increase the efficiency of the HID lamp and/or its corresponding driver.

The small dimensions of the arc tube of HID lamps make it inaccessible for some measurement methods. Especially flow measurements, e.g. with the laser Doppler anemometry, are difficult to realise because the material of the tube wall is translucent and not transparent. Additionally, only the effects are observable and the physical processes remain concealed. Therefore, a virtual model was set up to investigate the underlying mechanisms.

Figure 4.1 sketches the concept used in this work. The model bases on the

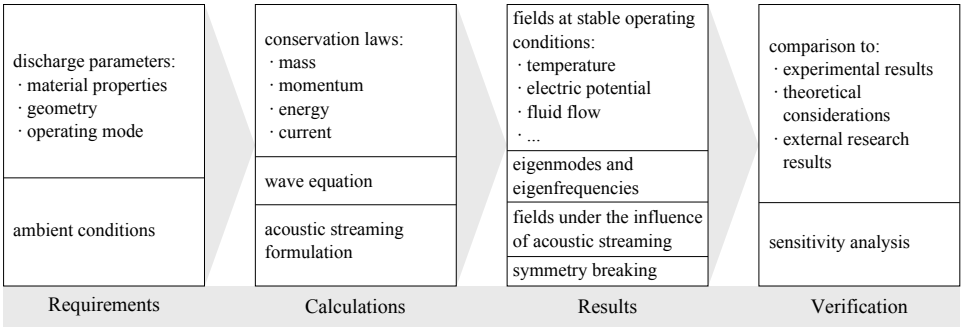

Figure 4.1. Overview of the investigations pursued in the thesis.

discharge configuration that incorporates the geometry, the material properties and the operating mode of the investigated lamp, and it has to regard the environment with appropriate conditions as well. The material properties for the interior of the arc tube and the other lamp components were measured by the manufacturer of the lamp. Prior to the calculation, the objectives have to be defined because these determine the physical processes that have to be incorporated, define the geometrical scale on which the calculations have to be conducted and limit the choice of suitable methods. In case of the research questions treated in this work (Section 2.4), the coupled solution of the conservation laws for mass, momentum, energy and charge serves to determine the input variables for the acoustic wave equation. The solution of the wave equation enables to incorporate the AS effect and, finally, to determine the stability of the calculated fields.

Other physical effects are presumably of minor importance and are not included in the model to reduce the computing time necessary to solve the problem. The model has to represent the arc tube filling domain at least. Additionally, it comprises the electrodes and the tube wall to simplify the description at the model boundaries. A suitable method to treat the problem is the finite element method, which is described in Section 4.3.1. The modelling accuracy of this method depends on the resolution of the finite element mesh and its element order as well as on the equation solver and the choice of the computational accuracy. The mesh has to be fine enough to spatially resolve the physical phenomena. In case of time-dependent calculations, the time steps have to be short enough compared to the timescale of the physical process. The validity of the physical description can only be justified afterwards and not in advance.

The results will show if the arc flicker phenomenon can adequately be described with the incorporated physical phenomena and if the research questions can be answered. Furthermore, the results will reveal if the simplifications of the model (geometry, boundary conditions, etc.) are acceptable. The accuracy of the results depends not only on the precision of the calculation process but also on the accuracy of the input data. The sensitivity analysis will highlight the influence of the material properties and the geometry on the results so that parameters can be detected, which are important to describe the flicker phenomenon.

The calculation results are mainly verified by accompanying experiments as well as by theoretical considerations and, if available, by comparison to research results of other researchers. These comparisons serve to verify the model qualitatively as well as quantitatively. For some results, no verification is possible due to

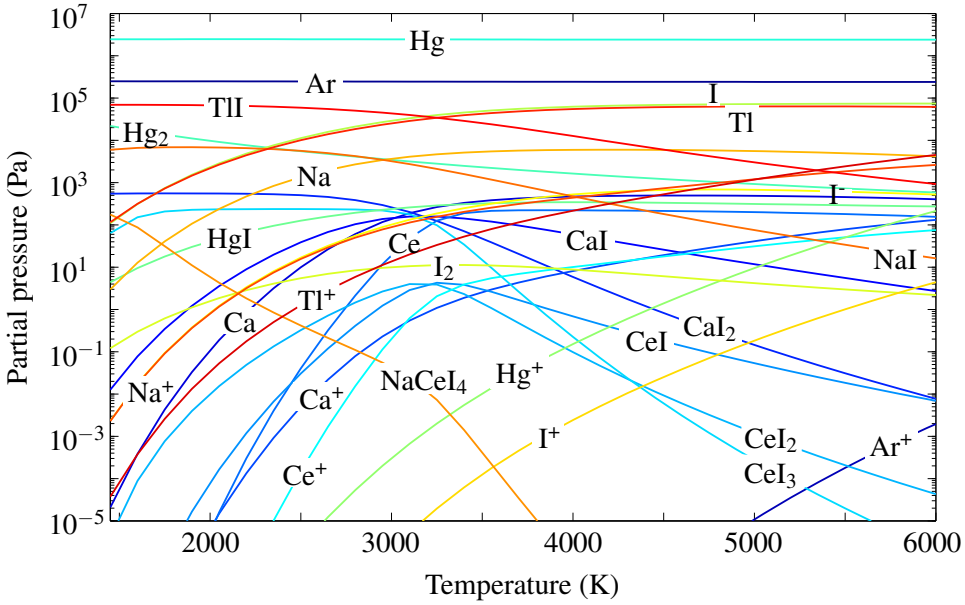

Figure 4.2. Partial pressure of the gaseous arc tube ingredients as a function of the temperature [145].

the lack of comparative data.

4.2 Material Coefficients

This section describes the material coefficients that are necessary for the simulation of the discharge arc and that occur in the partial differential equations in Section 3.1. These incorporate properties of the PCA wall, the tungsten electrodes and the arc tube filling.

The transport properties of the tube filling were derived under LTE conditions, which assumes that electrons and heavy particles possess the same temperature as mentioned in Section 3.1. Additionally, the partial pressure of each species in the discharge, which is shown as a function of the temperature in Figure 4.2, serves to calculate these properties. This data enable to calculate the material functions with the Chapman-Enskog theory [96]. The buffer gas argon possesses a partial pressure of approximately 0.24 MPa, and mercury in its ground state accounts for a partial pressure of ca. 2.4 MPa.

A sophisticated determination of the transport coefficients of the arc tube filling in HID lamps can be found elsewhere [146,147]. Here, the results, that were used in the simulation, are shown and discussed. An analysis was performed to identify

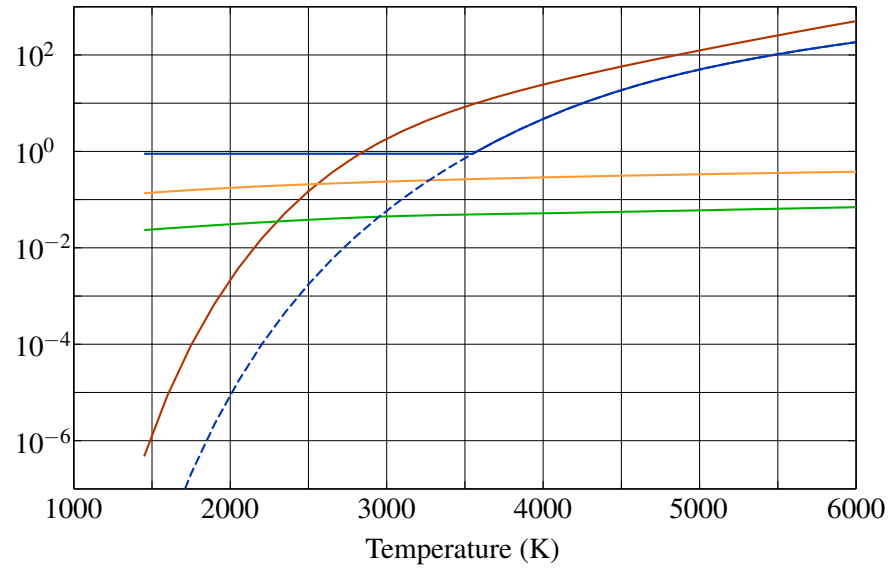

Figure 4.3. Temperature-dependency of some material properties of the tube filling. Blue: Electric conductivity ($\mathrm{S\,m^{-1}}$); green: Thermal conductivity ($\mathrm{W\,m^{-1}\,K^{-1}}$); red: Radiation loss ($\mathrm{W\,mm^{-3}}$); orange: Dynamic viscosity (mPa s).

the sensitivity of the material parameters on the temperature field and the acoustic eigenfrequencies (Section 5.3) because experimental data of the material coefficients rarely exist and theoretical data have high uncertainties since the collision cross sections for most plasma materials are unknown [34,146].

Figure 4.3 shows the temperature-dependency of some material properties. All curves start at 1450 K because this is the lowest temperature inside the arc tube at steady-state operation of the lamp. The minimum temperature defines the vapour pressure of the lamp ingredients [29,148] and is often called *coldest spot temperature*. This temperature enables adjustment of the technical properties of the lamp: Lifetime, light quality (CRI) and efficacy [35].

For the electric conductivity σ (blue curve in Figure 4.3), the assumption of LTE results in the dashed blue line for temperatures below 3550 K and in the solid line for temperatures above 3550 K. In the tube regions, where a high temperature and a high static pressure occur simultaneously, the error by taking LTE conditions is very small [38,96]. The electric conductivity decreases to values below $10^{-2}\,\mathrm{S\,m^{-1}}$ at low temperatures. These low conductivities were not measured in arc tube fillings. The LTE conditions are violated in the region between the hot plasma spots and the relatively cold electrodes [98]. A high electric field would be required to transport the electric current through this region. This would lead

to unrealistically high voltages near the electrodes that were not detected in experiments [33,98]. Moreover, an unrealistically large heat source due to Joule heating would result that would lead to severe convergence issues in the simulation. Consequently, the LTE conditions do not adequately describe the electric conductivity of the tube filling, and a non-LTE electric conductivity has to be introduced. The deviations from equilibrium can be incorporated with an additional differential equation [33,98,149]. To solve this additional equation, either a finite element mesh with up to a million degrees of freedom (see Section 4.3.1) is required, which implies a computing time of up to a couple of weeks for a 2D model [149], or a more complex approach for the simulation can be used that reduces the computing time to some days [101]*. These detailed investigations show that the electric conductivity is several orders of magnitude higher than the LTE electric conductivity and results in realistic electric fields in the near-electrode plasma. Furthermore, the investigations highlight that the non-LTE electric conductivity is nearly constant in this region. Therefore, a temperature-independent electric conductivity is assumed below a temperature of 3550 K indicated by the blue solid line in Figure 4.3. The influence of this constant electric conductivity on the acoustic eigenfrequencies and the temperature distribution inside an HID lamp were investigated [150].

Next to the electric conductivity, the green curve in Figure 4.3 shows the thermal conductivity κ of the plasma. The thermal conductivity is composed of three parts: The transport of kinetic energy, of chemical energy and of radiative energy [151,152]. The kinetic energy can be further divided into an electron and a heavy species translational kinetic energy. The chemical or reactive energy describes the energy transport during the ionisation and recombination of compounds. It becomes important for plasmas in HID lamps at temperatures above 7000 K. Depending on the temperature, the radiative energy transport can significantly increase the thermal conductivity [33,152], but in case of the investigated lamp the share of the total thermal conductivity is negligibly small. Its contribution to the total conductivity is important only if the temperature inside the arc tube exceeds 5000 K in a mercury discharge at 0.6 MPa [101] or is higher than 4000 K in a mercury discharge at 4.0 MPa [98]. In some works, a fourth transport mechanism called *internal thermal conductivity* is considered, but this effect is insignificantly small in plasmas of HID lamps [146,151].

The radiation loss q_{rad} (red curve in Figure 4.3) accounts for the radiated power inside the arc tube and serves as a sink in the Elenbaas-Heller equation (Equa-

*For the calculations, a *HP j6000* workstation with a *PA-8600* processor was used.

tion 3.5). It was determined by an Abel inversion of the measured emitted electromagnetic spectrum of the lamp [145].

The dynamic viscosity η of the tube filling (orange curve in Figure 4.3) was determined with the kinetic theory of gases [96] on the basis of the chemical composition shown in Figure 4.2.

Additionally, the specific heat capacity is represented by [145]

$$c_p(T) = \left(920 \times 10^{-7} \frac{T}{\mathrm{K}} + 110\right) \mathrm{J\,kg^{-1}\,K^{-1}}. \tag{4.1}$$

For the ideal gas law (Equation 3.9), the static pressure of $P = 2.8\,\mathrm{MPa}$ and the molar mass according to [145]

$$M(T) = \left(-161 \times 10^{-5} \frac{T}{\mathrm{K}} + 193\right) \mathrm{g\,mol^{-1}} \tag{4.2}$$

are required. To solve the wave equation (Equation 3.14), a heat capacity ratio $\gamma = 1.4$ was used.

The electrodes are made of tungsten. Their temperature-dependent thermal conductivity, which is necessary to solve the Elenbaas-Heller equation, slightly decreases from $110\,\mathrm{W\,m^{-1}\,K^{-1}}$ at 1400 K to $92\,\mathrm{W\,m^{-1}\,K^{-1}}$ at 3000 K [153,154]. The uncertainty of the thermal conductivity at these high temperature values ranges from 1 % to 5 %.

The thermal conductivity of the PCA material of the tube wall can be described by the temperature-dependent function

$$\kappa_{\mathrm{PCA}}(T) = \left(37.8 - 556 \times 10^{-4} \frac{\Delta T}{\mathrm{K}} + 282 \times 10^{-7} \frac{\Delta T^2}{\mathrm{K^2}}\right) \mathrm{W\,m^{-1}\,K^{-1}} \tag{4.3}$$

with $\Delta T = T - 273.15\,\mathrm{K}$. In Section 4.3.2, the emissivity of the arc tube wall

$$\varepsilon_{\mathrm{PCA}}(T, d_{\mathrm{wall}}) = 0.195 - \frac{0.017\,\mathrm{mm}}{d_{\mathrm{wall}}} + \frac{(110\,d_{\mathrm{wall}} + 19)\,10^{12}\,\mathrm{K^5}}{T^5\,\mathrm{mm}} \tag{4.4}$$

is used to calculate the heat radiation that is emitted from the boundary of the model through the evacuated region of the outer bulb to the ambient atmosphere with a temperature of $T_{\mathrm{amb}} = 293\,\mathrm{K}$. d_{wall} denotes the wall thickness that is 0.5 mm in case of the 35 W HID lamp.

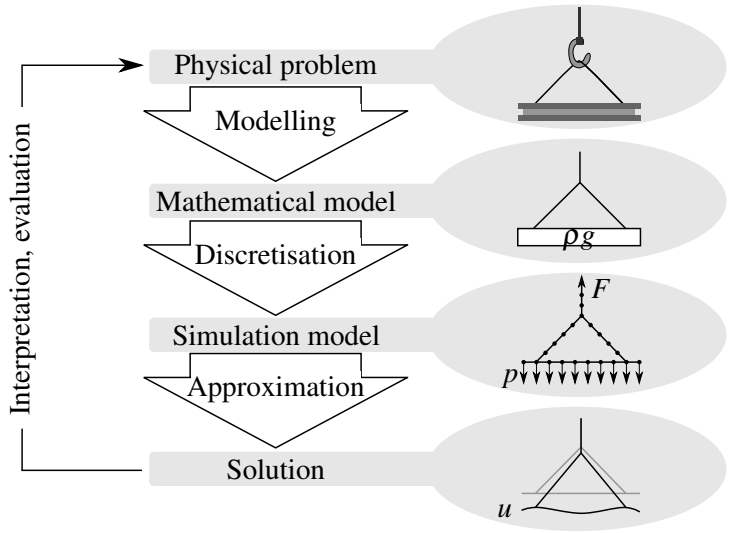

Figure 4.4. Process of the finite element analysis from the physical problem to the solution.

4.3 Simulation Model

4.3.1 Finite Element Method

To solve the differential equations for the tensor fields, different (numerical) approaches exist. In the most practical cases, an exact solution of such a problem cannot be calculated because the geometry of the computation domain is complex and/or the differential equations are nonlinear. Consequently, numerical techniques are used to approximate the exact solution. The finite element method (FEM) is a procedure to determine approximate solutions for elliptic partial differential equations. Currently, the FEM is one of the most important approximation methods to solve boundary value problems for partial differential equations. It was initially described in 1943 [155].

The FEM is mainly used in engineering analysis in which a physical field problem occurs. The method enables to identify the underlying mechanisms of the problem, determine quantities that are inaccessible for measurements, conveniently test alternative solutions to the problem, optimise structural components, reduce costs in the development phase and investigate many other issues. Figure 4.4 summarises the concept of a finite element analysis. The physical problem is usually limited to a certain region that is applied with a definite load. Originally, structural dynamic issues, in which the loads are mechanical forces, were

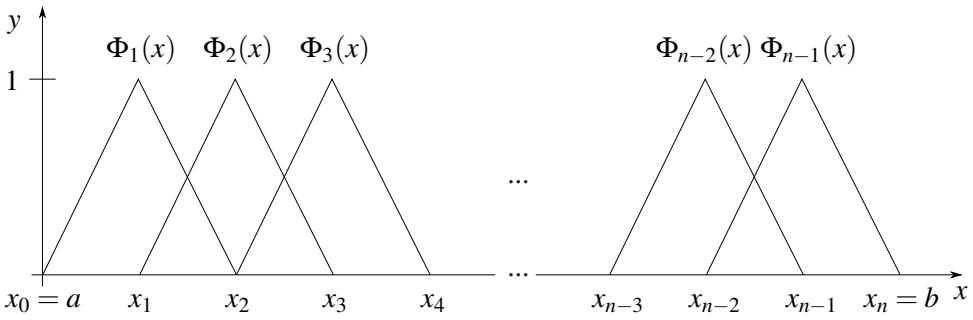

Figure 4.5. Linear functions Φ_i on subintervals of a one-dimensional domain.

solved with the FEM [156,157]. However, the FEM is not limited to this kind of investigation. A comprehensive description of the physical problem is typically so complex that it is reduced to a mathematical model which approximates the physical phenomena by differential equations. Additionally, assumptions at the model boundaries, for the initial conditions, the geometry, materials, loadings, etc. have to be made. This mathematical model is solved with the aid of FEM. The solution accuracy depends on the finite element mesh resolution of the geometry, on the order of finite elements and on the solving parameters. To increase the accuracy, a model with refined parameters has to be solved. Obviously, the solution contains all information that has been previously specified in the mathematical model. It ignores physical phenomena that were not included. Hence, appropriate assumptions for the model have to be made to completely describe the problem or, at least, to include the phenomena that are crucial to solve the problem of interest.

In the following, a summary of the basic concept of the FEM is presented. More details can be found in standard textbooks [158,159]. The keynote of the FEM is to discretise a geometrical domain into subdomains ("finite elements"), connect the simple element equations to a system of equations and solve the problem by minimising the associated residual $\mathscr{R}$ (defined later). The element equations, also called basis functions, are not globally defined in the whole problem domain, but rather locally in the subdomains. In contrast to global functions, this enables precise resolution of local effects, incorporation of different materials, solution of problems with large gradients and representation of geometrical complex issues.

In Figure 4.5 a one-dimensional interval $[a,b]$ is divided into n subintervals so that the considered space is discretised into $(n-1)$ intervals. For each point of the

interval x_i, also called node, a basis function

$$\Phi_i(x_j) = \delta_{ij} \tag{4.5}$$

(δ_{ij} Kronecker delta) is defined [148]. The simplest choice is to connect the points with piecewise linear functions on the subintervals as shown in Figure 4.5. These linear shape functions are also called triangle or hat functions [160]. Instead of linear functions, shape functions with higher-order polynomials can be used as well [161]. These require additional supporting nodes that increase the solution accuracy, but lead to a bigger system of equations and increased computing time. Practically, often smaller elements instead of quadratic or cubic shape functions are used to obtain a higher accuracy of the solution. An approximate ansatz for the solution is described by a linear superposition of shape functions

$$y_N(x) = \sum_{i=1}^{n-1} c_i \Phi_i(x), \tag{4.6}$$

so that in the case of hat functions the degrees of freedom c_i are equal to the values of the approximate ansatz y_N at the mesh points x_i. The elements with these shape functions are called Lagrangian elements.

For the determination of the unknown coefficients c_i, a variational problem is formulated. Therefore, the approximate ansatz is inserted into the sought differential equation [159–161]

$$\mathscr{L}(y(x)) = f(x). \tag{4.7}$$

$\mathscr{L}$ is the differential operator and f the source term. The Dirichlet conditions $y(x_0 = a) = 0$ and $y(x_n = b) = 0$ are defined at the boundaries. An initial choice of random coefficients c_i for the approximation solution generally results in deviations between the exact solution and the approximation so that an error

$$\mathscr{R}(\mathbf{c}, x) = \mathscr{L}(y(x)) - \mathscr{L}(y_N(x)) \tag{4.8}$$

occurs, which is named residual. It depends on the coefficients $\mathbf{c}$ and on the location x. The goal is to find coefficients that minimise the residual. For this minimisation, different approaches, like the method of least squares, the Ritz method or the Galerkin method, exist. In the following, the principle of the Galerkin method is outlined. Elliptic partial differential equations can be solved successfully with this method. Contrarily, the finite volume method is used to approximate hyperbolic

equations [160].

For the Galerkin method, the residual is multiplied with a weight function $w_k(x)$ and integrated over x. The Galerkin method uses the shape functions as weight functions. As the Galerkin method postulates that the residual is orthogonal to the weight functions [160], the integral of its product is equal to zero:

$$\int_a^b \mathscr{R}(\mathbf{c},x)\, w_k(x)\, \mathrm{d}x = 0. \tag{4.9}$$

The orthogonality of functions requires that the dot product of these functions is zero. The index k represents the nodes of the elements. The shape functions have to regard the boundary conditions of the differential equations and have to be piecewise differentiable [160].

Combining Equations 4.6 to 4.9 results in

$$\sum_{i=1}^{n-1} \int_a^b w_k(x)\, \mathscr{L}\Phi_i(x)\, c_i \mathrm{d}x - \int_a^b w_k(x)\, f(x)\, \mathrm{d}x = 0. \tag{4.10}$$

With the aid of the inner functional product

$$\langle f,g \rangle = \int_a^b f(x)\, g(x)\, \mathrm{d}x, \tag{4.11}$$

Equation 4.10 can be rewritten in the form

$$\sum_{i=1}^{n-1} \langle w_k, \mathscr{L}\Phi_i \rangle\, c_i = \langle w_k, f \rangle, \tag{4.12}$$

which is a system of algebraic equations in the form $\mathbf{A}\vec{c} = \vec{b}$ with $\mathbf{A} = \langle w_k, \mathscr{L}\Phi_i \rangle$ and $\vec{b} = \langle w_k, f \rangle$.

In scientific or engineering applications, the matrix $\mathbf{A}$ is often a large, sparse matrix. Two main categories, direct and iterative solution algorithms, exists to solve the system of linear equations. Direct solvers can be used for fully occupied matrices and attempt to compute the exact solution, whereas iterative methods are advantageous to solve nonlinear equations. The latter compute successive approximations to a solution based on an initial condition. In this work, the *PARDISO* [162,163] solver was used, which is able to solve large sparse symmetrical and unsymmetrical linear systems of equations. The solver automatically combines both solver types for large 3D systems and can reduce the computing time [164].

4.3.2 Digital Model

For the numerical investigation of the light flicker phenomenon, a model of a CMH lamp (*Philips* MASTERColour CDM-T Elite 35 W/930 [165]) was constructed. The model was set up and solved with COMSOL Multiphysics 4.4.0.195 and MATLAB 8.3.0.532. The model is described and compared to similar models used by other researchers.

The model of the arc tube is composed of three domains: The arc tube filling, the arc tube wall and the two electrodes. These three domains possess a rotational symmetry with respect to an axis that passes through the centre of the electrodes. For vertically operated lamps, 2D axisymmetric models sufficiently describe the physical processes because the direction of the gravitation equals the rotational axis. Many researchers have set up 2D models of HID lamps to solve the temperature field, the electric potential and the convection flow [19,33,71,91, 93,98,99,101,166–168] or investigated interactions of the arc with the electrode [102,103,107]. Some studies focus on acoustic eigenmodes and their corresponding resonance frequencies [71,81]. 2D models also enable time-dependent simulations [7,27,31,57,82,147,169,170] because the computing-time of these simulations is still reasonable due to a smaller number of degrees of freedom compared to a 3D model.

When the lamp is operated horizontally, the direction of the gravitation is perpendicular to the rotational axis. The buoyancy leads to an upward bending of the discharge arc that is schematically shown in Figure 4.6. Consequently, the rotational symmetry is lost, and a 3D model is required. The convection flow in horizontally operated lamps is addressed by many authors [86,94,171–176] because it essentially differs to the flow in a vertically operated lamp. Furthermore, the convection flow and the temperature distribution of both, vertical and horizontal, operating positions were compared [177]. Some 3D studies simulated acoustic eigenmodes on the basis of the rotationally unsymmetrical temperature field [78,80]. Other researchers calculated the temperature distribution of a vertically operated lamp with a 2D axisymmetric model, rotated the temperature distribution around the rotational axis, to get a 3D field, and computed the acoustic eigenmodes and eigenfrequencies in the 3D model [67]. 3D time-dependent simulations, that focus on the acoustical phenomena in the arc tube, require long computing times because of the high number of degrees of freedom. Such time-consuming simulations were not executed so far.

In this work, a 3D model was set up and simulated in horizontal operating

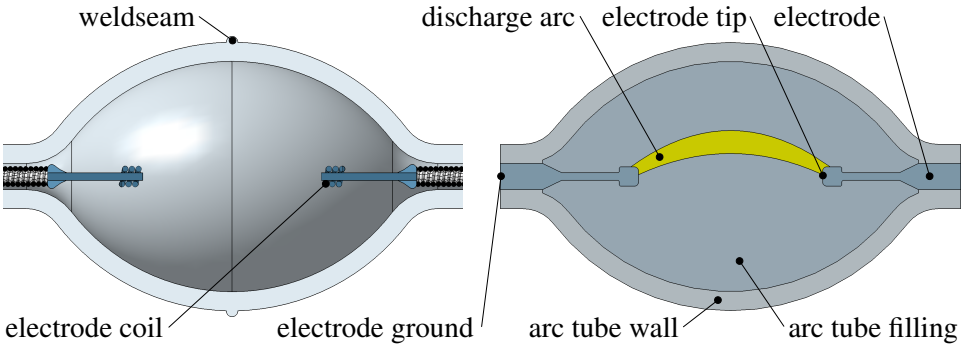

Figure 4.6. Comparison of geometries of the *Philips* MASTERColour CDM-T Elite 35 W/930 arc tube in the *y*-*z*-plane: CAD model (left), simulation model (right).

position to investigate the flicker phenomenon.

Figure 4.6 highlights the differences between the CAD model, that presents the nominal dimensions used to manufacture these lamps, and the slightly simplified simulation model of the low-wattage HID lamp. Technical drawings of both parts can be found in Appendix A. The distance between the electrodes is 4.8 mm, the outer diameter of the arc tube wall is 7.0 mm and the wall thickness is 0.5 mm. The dimension and the radii of the arc tube wall in the simulation model correspond to those of the CAD model. The small weldseam on the outer surface of the tube wall was neglected because it is suppose to have a negligibly small effect on the temperature distribution inside the arc tube. Instead of the three windings of the electrode coils, the current-carrying parts in the simulation model were created as cylinders with rounded edges to restrict the number of finite element nodes and the computing time accordingly. Moreover, the complex geometry of the electrodes at the transition to the arc tube wall were simplified. The length of model is limited to 12 mm in total. Hence, appropriate conditions at these boundaries, that are called electrode grounds, have to be defined. In addition to the geometrical differences, manufacturing tolerances lead to further deviations between the model and the real lamp. The sensitivity analysis in Section 5.3 investigates the influence of geometrical modifications and important material properties of the arc tube filling on the AR frequency, the voltage drop between the electrode, the maximal temperature and the fluid velocity inside the arc tube.

In the three model domains, several coupled partial differential equations were solved to obtain the electric potential, the velocity and the temperature field. These equations, that are discussed in Section 3.1, have to be supplemented by boundary

conditions. All terms with time-derivatives in the equations are neglected. The instability of the stationary solution is used as a criterion for flicker. Only one half of the physical geometry is considered because the stationary temperature field is symmetrical with respect to the vertical y-z-plane (Figure 4.7). Afterwards, the temperature field is mirrored at this plane to map it onto the full geometry.

The charge conservation equation (Equation 3.1) was only solved in the domain of the arc tube filling. The current transport in the electrodes is insignificant for the simulation because the electric conductivity of the tungsten electrodes is several orders of magnitude higher than the electric conductivity of the tube filling so that Joule heating in the electrodes is negligibly small. The transport coefficients are described in Section 4.2. Usually, a time-dependent electric current density has to be defined on the electrodes of the model to coincide with the experimental operation (Section 4.4). The system is symmetric on temporal average because the carrier wave at AC condition periodically changes. Therefore, it is possible to perform corresponding simulations for DC operation. The DC boundary conditions have to be set up accordingly. The Neumann boundary condition

$$\vec{n} \cdot \left(-\sigma \vec{\nabla} V \right) = J_0 \tag{4.13}$$

($\vec{n}$ normal vector) with a current density of $J_0 = 0$ is applied to the electric isolated walls and the symmetry plane. For the current-carrying surface, the electrode tip, the cylinder jacket and the rounded edge of the simplified geometry were chosen. These surfaces approximate the current-carrying surface of the electrode coil in the real lamp (Figure 4.6, left). On the electrode surfaces, the inward current density was obtained by the electrode tip area and the electric current I_{lamp}. Its value was computed with the aid of the nominal lamp power P_{lamp} and the voltage drop between the electrodes V_{drop}. For DC operation the electric current is $I_{\mathrm{lamp}} = P_{\mathrm{lamp}}/V_{\mathrm{drop}}$. A positive current density was defined on the anode surface and a negative one of the same magnitude was specified on the cathode surface. In order to preserve the model symmetry, the electric ground was defined in the centre of the model (middle plane between the electrodes: x-z-plane). Its position only determines the reference point of the electric potential, but does not influence the temperature field. The electric current density is uniformly distributed on the current-carrying surface.

The simulation of the energy conservation equation (Equation 3.5) was performed in the all three domains. The heat on the exterior surface of the arc tube

wall is only emitted by radiation

$$\vec{n} \cdot (-\kappa_{\mathrm{PCA}} \vec{\nabla} T) = \varepsilon_{\mathrm{PCA}} \sigma_{\mathrm{SB}} \left(T_{\mathrm{amb}}^4 - T^4 \right) \tag{4.14}$$

(σ_{SB} Stefan-Boltzmann constant) because the outer bulb is evacuated. The material parameters for the thermal conductivity κ_{PCA} and the emissivity $\varepsilon_{\mathrm{PCA}}$ of the PCA material of the arc tube wall can be found in Section 4.2. $\varepsilon = 0$ was specified on the symmetry plane. The ambient temperature T_{amb} was set to 293 K. Furthermore, a constant temperature of 1430 K was defined on the electrode ground surfaces. This value was adjusted to obtain the coldest spot temperature of 1450 K inside the arc tube (see Section 4.2).

When the investigations focus on the anode and cathode temperatures, a more detailed model of the heat transfer process between the electrodes and the plasma, that take cooling and heating effects by ion and electron current into account, has to be set up [33,99]. Hence, the work function of the electrode material is the decisive factor for an exact determination of the electrode temperature in these investigations [30,31,148]. The work function of a material describes the minimal energy that is needed to remove an electron from its surface. The heating and cooling effects are not included in the simulation model because the electric discharge is simulated as an averaged AC discharge so that these effects cancel each other out. Additionally, the investigations focus on the temperature of the arc tube filling, that is required to calculate the acoustic eigenmodes, and not on the electrode temperature.

The flow field in the arc tube is calculated from the compressible Navier-Stokes equation (Equation 3.6) and the mass conservation equation (Equation 3.8). A homogeneous Dirichlet boundary condition $\vec{u} = 0$ at the wall and the electrodes as well as $\vec{n} \cdot \vec{u} = 0$ at the symmetry plane was specified. The static pressure of $P = 2.8\,\mathrm{MPa}$ was defined in the lamp's centre. Similar to the position of the electric ground, its position does not influence the results. The density ρ inside the arc tube is calculated by the ideal gas law (Equation 3.9). During stable operation, the gravitational force (Equation 3.7) drives the fluid. For the horizontally operated lamp, the gravitational force points to the negative z-direction.

The finite element mesh of the 3D half model for the simulation of the temperature field (Figure 4.7) is composed of approximately 258 000 elements. Most of these are tetrahedral elements that form an unstructured mesh, which can automat-

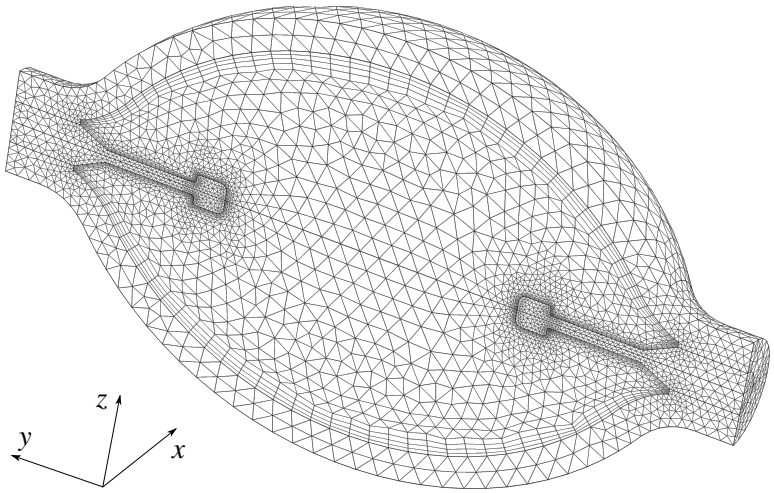

Figure 4.7. Finite element mesh for the simulation of the temperature field. The origin of the coordinate system is located in the centre of the arc tube.

ically be generated and can be refined locally. Only near the boundary to the arc tube wall, a mesh with prism elements was generated. These prism elements can better approximate the velocity drop in the boundary layer and, therefore, increase the accuracy of the solution. Furthermore, a finer mesh was created in regions where large temperature gradients occur, e.g. the area between the hot plasma and the relatively cold electrode.

The model at stable operating conditions was simulated with seven finite element mesh resolutions. Table 4.1 lists the mesh parameters and some important simulation results. The simulation results show no significant difference between all seven meshes. With the selected mesh (ca. 258 000 elements), accurate results can be obtained in a reasonable computing time of ca. 0.5 h. The computer used for the simulations was a *Fujitsu* CELSIUS R920 with an *Intel* Xeon E5-2640 processor, 16 GB memory and a *Nvidia* Quadro 5000 graphics [178]. Only the model with approximately 200 000 elements reaches convergence a little bit faster because it contains less elements in the electrodes and the arc tube wall. However, the finite element mesh in the electrodes is already very coarse so that this mesh was not used. The resulting maximal temperature, voltage drop between the electrodes and first eigenfrequency of the selected mesh differ from results with a very fine mesh (ca. 328 000 elements) less than 1 %, but the computing time with the selected mesh could simultaneously be reduced by a factor of ca. ten compared to the simulation with the very fine mesh.

Table 4.1. Influence of different finite element meshes on important arc tube characteristics. V_{drop} is the voltage drop between the electrodes, $T_{\max}$ the maximal temperature inside the arc tube, $u_{\max}$ the maximal velocity and $f_{2\mathrm{nd}}$ the frequency of the second eigenmode.

		Total number of elements						
		328 270	291 975	258 173	228 792	200 051	115 270	115 270
Mesh parameters electrodes/wall	Maximum element size (µm)	300	300	376	376	400	500	500
	Minimum element size (µm)	100	100	112	112	130	130	130
	Maximum element growth rate	1.15	1.15	1.15	1.15	1.20	1.30	1.30
Mesh parameters arc tube filling	Maximum element size (µm)	320	350	350	400	350	500	500
	Minimum element size (µm)	70	80	80	100	80	130	130
	Maximum element growth rate	1.25	1.30	1.30	1.30	1.30	1.30	1.30
Simulation results	V_{drop} (V)	76.7	76.9	76.9	76.3	76.7	76.7	76.7
	$T_{\max}$ (K)	4883	4883	4883	4892	4886	4888	4888
	$f_{1\mathrm{st}}$ (kHz)	32.858	32.861	32.865	32.865	32.873	32.912	32.907
	Computing time (s)	19 217	2451	2002	3219	1879	2714	7394

The coupled simulation of the conservation of mass, momentum, energy and charge serves to calculate the temperature distribution and the power density of heat generation inside the arc tube. To determine all acoustic pressure modes and their corresponding eigenfrequencies, the temperature field was mapped onto the full geometry. For the simulation of the homogeneous Helmholtz equation (Equation 3.18), the tube wall and the electrode boundaries are assumed to be sound hard so that the normal derivative of the pressure is zero:

$$\frac{\partial p}{\partial \vec{n}} = 0. \tag{4.15}$$

Subsequently, the inhomogeneous Helmholtz equation was solved by an eigenmode expansion of the acoustic pressure (Section 3.2.1). The solution of the inhomogeneous Helmholtz equation is available at specified points inside the arc tube only. To compute the material parameters of the volume loss factors, the volumetric mean values (Equations 3.28, 3.30) were used.

The resulting acoustic eigenmode of the simulation was normalised so that the pressure at an antinode was 1 Pa. The absolute acoustic pressure at this antinode is known from the solution of Equation 3.22. This enables calculation of the acoustic particle velocity (Equation 3.34) and the AS force field (Equation 3.32).

In a first step, only the fluid flow inside the arc tube caused by the acoustic streaming effect was considered in the simulation. The procedure is depicted in Figure 4.8 (left). Initially, the thermal plasma fields are calculated, followed by the acoustic response. Subsequently, the AS force and the corresponding velocity field are simulated. For this calculation, the half model was used again. The driving force of the fluid is composed of both, the gravitational and the AS force. To gradually increase the AS force, a control parameter $0 \leq S \leq 1$ was introduced so that the driving force is

$$f_l = S\frac{\partial \overline{\rho v_k v_l}}{\partial x_k} - \delta_{l3}\rho g. \tag{4.16}$$

the function $s(d)$ (Equation 3.36) has to be multiplied with the particle velocity without the descent to consider the exponential descent of the acoustic particle velocity towards the arc tube wall. For the implementation of this function into the simulation, the shortest distance of each point inside the arc tube to the wall is needed. This distance cannot be obtained with a standard functionality of the simulation software. For that reason, a subdomain with a thickness of $50\,\mu\text{m} \approx 10\delta_\eta$

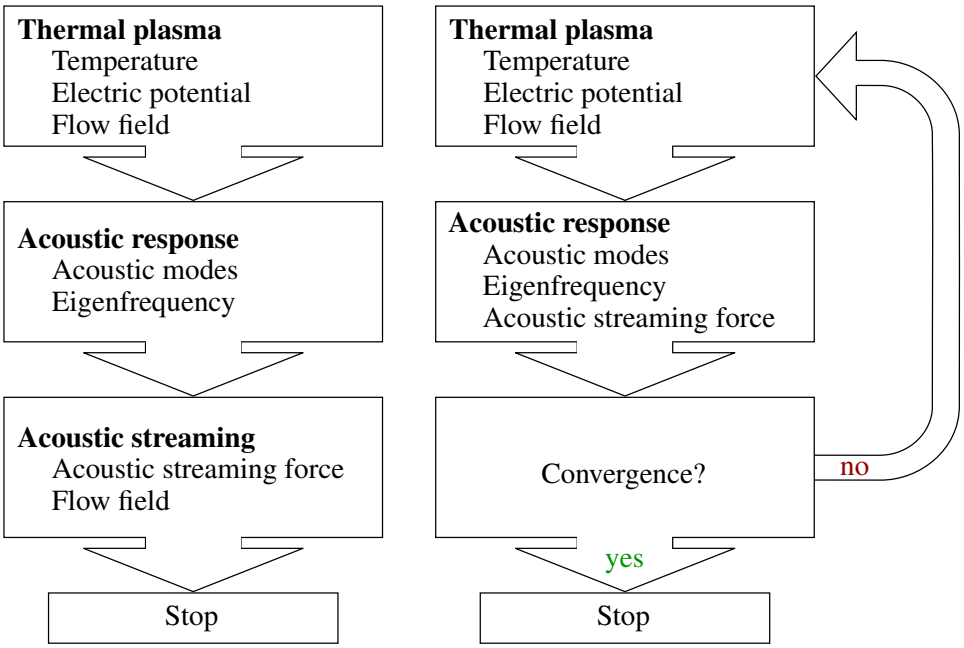

Figure 4.8. Procedure to calculate the acoustic streaming flow field (left). Simulation scheme to calculate the influence of acoustic streaming on all fields by incorporation of a recursion loop (right).

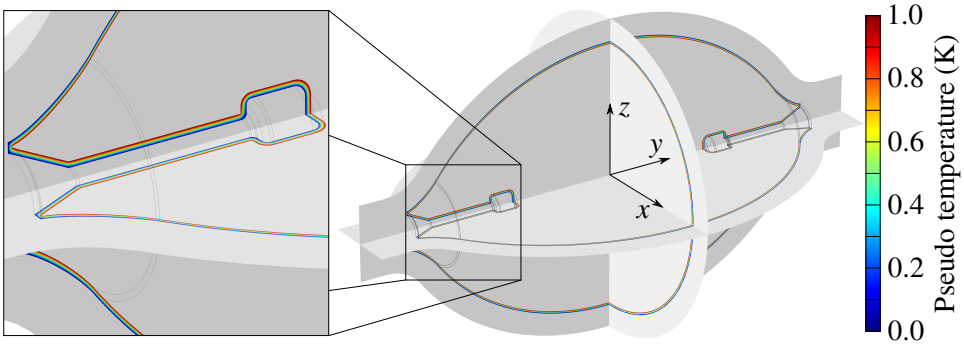

Figure 4.9. Pseudo temperature defined in the subdomain of the arc tube filling with a thickness of 50 µm.

(for δ_η see Equation 3.24) adjacent to the wall was generated. The geometry of the inner boundary layer was obtained by a geometry contraction. In this subdomain, a heat transfer model for solids with a pseudo temperature of 0 K at the outer boundary (tube's wall) and 1 K at the inner boundary (contracted geometry) was solved. The resulting auxiliary field varies linearly from zero to one and is shown in Figure 4.9. After multiplying it with the appropriate factor, the field was used as the d variable of the function $s(d)$. The finite element mesh for the simulation of the AS field is so coarse that it cannot resolve this function properly, in particular the oscillating factor. Nonetheless, it is fine enough to resolve the exponential descent, which is the important property of $s(d)$ in the present context.

In the second step, the model was extended. A recursion loop was implemented because the stationary approach does not allow for a coupling of the conservation equations and the wave equation. The procedure is depicted in Figure 4.8 (right). Instead of only simulating the velocity field under the influence of AS, the extended model additionally calculates the impact of AS on the temperature and the electric potential field. Thus, these fields, the acoustic pressure as well as the AS force are coupled, and the simulation enables determination of the stationary fields at a certain frequency. This frequency is called *excitation frequency* because the discharge arc is excited at this frequency. In contrast to the virtual control parameter S that was implemented to stepwise increase the AS force, the magnitude of the force in this simulation can be controlled by the value of the excitation frequency. When a frequency far off the resonance is chosen, the acoustic pressure amplitude and, therefore, the AS force is small. In the vicinity of the resonance frequency, the AS force is large. The lamp in this simulation is always tilted by 5° against the horizontal axis because the simulation of the AS velocity field shows instable paths that are related to a symmetry breaking transition (see Section 5.4.2).

In the initial simulation step, only the gravitation acts as the driving force of the momentum conservation. After the coupled equations for the temperature, the electric potential and the fluid flow were solved, the acoustic eigenmodes and their corresponding frequencies were calculated. Subsequently, the acoustic response function was determined. The excitation frequency, which should be chosen far off the resonance frequency at the initial step to reach convergence, defined the AS force. The recursion loop was implemented because this additional force was only calculated on the basis of the gravitational force. The temperature field, the electric potential and the fluid flow alter when the momentum conservation equation is driven by both, the gravitational and the AS force. The changed acoustic

eigenmodes and their corresponding eigenfrequencies lead to a different AS force compared to the one of the initial step. In the next iteration step of the recursion loop, this force served as the driving force. When the resonance frequencies of the current and the previous step differed less than 5 Hz, the recursion loop for this excitation frequency was successfully finished, otherwise the procedure was continued. For comparison, the investigated eigenfrequency is located at ca. 47.8 kHz. The 5 Hz-boundary acts as a convergence criterion because the results remain constant within a certain limit.

In the next step, the solution at an excitation frequency closer to the resonance frequency was calculated, i.e. the excitation frequency was increased when the resonance frequency was higher than the actual excitation frequency and vice versa. The converged results of the previous excitation frequency were taken as initial conditions. The step size was adopted according to the difference of the excitation to the resonance frequency. As the AS force significantly increases with decreasing difference of the excitation to the resonance frequency, a small step size had to be chosen to reach convergence near the resonance frequency.

4.4 Experimental Setup

The experimental setup was mainly used to determine the acoustic eigenfrequencies of the arc tube of the HID lamp. Additionally, the setup served to investigate the hysteresis effect (Section 5.5). Optical measurement devices were implemented in this setup to detect the emitted light of the discharge arc during stable and unstable operation.

Figure 4.10 schematically depicts the experimental setup that consists of the HID lamp itself, the equipment necessary to operate the lamp and different measurement devices. Furthermore, the manufacturer and the product name are presented. The HID lamp, a *Philips* MASTERColour CDM-T Elite 35 W/930 [165], was operated at a square-wave voltage with a carrier frequency $f_c = 400\,\text{Hz}$. The square-wave signal was provided by an *Agilent* 33 220A function generator with a rise and fall time of less than 13 ns and an overshoot of less than 2 % [179]. No instabilities of the discharge arc occurred at f_c because the driving frequency was considerably smaller than the lowest acoustic eigenfrequency at approximately 42 kHz. The second function generator, a *Wavetek* Model 29A, produced a sinusoidal voltage with a resolution of 0.1 mHz [180] that was used to excite discharge arc flicker. For this reason, the frequency of this signal is also called *excitation*

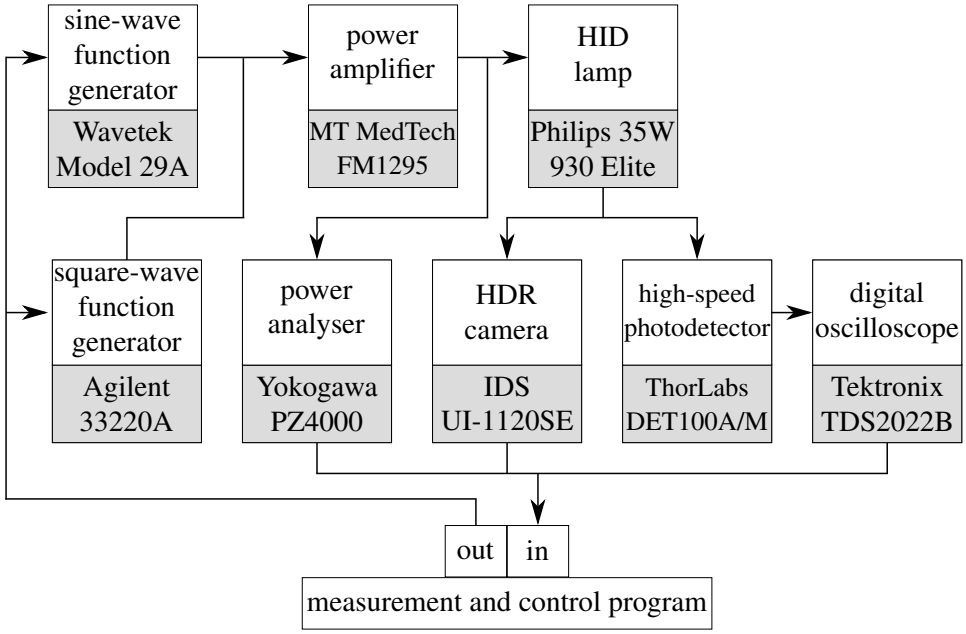

Figure 4.10. Experimental setup to characterise discharge arc flicker in HID lamps.

frequency f_{ex}. It was tuned to different frequencies in a certain high frequency range. In case of the investigated 35 W lamp, the frequency was varied between 35 kHz and 50 kHz. The superposition of both voltage signals is described by ($\omega_{\mathrm{ex}} = 2\pi f_{\mathrm{ex}}$, $\omega_{\mathrm{c}} = 2\pi f_{\mathrm{c}}$):

$$V(t) = \begin{cases} \hat{V}\left[+1+\alpha\sin\left(\omega_{\mathrm{ex}}t\right)\right] & 2n < \omega_{\mathrm{c}}t \leq 2n+1 \\ \hat{V}\left[-1+\alpha\sin\left(\omega_{\mathrm{ex}}t\right)\right] & 2n+1 < \omega_{\mathrm{c}}t \leq 2n+2 \end{cases} \qquad n \in \mathbb{N}_0. \quad (4.17)$$

The power amplifier, a *MTMedTech* FM1295 [181], regulated the amplitude $\hat{V}$ of the voltage $V(t)$ and the electric current $I(t)$ so that the HID lamp was operated at its nominal power. The modulation depth α describes the ratio of the sinusoidal to the square-wave voltage amplitude. The power can be derived from $P(t) = V^2(t)/R_{\mathrm{plasma}}$ with the electric resistance of the plasma R_{plasma}. The power analyser, a *Yokogawa* PZ4000 [182], measured the following data: The electric current, the electric potential drop between the electrodes and the electric power.

The high dynamic range (HDR) camera, a *IDS* UI-1120SE, enables direct observation of the discharge arc because it can resolve the high brightness differences between the arc and its surrounding. The CMOS chip of the camera is sensitive in the wavelength range of 400 nm to 900 nm with the highest sensitivity at 710 nm,

has a resolution of 768×576 pixels and a high dynamic range of 120 dB [183]. The maximal refresh rate of the camera is 50 Hz [183], i.e. it can record up to 50 images per second. The optical measurements were used to detect the light intensity distribution, the shape of the discharge arc and the arc deflection in case of a horizontally operated lamp.

When the discharge arc flicker was investigated experimentally, both the camera and the high-speed silicon photodetector, a DET100A/M from *ThorLabs*, were used. The photodiode with a rise time of 43 ns converts the brightness fluctuations into an electric current. The spectral sensitivity is 400 nm to 1100 nm with a peak wavelength at 970 nm [184]. The photodiode was placed in a distance of 0.2 m from the HID lamp to receive enough illumination and simultaneously to prevent saturation. The digital oscilloscope, a *Tektronix* TDS2022B [185], records the time-dependent signal and converts it into the frequency domain by fast Fourier transform (FFT). A computer transmitted the values of the modulation depth and the excitation frequency to the function generators and records the camera and photodiode signals as well as the electric current, electric potential drop and electric power. To control the experimental setup, program code created with MATLAB was used.

To determine the acoustic eigenfrequencies that lead to a flickering discharge arc, the lamp was initially operated at a modulation depth of 0 % for at least ten minutes. The lamp reached a stationary state at this stable condition, which means that the temperature inside the arc tube, the voltage drop between the electrodes, the irradiated light, etc. do not change any more.

The constant electric potential drop between the electrodes without acoustic excitation is defined as the reference voltage V_{ref}. In case of the exemplary measurement in Figure 4.11, V_{ref} is 90 V ($f_{\mathrm{ex}} = 40.0\,\mathrm{kHz}$, $\alpha = 0\,\%$). The electric potential is proportional to the arc length because the passage of current through the plasma acts as an ohmic resistance [38]. Therefore, arc flicker can directly be observed by measurement of the voltage drop. After the stationary state was reached, f_{ex} was set to a constant value near an acoustic eigenfrequency of the lamp and α was stepwise increased every 10 s to excite acoustic waves. Meanwhile, the potential drop was measured every 0.5 s, and the power was regulated to keep it at its nominal value. When the voltage fluctuated more than $V_{\mathrm{fluc}} = 1.5\,\mathrm{V}$ or when the voltage exceeded $V_{\mathrm{lim}} = V_{\mathrm{ref}} + 5.0\,\mathrm{V}$, the measurement was aborted to prevent lamp failure caused by exceedingly high arc tube temperature or by temperature oscillations of the arc tube. Immediately afterwards, α was set back to 0 % and f_{ex}

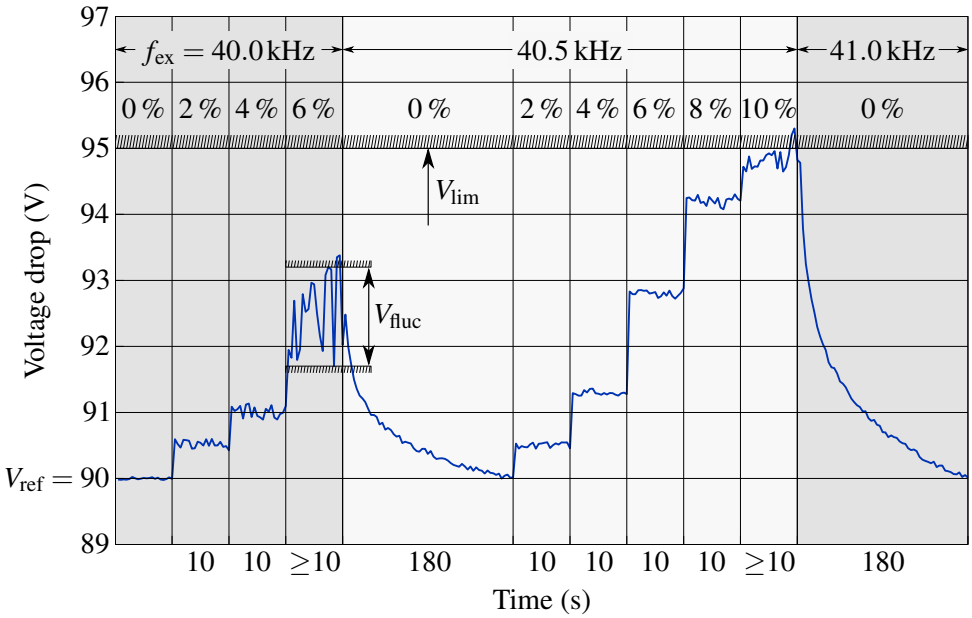

Figure 4.11. Exemplary behaviour of the voltage drop during determination of acoustic eigenfrequencies.

was increased to the next frequency step. Additionally, an upper limit of $\alpha = 12\,\%$, which is sufficient to excite ARs [44], was defined to restrict the duration of the experiment.

Figure 4.11 displays both cases of measurement abortion. A voltage fluctuation of more than V_{fluc} occurs at $f_{ex} = 40.0\,kHz$ and $\alpha = 6\,\%$, and the voltage limit V_{lim} is exceeded at $f_{ex} = 40.5\,kHz$ and $\alpha = 10\,\%$. For the 35 W lamp, the excitation frequency was generally increased from 35 kHz to 50 kHz in 500 Hz-steps to excite the first instability at around 42 kHz (see Section 5.2.2). The modulation depth was increased from 0 % to 12 % in 2 %-steps.

A different measuring procedure was used to detect the hysteresis effect (Section 5.5). The starting phase and the definition of V_{ref} are the same as in the procedure used to measure ARs. Instead of varying the modulation depth at a constant excitation frequency, the modulation depth was set to a constant value, which had to be high enough to stimulate arc flicker. The excitation frequency was increased from low frequencies and decreased from high frequencies. These procedures are also called forward and backward frequency sweeping [62]. In both cases, the investigated resonance frequency lies between the starting and ending frequency. The initial excitation frequency was set to a value some kHz off the resonance frequency. For the 35 W lamp, 37 kHz were used for forward and 47 kHz for back-

ward sweeping. At each frequency step, the potential drop was measured every 0.5 s, and the power was regulated to keep it at its nominal value. The step size of the frequency was 50 Hz. The dwell time at these conditions was 10 s so that the lamp was able to reach a stationary state, which means that the temperature inside the arc tube, the voltage drop between the electrodes, the irradiated light, etc. do not change any more. If one of the voltage measurements exceeded the reference voltage by 8 V or if the voltage fluctuated by more than 1.5 V, the experiment was terminated. When none of these criteria was fulfilled, the experiment was continued until the excitation frequency reached 37 kHz and 47 kHz, respectively.

The camera was used for two investigations: (1) brightness measurements were performed at stable operating conditions (no acoustic excitation, i.e. $\alpha = 0\,\%$) when the lamp had reached its stationary state. These experimental results serve to validate the stationary simulation results (Section 5.1.2). (2) videos of the flickering discharge arc were recorded. These results were compared to the simulation results that incorporate the AS effect (Section 5.5). Furthermore, the brightness fluctuations were simultaneously recorded with the photodiode to test if light intensity fluctuation and discharge arc motion correspond.

Chapter 5

Results

5.1 Discharge Arc at Stable Operating Conditions

The investigations of the HID lamp operated at stable operating conditions serve to qualitatively and quantitatively validate the simulation model. For this purpose, accompanying experiments were performed. Additionally, results of similar investigations of other researchers are evaluated. The results of all investigations are compared and discussed.

5.1.1 Simulation

The model includes the calculation of the flow field, the electric potential and the temperature field to simulate the discharge arc at stable conditions. Therefore, the coupled system of differential equations, that describe the conservation of charge, energy, momentum and mass, complemented by the ideal gas law, have to be considered. The equations, their corresponding boundary conditions and the material coefficients have already been described in Sections 4.2 and 4.3.2. These serve to define the conditions in all FE nodes and to set up the system of equations. The solution process of this stationary step is summarised in Appendix B. The solution contains the electric potential, the flow field as well as the temperature field that serves to determine the space-dependent gas density and speed of sound for the calculation of the acoustic eigenmodes and the corresponding frequencies, which are presented in Section 5.2.

Figure 5.1 shows the electric potential field inside the arc tube. Since the electric ground was placed in the centre point and the model is symmetric with respect to the x-z-plane (see Figure 5.9), the electric potential equals zero in this plane.

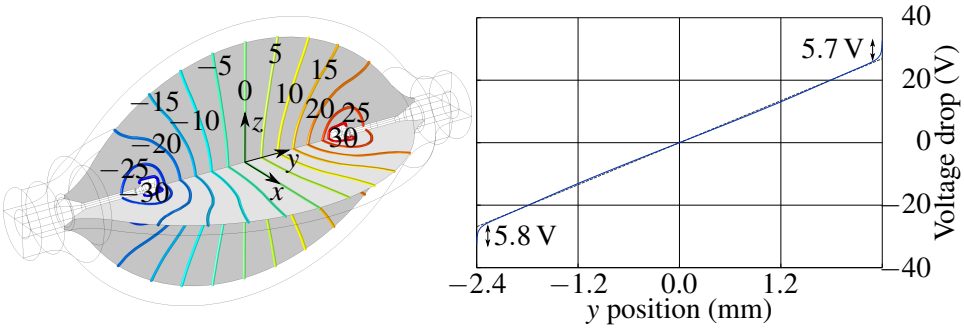

Figure 5.1. Electric potential inside the arc tube of the HID lamp at stable operating conditions. Left: Contour lines on the x-y- and y-z-plane of the 3D model. The contour lines for ± 35 V and ± 40 V are not shown because these are practically identical with the ± 30 V lines. Right: Electric potential drop between the electrode tips along a line defined by $\vec{r} = (0, y, 0)^{\mathrm{T}}$ mm.

The definition of the current density at the electrodes with inverse signs (Equation 4.13) leads to positive voltages at the one electrode and negative voltages at the other electrode. The absolute voltages are symmetric to the x-z-plane, i.e. the absolute voltage at the point $\vec{r} = (x, y, z)^{\mathrm{T}}$ equals the absolute voltage at the point $\vec{r} = (x, -y, z)^{\mathrm{T}}$.

Additionally, Figure 5.1 (right) shows the voltage drop between both electrodes that linearly increases in the discharge arc except for a small region in front of the electrodes. Here, much higher electric field strengths are required to transport the charged particles. This behaviour was detected and described in other investigations of HID lamps as well [39,101,102]. The simulation results in electrode sheath voltages of over 5 V that slightly differ due to the limited accuracy of the simulation. The minimum and maximum voltages in the arc tube occur not directly at the tip of the electrodes because the current-carrying surface was defined to be the electrode tip as well as the cylinder jacket. Therefore, the total voltage drop in the simulation results in 83.0 V.

The source term of the energy conservation equation (Equation 3.5) is the difference of the ohmic loss generated by the ohmic resistance of the plasma and the temperature-dependent emission (Section 4.2, Figure 4.3). As the electric field strength is maximal in the electrode sheath, the majority of the 35 W is induced here. This leads to high temperature peaks of approximately 4800 K that can be observed in Figure 5.2. These temperature peaks are also called *hot plasma spots*. The temperature of the discharge arc is approximately 4200 K and decreases in the direction of the arc tube wall that has a minimum temperature of 1450 K, which

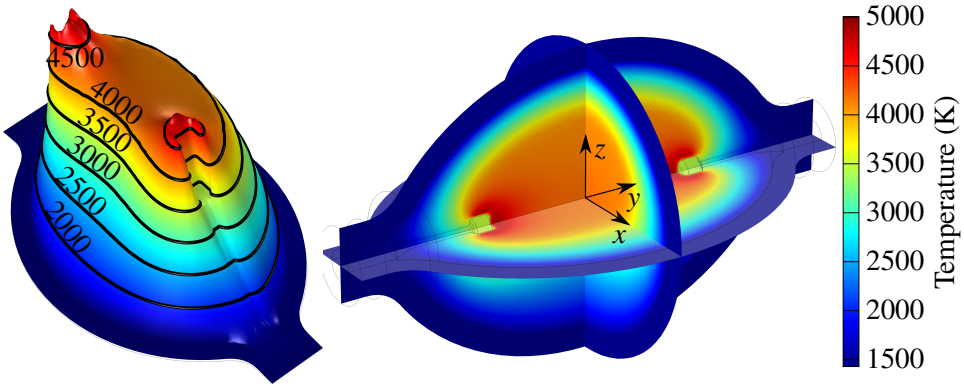

Figure 5.2. Temperature field inside the arc tube of the HID lamp at stable operating conditions. Left: Temperature distribution in the y-z-plane figured as height expression. Right: Temperature distribution in the three planes (x-y-, y-z-, x-z-plane).

represents the previously specified coldest spot temperature that defines the vapour pressure of the lamp ingredients. Due to the buoyancy caused by the gravitational force, the discharge arc is bent upwards (positive z-direction) off the geometrical symmetry axis. Consequently, the temperature gradient from the discharge arc to the upper wall is larger than the gradient from the discharge arc to the lower wall. The temperature drops from the hot plasma spots to 3460 K at the electrode tip. The spatial distance of these temperature values is only 120 µm so that a large temperature gradient occurs. The distance matches simulation results with a similar HID lamp configuration with a nominal power of 100 W that determined 100 µm to 250 µm [99] or 30 µm to 150 µm [100], respectively.

The temperature distribution of Figure 5.2 already indicates the convection flow inside the arc tube. During stable operation, solely the gravitational force drives the fluid. The temperature in the discharge arc is higher than in the vicinity of the wall, i.e. the mass density inside the discharge arc is lower. This leads to an upward-directed, laminar flow in the centre of the arc tube (Figure 5.3). The fluid flow in the vicinity of the wall is directed downwards. The maximal velocity of this buoyancy-driven flow is 85 mm s^{-1} and occurs 0.26 mm above the lamp centre. Figure 5.3 also demonstrates the necessity of a 3D model. The upward bending of the temperature field leads to a field that is not rotationally symmetric according to the y-axis any more. This rotational symmetry is mandatory for a 2D axisymmetric model. Consequently, all three spatial dimensions are required to adequately describe the HID lamp operated horizontally.

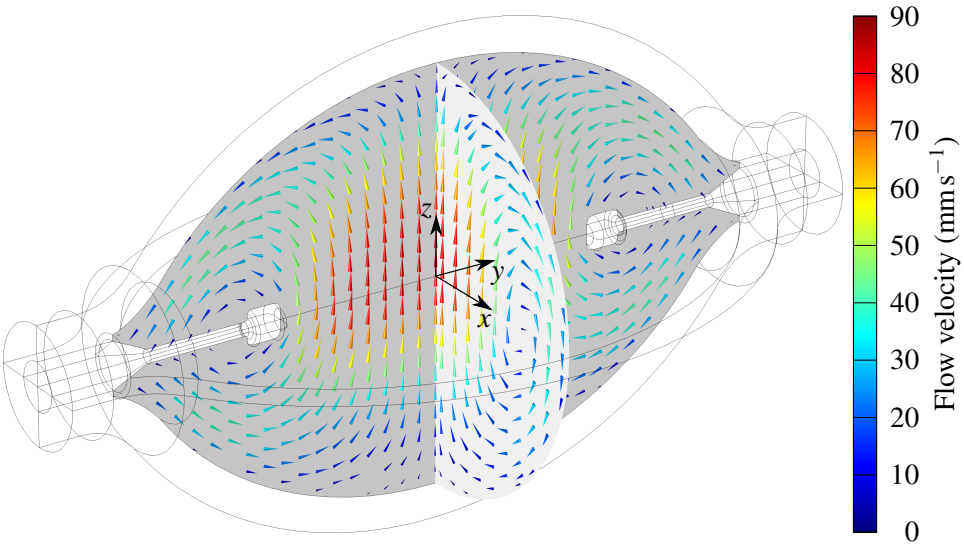

Figure 5.3. Convection pattern inside the arc tube of the HID lamp at stable operating conditions represented by the x-z- and y-z-plane.

The investigations of the temperature and the flow field reveal that the results are symmetric to the x-z-plane and the electric potential is antisymmetric. Hence, a 3D quarter instead of a half model is sufficient to describe the HID lamp at stable operating conditions. Nevertheless, the model dimension was retained because the symmetry breaking phenomenon described in Section 5.4 leads to unsymmetrical fields that would not be adequately described by a quarter model.

To compare the simulation results and the experimental light intensity measurements presented in the next section, two methods were selected. The first method determines the maximal temperature values in x-direction for each pair of y/z coordinates. The y-z-plane equals the focal plane of the camera. The highest temperature values are selected because these emit a large ratio of the radiation.

For the second method, the emitted radiation of the discharge arc is simplified as a Planck radiator so that the light emission in a specific wavelength range can be calculated on the basis of the temperature. Therefore, the total emission (Equation 3.11) is calculated in each finite element node. The lower bound of integration in Equation 3.11 is set to 400 nm and the higher bound to 900 nm in accordance with the spectral sensitivity of the camera [183]. The resulting emission is integrated in x-direction.

Figure 5.4 shows the results of both methods. The distance of the black curves in the figure to the horizontal symmetry axes (y-axis) is defined as *arc deflection*.

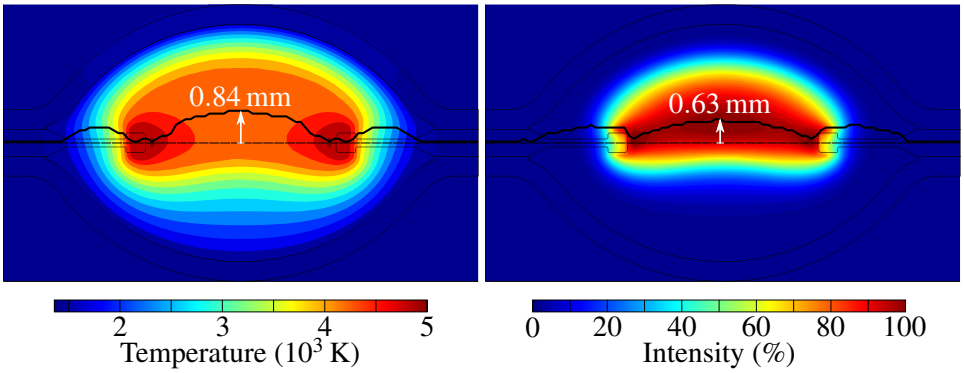

Figure 5.4. Determination of the arc deflection: Maximal temperature values in 250 K-steps projected onto the y-z-plane (left). Integration of the black-body radiation in the x-direction (right). The black line indicates the mean position of all values that are larger than 95 % times the highest value as a function of the y-coordinate.

Due to the symmetry of the model and the results, the arc deflection is maximal in the centre ($y = 0$ mm) of the arc tube. In case of the projected maximal temperature values, the maximal arc deflection is 0.84 mm. When assuming the lamp as an ideal Planck radiator, the maximal arc deflection is only 0.63 mm and, thus, 25 % smaller. In contrast to the distinctive hot plasma spots in Figure 5.4 (left), the integrated power density in Figure 5.4 (right) shows a consistently high radiation density between the electrodes. Moreover, the high gradient towards the arc tube wall leads to the impression of a constricted arc. The constriction is caused by the power, which is proportional to T^4 (see Equation 3.11) so that the contribution of temperatures below 3000 K to the sum of radiated power is negligibly small.

5.1.2 Experiment

For the measurement of physical quantities at stable conditions, the lamp was operated at a square-wave voltage with a carrier frequency of 400 Hz and at the nominal lamp power of 35 W. The electric potential drop and the electric current were measured with the power analyser. The light intensity was recorded by camera. Its focal plane was aligned to be parallel to the y-z-plane of the arc tube. For the maximal image contrast, the aperture was adjusted so that the saturation was reached at the point with the highest light intensity. In the x-y-plane, no arc deflection occurs at stable conditions. This was confirmed by top-down light intensity measurements. The experiments were performed for twelve lamps of the same kind.

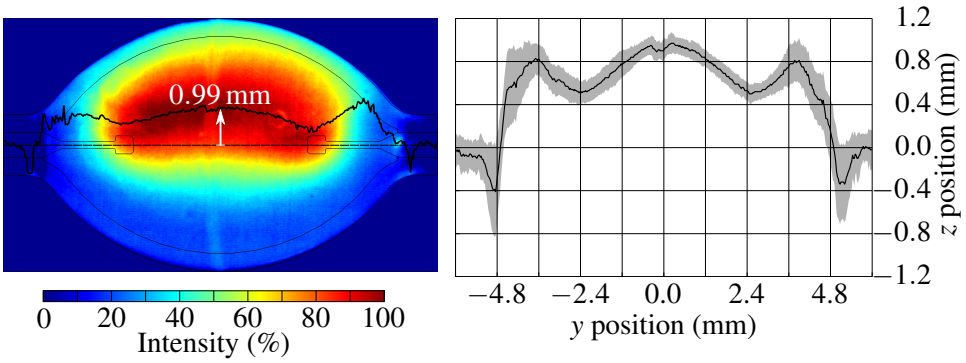

Figure 5.5. Experimental determination of arc deflection at stable operating conditions. Left: Exemplary light intensity measurement of a horizontally operated HID lamp. The black line indicates the mean position of all light intensity values that are larger than 95 % times the highest light intensity as a function of the y-coordinate. Right: Average (black line) and standard deviation (grey area) of the arc deflection of twelve lamps.

Measurements of the electric potential over time reveal that a fully stationary state is never reached. Even at stable operating conditions, the voltage drop between the electrodes slightly changes. The voltage varies by up to 2 V within a time frame of a few minutes. Therefore, the mid-range voltage calculated from the maximum and minimum value for each lamp is determined and used hereinafter. The stationary voltage of the lamps ranges from 88.6 V to 94.2 V. As the plasma acts as an ohmic resistance, the voltage drop depends on the "length" and the "cross-section" of the discharge arc. These hypothetical values are influenced by the geometry of the arc tube, the distance of the electrodes, the amount and composition of the plasma ingredients, etc. and are subject to tolerances in the manufacturing process. The mean value and standard deviation for all twelve samples is (91.3 ± 2.1) V. Furthermore, the voltage drop depends on the lamp age. Similar lamps have shown a voltage drop of 78 V when operated for 200 h and 85 V after 8000 h of operation [65].

The main results of the optical measurements are presented in Figure 5.5. The fluid flow bends the discharge arc upwards so that an arc deflection of 0.99 mm at $y = 0$ mm occurs in the exemplary image shown on the left-hand side of the figure. Additionally, this image illustrates the translucency of the tube wall [60]: The image is not sharp, but blurred. As the arc tube consists of two welded half-shells, the weld seam refracts the light. Consequently, a lower intensity in the z-direction is measured that appears as a vertical stripe at $y \approx 0$ mm.

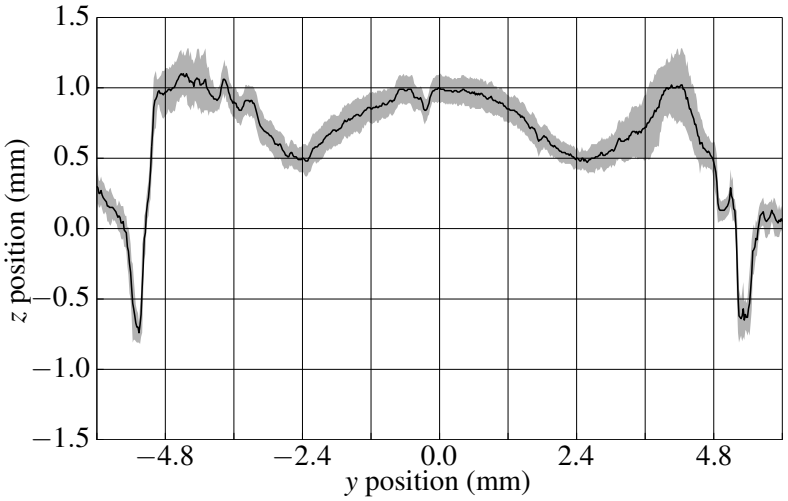

Figure 5.6. Experimental determination of arc deflection at stable operating conditions. Average (black line) and standard deviation (grey area) of the arc deflection of lamp sample 1 measured ten times. The electrode gap is between $y = -2.4\,\text{mm}$ and $y = 2.4\,\text{mm}$.

The right-hand side of the figure shows the arc deflection measurements of all twelve samples. The black line indicates the mean position of all light intensity values that are larger than 95 % times the highest light intensity as a function of the y-coordinate. Additionally, the standard deviation of the arc deflection is displayed in grey. The light refraction due to the weld seam can be observed in the graph as well. It shows up as a small dip at $y \approx 0\,\text{mm}$. The essential segment is the inter-electrode region that ranges from -2.4 mm to 2.4 mm. Here, the maximal arc deflection is 0.96 mm on average. The standard deviation of the arc deflection in the inter-electrode region is nearly constant and has a value of 0.10 mm. Furthermore, the figure reveals that the arc deflection at the electrode tips does not approach $z = 0\,\text{mm}$, but is rather located 0.52 mm above the electrodes.

In addition to the experimental investigations of all samples, the arc deflection of one lamp was measured ten times including switching off the lamp between the measurements. The resulting arc deflection diagram is shown in Figure 5.6. The results are similar to those presented in Figure 5.5: The maximal arc deflection between the electrodes is (1.00 ± 0.10) mm and the arc deflection is (0.50 ± 0.09) mm at the electrode tip.

5.1.3 Comparison and Discussion

The results of the discharge arc at stable operating conditions have shown similarities and differences in the simulations and experiments. The results of the voltage drop, the temperature field and the arc deflection are compared and discussed.

The resulting voltage drop in the simulation (83.0 V) is 9.1 % smaller than the mean potential drop measured in the experiments (91.3 V). In the model, the geometry of the electrodes was fundamentally simplified. This is associated with a significantly lower number of degrees of freedom of the finite element mesh, but has the drawback of an inaccurate computation of the voltage drop in this area. Moreover, the simulation does not consider the diverse effects in the plasma sheath directly in front of the electrodes [105]. Due to the simplification of the electrode geometry to a cylinder and the definition of the front and the lateral surface as the current-carrying parts, it cannot be expected that the electric field near the electrodes is calculated accurately. Nonetheless, a more detailed electrode geometry and a sheath model are not incorporated in the model because these are of minor importance for the simulation of the flicker phenomenon. The temperature-dependent electric conductivity and the simplified definition of the non-LTE electric conductivity can also be a source of inaccuracies. The influence of the transport coefficients and main geometrical dimensions on the voltage drop is described in Section 5.3.

The temperature inside the arc tube is crucial for the determination of the electric field because the electric conductivity is temperature-dependent. The temperature of the discharge arc is approximately 4200 K and the temperature of the hot plasma spots is around 4800 K. Compared to the simulated arc tube temperatures of an HID lamp of similar type [33], these temperatures are relatively low. It has been reported that the hot plasma spots have a maximum temperature of 7500 K, and the temperature of the discharge arc is approximately 5200 K.

The reasons for the lower temperature of the discharge arc are mainly caused by the transport coefficients and temperature-dependent material parameters that are input variables of the simulation and were externally derived [145]. The most important parameters are the thermal conductivity of the arc tube filling and the power that is emitted by radiation. The influences of these variables on the temperature are described in Section 5.3.

The temperature in the vicinity of the electrodes is mainly affected by the shape of the current-carrying part of the electrode, e.g. the hot spot temperature is much higher when the electrode tip has a conical instead of a flat form [101]. Therefore,

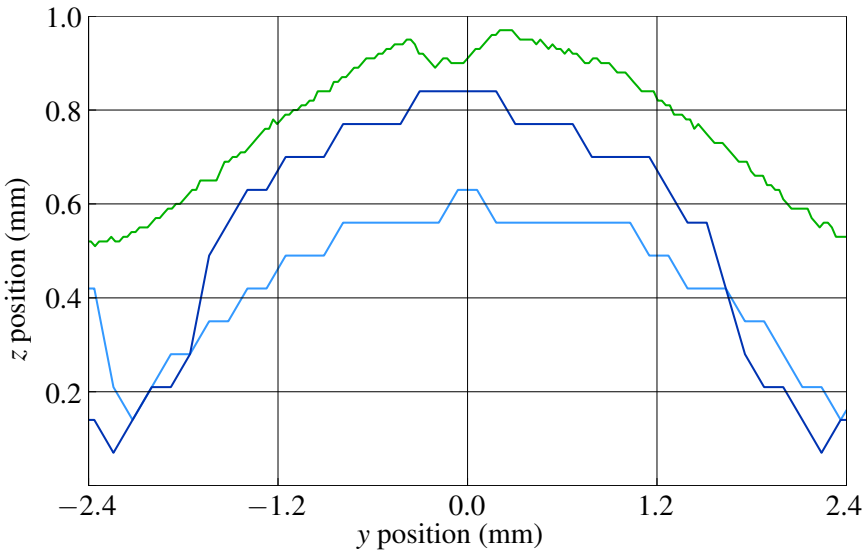

Figure 5.7. Comparison of arc deflection curves: The experimental result of the light intensity measurements (green), the projected maximal temperature values (dark blue) and the integrated Planck radiation (light blue).

the resulting lower hot spot temperatures are caused by the simplified electrode geometry already mentioned before. Recent simulations with the same geometric model, in which only the electrode tip and not its lateral surface was defined as current-carrying part, have shown that a much higher hot spot temperature of 6900 K can be obtained and that the temperature of the discharge arc likewise increases to 4300 K. Such a model requires additional finite element nodes to resolve the higher temperature gradient between the increased hot spot temperature and the relatively cold electrode tip. Hence, the solving time significantly increases.

The comparison of the resulting arc deflections presented in Figure 5.7 between the simulation and the experiment shows differences. The maximal deflection obtained with the projected maximal temperature values (0.84 mm) is 11.6 % smaller than the mean arc deflection measured in the experiments (0.95 mm). The approach, which simplifies the discharge arc as an ideal Planck radiator, has a maximal arc deflection (0.63 mm) that is 33.7 % smaller. In the near-electrode region, differences between the arc deflections can be observed as well. The measured light intensity distribution has its maximum at $z = 0.52\,\text{mm}$, whereas both simulation results drop down to $z \approx 0.1\,\text{mm}$. However, the shape of the arc deflection curves of the integrated Planck radiation and the light intensity measurement show good accordance. When the arc deflection curve of the integrated Planck radiation is dis-

placed by 0.3 mm in the positive z-direction, both curves match perfectly. These similarities can also be seen in the intensity distributions in Figures 5.4 (right) and 5.5 (left). The maximal intensity occurs in the discharge arc and is consistently high. The plasma hot spots near the electrodes are not visible as it is the case for the maximal temperature values in Figure 5.4 (left).

The reasons for the arc deflection differences are diverse: The main reason is that the measured and the simulated quantities differ (light intensity vs. maximal temperature values or idealised Planck radiation, respectively). Hence, no perfect accordance can be expected. Another important reason is that the PCA material of the arc tube is not transparent, scatters the light and, therefore, is inappropriate for optical diagnostic measurements. Additionally, the round surface of the arc tube and the outer wall refract the emitted light so that the arc deflection observed from the outside is different to the one inside the tube. Particularly, the results in the vicinity of the electrodes are distorted when the electrode is composed of a rod and a coil [30], which is the case for the investigated HID lamp. In the simulation model, these optical effects are not included and the electrode geometry is simplified. Due to the relatively low temperature of the arc tube filling in the model compared to results of a similar lamp [33], the impact of the gravitational force is low. Thus, a higher temperature difference between the plasma and the arc tube wall would be equivalent to an increasing buoyancy that would lead to a higher fluid velocity and a larger arc deflection. The effect would be dampened by an increasing heat loss that results from the increasing temperature gradient near the wall [36]. Furthermore, the emitted light of an HID lamp was only approximated by a Planck radiator. The material-specific discrete emission lines are not considered.

Despite the quantitative deviations between experiment and simulation, the model qualitatively describes the important physical phenomena and, therefore, is retained for the subsequent simulation steps. Furthermore, the investigations focus on the flicker phenomenon that is qualitatively not affected by the differences of the discharge arc at stable operating conditions.

5.2 Acoustic Response

In the experiments, the impact of the acoustic excitation on the electric parameters of the discharge arc are measured. To compute the acoustic response, an eigenvalue analysis is performed that bases on the temperature field as described

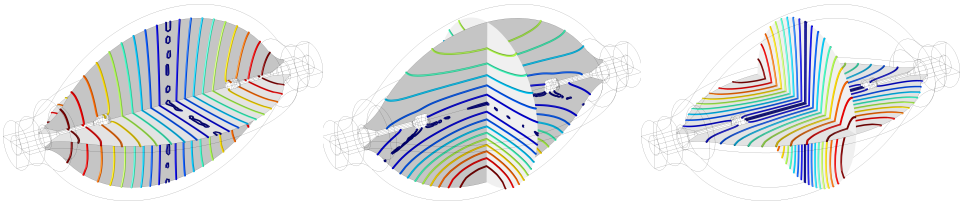

Figure 5.8. Simulation results of the three acoustic eigenmodes corresponding to the lowest eigenfrequency. The images illustrate the absolute value of the acoustic pressure $|p|$. Blue indicates $|p| = 0$ and red the maximum of $|p|$. The corresponding frequencies are: 33.1 kHz (left), 47.8 kHz (middle), 48.1 kHz (right).

in Section 5.1.1. The results of the simulation and the experiments are compared.

5.2.1 Finite Element Calculations

The acoustic response was determined in the complete 3D model of the arc tube to obtain the modes that have an acoustic pressure node in the y-z-plane. For its determination, the formulae in Section 3.2.1 were used. As the mass density and the speed of sound are temperature-dependent, the calculated temperature distribution was mirrored at the y-z-plane to make it available in the full domain.

In Figure 5.8 the three acoustic eigenmodes corresponding to the lowest eigenfrequencies are depicted. These derive from the solution of the homogeneous wave equation (Equation 3.18) and its appropriate boundary condition (Equation 4.15). The images show the absolute value of the acoustic pressure at the eigenfrequencies 33.1 kHz (left), 47.8 kHz (middle) and 48.1 kHz (right). The eigenfrequencies of the second and third mode are almost equal. The gravity, which bends the discharge arc upwards off the symmetry axis, prevents the formation of two degenerate modes. Under microgravity conditions, these modes would degenerate: a rotation of the third mode by 90° around the y-axis would equal the second mode. Particularly, the second mode visualises the non-rotationally symmetric temperature distribution inside the arc tube because the absolute pressure of the antinode at the top of the arc tube ($z = 3.0\,\mathrm{mm}$) is 40 % smaller than the pressure of the antinode at the bottom ($z = -3.0\,\mathrm{mm}$). Higher eigenfrequencies occur at 53.3 kHz, 64.2 kHz and 65.2 kHz. The latter two frequencies would degenerate under microgravity conditions as well.

The inhomogeneous wave equation (Equation 3.14) was solved to obtain the acoustic pressure amplitude as a function of the excitation frequency f_{ex}. The amplitudes in Figure 5.10 result that depend on their location inside the arc tube

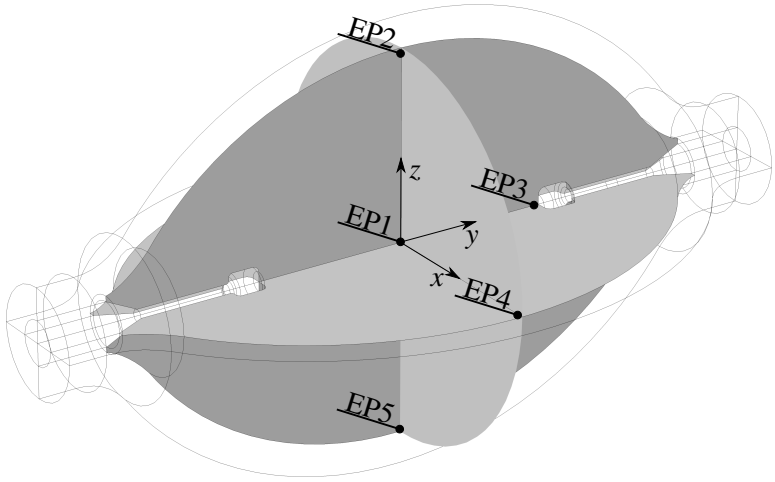

Figure 5.9. Location of five evaluation points inside the arc tube: Centre of the tube $\vec{r}_1 = (0,0,0)^T$ mm, top end of the tube $\vec{r}_2 = (0,0,2.9)^T$ mm, in the front of one electrode $\vec{r}_3 = (0,2.38,0)^T$ mm, in the front of the arc tube $\vec{r}_4 = (2.9,0,0)^T$ mm. The point at $\vec{r}_5 = (0,0,-2.9)^T$ mm will be used later on.

(Figure 5.9). These curves are also named *acoustic response functions*. For example, for the first eigenfrequency at $f_{\text{ex}} = 33.1\,\text{kHz}$ an amplitude peak appears at a point located in front of one of the electrodes ($\vec{r}_3$, green curve). The eigenmode in Figure 5.8 (left) already shows an acoustic pressure higher zero ($|p| > 0$) at this point. The other three curves in Figure 5.10, that correspond to the points $\vec{r}_1$ (dark blue curve), $\vec{r}_2$ (red curve) and $\vec{r}_4$ (light blue curve), do virtually not show amplitude peaks at $f_{\text{ex}} = 33.1\,\text{kHz}$ because these points are located at pressure nodes. Actually, no amplitude peaks in the amplitude response function appear at the eigenfrequencies 64.2 kHz and 65.2 kHz because the corresponding modes possess pressure nodes at all four points, where the pressure was evaluated (Figure 5.9). The profile of these frequency-dependent amplitudes are assumed to be of a Lorentzian shape (Equation 3.22).

The amplitudes $\mathscr{A}_j$, which represent the contribution of the j^{th}-mode to the response curve, are determined by the excitation and the damping. A prerequisite for a strong resonance is a large excitation amplitude

$$\mathscr{A}_j \propto \int_{V_c} p_j^* \mathscr{H} \mathrm{d}V. \tag{5.1}$$

that is proportional to the overlap integral of the power density of heat generation $\mathscr{H}(\vec{r})$ and the conjugate complex of the acoustic pressure mode $p_j^*(\vec{r})$. The power

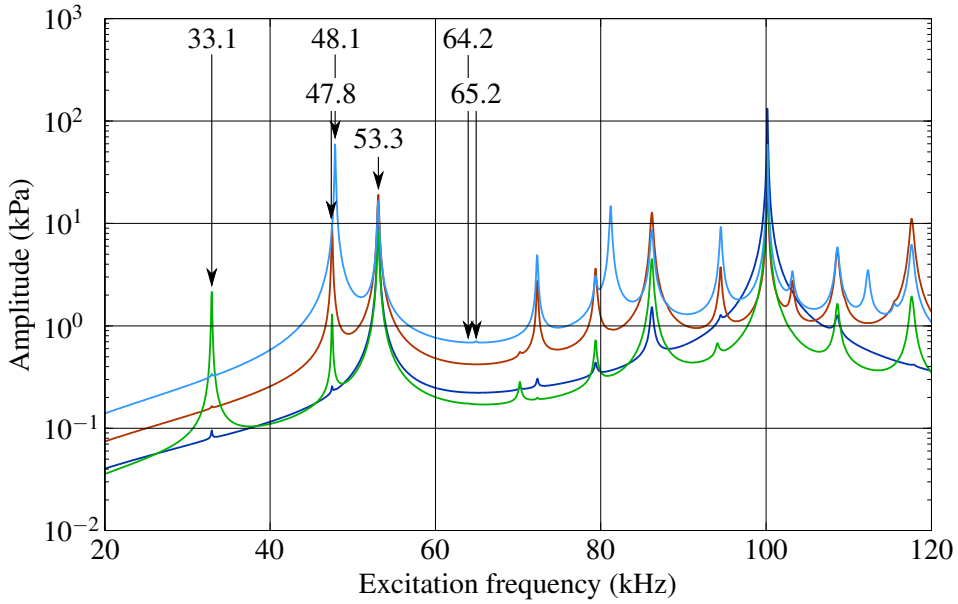

Figure 5.10. Calculated amplitude response function at four positions inside the arc tube (see Figure 5.9). Dark blue: $\vec{r}_1$, red: $\vec{r}_2$, green: $\vec{r}_3$, light blue: $\vec{r}_4$.

density represents the source term of the Elenbaas-Heller equation (Equation 3.5), which is the Joule heat less the emitted radiation. The power density is large inside a region with a temperature larger 4000 K and small in the remaining volume of the arc tube. Hence, the magnitude of the overlap integral strongly depends on the spatial distribution of the acoustic pressure that is obviously different for each eigenmode.

The pressure node of the first eigenmode (Figure 5.8, left) coincides with the x-z-plane. Consequently, the resulting overlap integral is small in this region despite a large power density. In the volume, where the acoustic pressure is high, the power density is low ($T < 4000\,\mathrm{K}$). Altogether, no strong excitation of the first eigenmode occurs. The situation for the second eigenmode is quite different because the positions of the power density and the pressure node do not coincide. This results in a significant overlap in the region between the electrodes (Equation 5.1). Hence, a high acoustic pressure is expected, which impacts the fluid flow. Therefore, detailed investigations of this mode are presented in Sections 5.4 and 5.5.

Figure 5.11 shows the total loss factors, which comprises viscous and heat conduction losses. The loss factor equations (Equations 3.25, 3.26, 3.29, 3.31) together with the Equations 3.23 and 3.24 for the layer thickness show that the

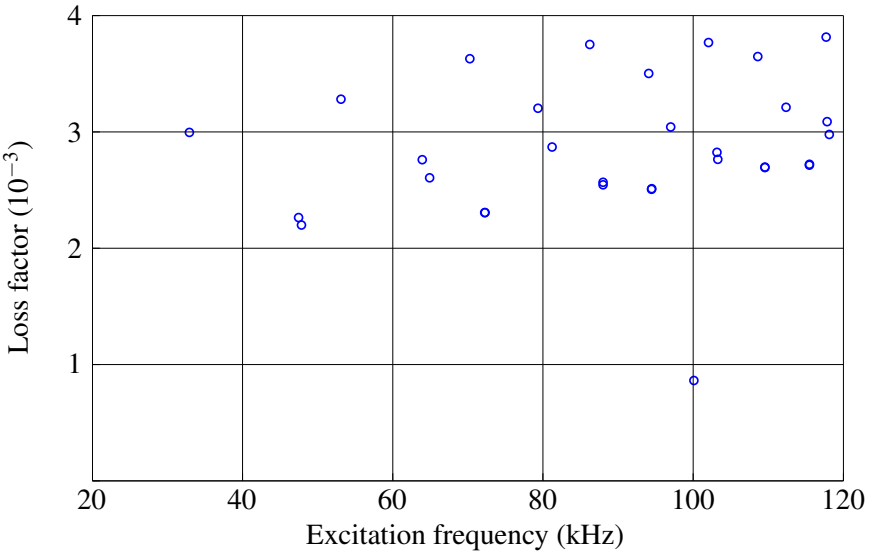

Figure 5.11. Total loss factor as a function of the excitation frequency.

damping rises with increasing viscosity and heat conductivity. Furthermore, the volume losses linearly increase with the excitation frequency. Hence, the sound absorption is large enough to dissipate the excitation energy and to avoid visible distortion of the discharge arc when the excitation frequency exceeds a specific value. Experimental investigations revealed that this frequency is approximately 500 kHz [32,46,65].

5.2.2 Experimental Investigations

In the experiment, arc flicker is detected by measurements of the voltage drop between the electrodes as described in Section 4.4 and schematically depicted in Figure 4.10. Generally, an AR is excited when the operating frequency of the power signal equals an acoustic eigenfrequency of the arc tube. Arc flicker is excited when a certain power threshold of the alternating part of the signal is exceeded. In this work, the power threshold is adjusted by the modulation depth of the voltage signal.

Figure 5.12 presents an overview of a wide frequency range of 20 kHz to 200 kHz, in which arc flicker in the investigated HID lamp occurs. The modulation depth in this experiment was varied from 0 % to 10 % in 1 %-steps. In the grey-coloured area, no arc flicker was detected and, hence, the lamp could stably be operated. The maximum modulation depth was not reached at some excita-

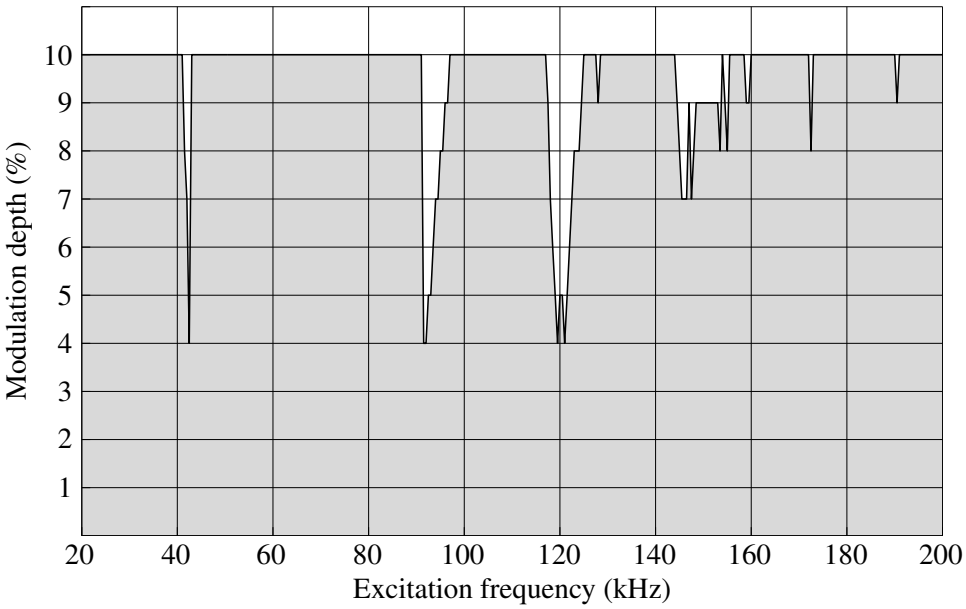

Figure 5.12. Experimental detection of acoustic instabilities over a wide frequency range. The data originate from lamp number 4.

tion frequencies because the voltage drop exceeds one or even both termination criteria. These consist of the voltage fluctuation $V_{\text{fluc}} \geq 1.5\,\text{V}$ measured at one operating point (specific excitation frequency f_{ex} and modulation depth α) and of a voltage limit of $V_{\text{lim}} \geq V_{\text{ref}} + 5.0\,\text{V}$ that exceeds the reference voltage measured at a modulation depth of 0 %. Thus, the termination prevents operation at higher modulation depths at this excitation frequency to prevent lamp failures that are caused by temperature fluctuations or exceedingly high temperatures inside the arc tube.

The results show that the lowest excitation frequency leading to arc flicker is approximately 42 kHz and occurs in a relatively narrow frequency band. Around 95 kHz and 120 kHz, wider frequency bands are affected by arc flicker. The wider range can result from excitations of more than one acoustic eigenmode. The simulation results (see Figure 5.10) have already shown that a lot of eigenfrequencies occur in this frequency range. Figure 5.12 also reveals that for some excitation frequencies a modulation depth of 4 % is sufficient to excite ARs and, consequently, terminate the measurement.

For a more detailed analysis, the AR at the lowest frequency, that shows arc flicker, was chosen in order to reduce the probability of measuring a superposition of acoustic eigenmodes. The frequency region of these detailed measurements ranges from 35 kHz to 50 kHz in 500 Hz-steps, and the modulation depth was in-

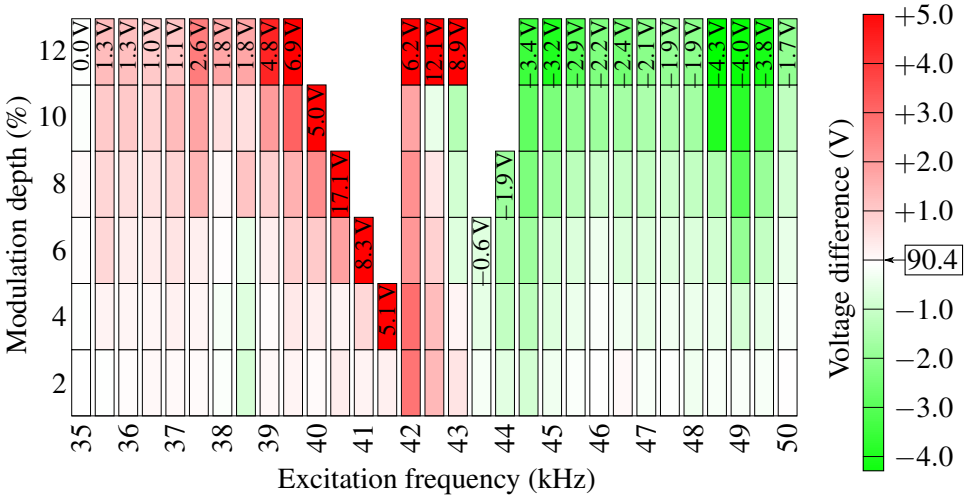

Figure 5.13. Measurement of the AR at the lowest excitation frequency, at which arc flicker occurred. The data originate from lamp number 4.

creased from 0 % to 12 % in 2 %-steps. Figure 5.13 shows the detection of the AR of a certain lamp (number 4). In addition to the threshold value of the modulation depth for each excitation frequency, the corresponding result of the measured voltage drop for each operating point is shown. In the scale, the reference voltage $V_{\mathrm{ref}} = 90.4\,\mathrm{V}$ is pointed out. Measured voltages that are higher than V_{ref} are marked in red and operating points with a lower voltage are coloured green. The scale of the excess voltage is limited to 5.0 V, which corresponds to V_{lim}. Additionally, the measured voltage at the last operating point for each excitation frequency is presented. A higher voltage is the result of an increasing arc length so that the arc deflection increases as well [38]. In contrast to that, the green colour indicates operating points with a decreasing arc deflection (arc straightening). The intensity of the colour represents the strength of the voltage difference to V_{ref} and, consequently, the strength of the deflection change. This was observed by eye and proved by measurements with the camera. For example, Figure 5.13 shows at $f_{\mathrm{ex}} = 36.0\,\mathrm{kHz}$ and $\alpha = 8\,\%$ a pale red colour, which indicates a 0.7 V higher voltage than the reference voltage: $V_{\mathrm{ref}} + 0.7\,\mathrm{V} = 91.1\,\mathrm{V}$.

The information, which termination criterion was reached in the experiment, can also be extracted from Figure 5.13. When the operating point is marked in a shade of red and a voltage difference below 5.0 V is given, V_{lim} was reached (e.g. $f_{\mathrm{ex}} = 39.5\,\mathrm{kHz}$, $\alpha = 12\,\%$ or $f_{\mathrm{ex}} = 41.5\,\mathrm{kHz}$, $\alpha = 4\,\%$). When the operating point is marked in bright red or even green and a value less than 5.0 V is presented, V_{fluc}

prevented operation at higher modulation depths (e.g. $f_{ex} = 43.5\,\text{kHz}$, $\alpha = 6\,\%$ or $f_{ex} = 44.0\,\text{kHz}$, $\alpha = 8\,\%$).

In general, two different discharge arc behaviours can be observed in Figure 5.13 that are caused by different mechanisms. Up to $f_{ex} = 42.5\,\text{kHz}$, the voltage increases when increasing the modulation depth. At higher excitation frequencies, the voltage decreases. The strength of the voltage difference to V_{ref} rises with increasing modulation depth because the share of the excitation part in relation to the stable part grows. The two local minima in the modulation depth are related to two different modes. The results of lamp number 4 highlight that the first minimum occurs at $f_{ex} = 41.5\,\text{kHz}$ and the second minimum at $f_{ex} = 43.5\,\text{kHz}$. The voltage exceeds V_{lim} at $f_{ex} = 41.5\,\text{kHz}$, whereas a fluctuating voltage V_{fluc} of a slightly straightened arc was detected at $f_{ex} = 43.5\,\text{kHz}$. At the three measured frequencies between these two minima, the experiment terminated at $\alpha = 12\,\%$. The measured voltage at $\alpha = 2\,\%$ and $f_{ex} = 42.0\,\text{kHz}$ is conspicuous because it is considerably higher than voltages at the same modulation depth at other excitation frequencies. The reason for this behaviour will be explained by the results of the recursion loop simulations, which are presented in Section 5.5.

The described measurements were performed for twelve lamps. The measurements serve to identify the mean values as well as the standard deviations of the reachable modulation depths and the frequencies, at which the lowest modulation depth is attained. Qualitatively, the results coincide with those presented beforehand; especially the results shown in Figure 5.13. Up to excitation frequencies, at which the lowest modulation depth occurs (e.g. $f_{ex} = 42.0\,\text{kHz}$ at lamp number 4), the voltage increases with modulation depth. At higher excitation frequencies, arc straightening, i.e. a decreasing voltage with increasing modulation depth, was detected. Quantitatively, the results differ from lamp to lamp of the same kind because geometry and gas composition tolerances occur in the manufacturing process. During the measurements, one of the lamps exploded at $f_{ex} = 40.5\,\text{kHz}$ and $\alpha = 12\,\%$ so that its measurement results were excluded in the following calculations.

Figure 5.14 presents the averaged results. The minimal modulation depth, that terminates the experiment, is $3.8\,\%$ and occurs at $f_{ex} = 41.5\,\text{kHz}$. Moreover, at $f_{ex} = 43.5\,\text{kHz}$ a second local minimum is visible, at which a mean modulation depth of $7.6\,\%$ is necessary for the excitation. The lines indicating the standard deviation unveil considerable differences from lamp to lamp in the modulation depth that is required to excite AR in the arc tube. For example, at $f_{ex} = 41.5\,\text{kHz}$ the

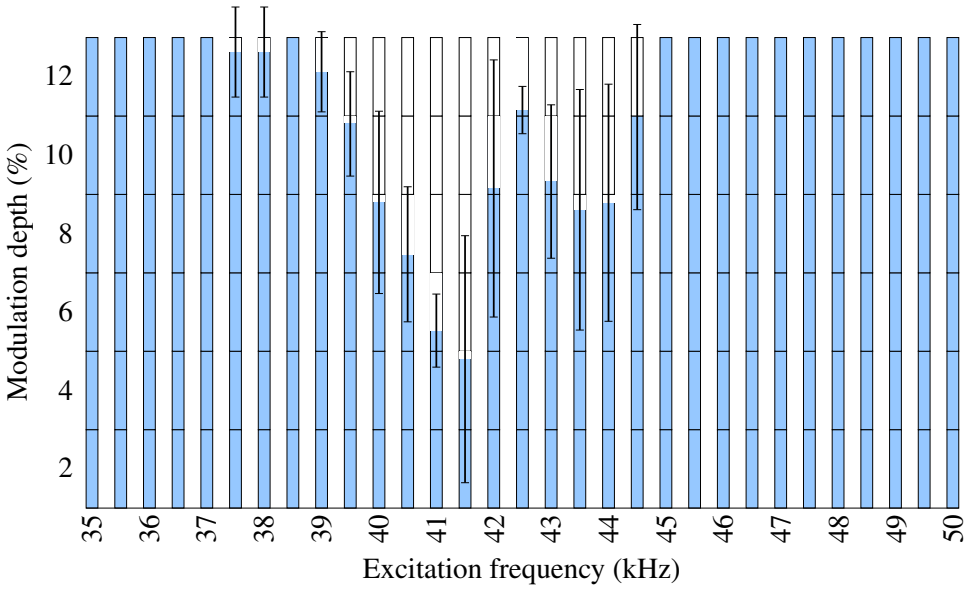

Figure 5.14. Determination of ARs at different excitation frequencies and modulation depths. The blue bars represent the mean values of eleven lamps, and the black lines mark the standard deviations of these lamps.

standard deviation of the modulation depth is 3.2 % and, therefore, nearly equals the mean value. Contrarily, the frequency, at which the least modulation depth is required for the excitation, only ranges from 40.0 kHz to 42.0 kHz. Therefore, the experimental AR frequency is (41.4 ± 0.4) kHz.

In addition to the experimental investigation of different lamps, one lamp was tested ten times in the frequency range of 36.0 kHz to 46.0 kHz in 500 Hz-steps and at modulation depths of 0 % to 12 % in 1 %-steps. The mean values and standard deviations are depicted in Figure 5.15. Compared to the measurement results of eleven lamps, the standard deviation of the modulation depth is significantly lower, e.g. $\alpha = (3.1 \pm 0.6)\,\%$ at $f_{\mathrm{ex}} = 41.5\,\mathrm{kHz}$. The result of the AR frequency is (41.6 ± 0.2) kHz. Therefore, the high standard deviations are due to the lamp differences and are not caused by the measurement system.

Experiments in the frequency range of 62.0 kHz to 68.0 kHz with the same measurement procedure were conducted because the simulation shows two eigenmodes at 64.2 kHz and 65.2 kHz. Since a modulation depth of 10 % (Figure 5.12) is not sufficient to induce light flicker, the modulation depth was increased in 2 %-steps up to 16 %. The results of the six tested lamps summarises Figure 5.16. The modulation depth, which is required to reach the termination criteria, has a minimal

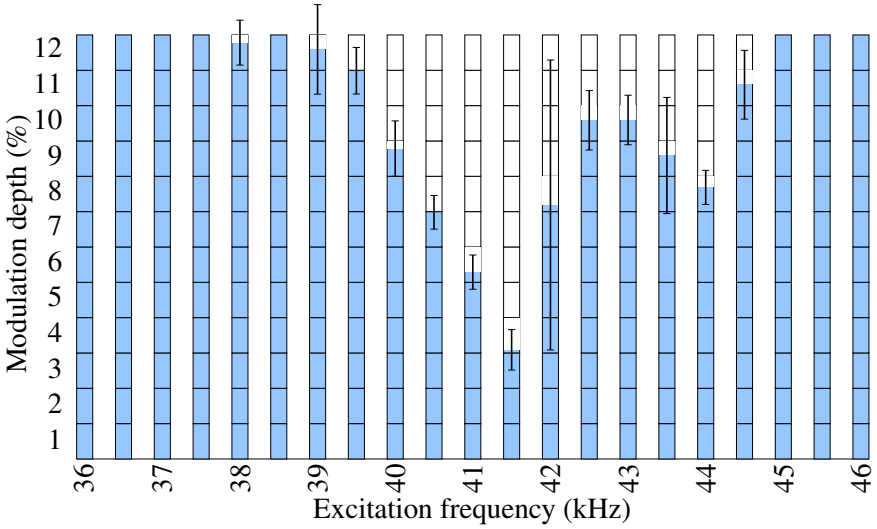

Figure 5.15. Determination of the AR frequency at different excitation frequencies and modulation depths of lamp sample 1. The blue bars show the mean value and the black bars the standard deviation of ten measurements.

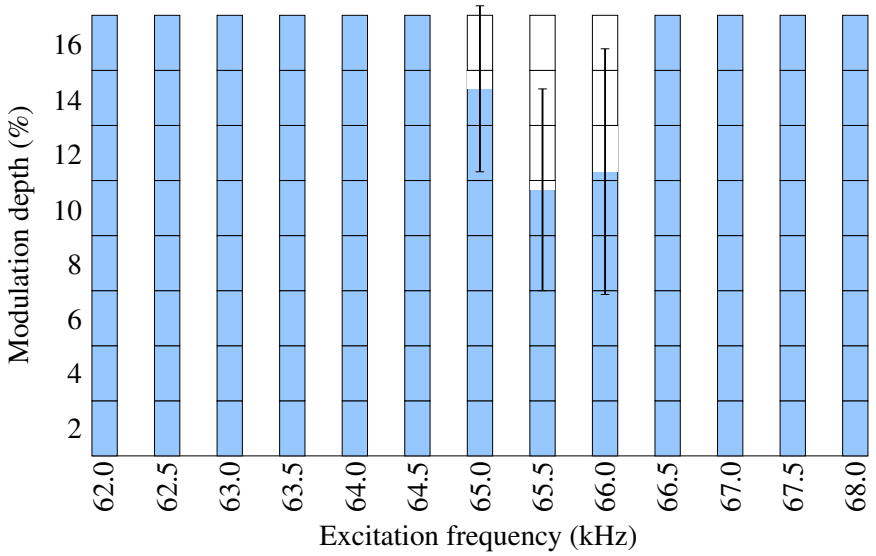

Figure 5.16. Determination of the AR around 65 kHz. The blue bars represent the mean values of six lamps, and the black lines mark the standard deviations of these lamps.

value of (9.7 ± 3.7) % at an excitation frequency of 65.5 kHz and (10.3 ± 4.5) % at $f_{ex} = 66.0$ kHz. The frequency, at which the least modulation depth is required for the excitation, is (65.8 ± 0.2) kHz. Furthermore, the measured results reveal that the measurements always terminated because of a fluctuating voltage V_{fluc}. In contrast to the measurement results around 41 kHz (Figure 5.13), no significant voltage increase was detected. Moreover, the voltage fluctuations and, therefore, the arc movements were comparably small. A similar behaviour of the discharge arc for all six lamps was detected at frequencies above the resonance frequency; the excitation leads to a decreasing voltage with increasing modulation depth, i.e. arc straightening.

5.2.3 Comparison and Discussion

The excitation frequencies, at which the discharge arc flickers, are experimentally determined by measurements of the voltage drop between the electrodes. In the simulation, the results of the eigenmode analysis show the acoustic pressure distribution and the corresponding eigenfrequencies.

The simulation computes the first acoustic eigenfrequency at 33.1 kHz. As has been described in Section 5.2.1, the resulting excitation amplitude of this mode is weak and, hence, no acoustic instabilities are expected. This corresponds to experimental observations because no significant deviation from the voltage at stable operating conditions was detected in this frequency region.

The second eigenfrequency occurs at 47.8 kHz and corresponds to the experimentally determined resonance frequency at 41.4 kHz. The simulated frequency is therefore 6.4 kHz or 15.5 % higher. Since the material parameters (mass density and speed of sound) of the homogeneous wave equation (Equation 3.18) are temperature-dependent, an incorrect temperature field deteriorates the resulting eigenfrequencies. The main reason for the temperature deviation of the simulation to experimental findings were already discussed in Section 5.1.3: A simplified model of the electrodes and inaccurate transport coefficients that are further analysed in Section 5.3. The extended model, that includes the recursion loop, computes a smaller difference between the experiment and the simulation. The resonance frequency of the second eigenmode reduces to 46.3 kHz so that the difference to the experiment diminishes to 11.8 %. The reason for the altered eigenfrequency of the extended model are presented in Section 5.5.

The correspondence of the third eigenmode at 48.1 kHz and its experimental equivalent at 43.5 kHz were not further investigated. Light flicker was also mea-

sured at an excitation frequency of 65.8 kHz. In the simulation, two eigenmodes at 64.2 kHz and 65.2 kHz were detected that differ maximal 2.5 % from the experimental value.

In contrast to the straightforward comparison of the frequencies, a comparability of the pressure amplitude of the simulation and the voltage changes in the experiments is inappropriate. The impact of the acoustically induced flow on the voltage drop is treated in Section 5.5, in which the recursion loop is incorporated. There, the simulated voltage is compared to the measured voltage.

With regard to the amplitude (modulation depth), the experimental results show an increasing loss with an increasing excitation frequency because the modulation depth necessary to excite flicker increases. Figure 5.12 reveals that up to 120 kHz a modulation depth of 4 % is sufficient to excite flicker, but a higher modulation depth is necessary at frequencies beyond 120 kHz. The simulation results in Figure 5.11 also show the trend of an increasing loss factor when raising the excitation frequency. However, the increase is weak, which might be explained by loss mechanisms not considered in the simulation due to geometrical simplifications and no sharp edges [71].

5.3 Sensitivity Analysis

Geometrical deviations and gas composition tolerances in the manufacturing process influence the physical properties considered in this work. Additionally, ageing effects can alter discharge arc properties. The sensitivity analysis serves to identify the impact of different transport coefficients and main geometries on characteristic arc tube properties. Furthermore, the investigation enables detection of parameters that enlarge the frequency region, in which the excitation of ARs is prevented. As characteristic properties, the maximal temperature inside the arc tube $T_{\max}$, the voltage drop between the electrodes V_{drop}, the maximal velocity $u_{\max}$ and the frequency of the second eigenmode $f_{2\text{nd}}$ were chosen.

In case of the transport properties, the absolute pressure, the dynamic viscosity, the electric conductivity, the radiation loss and the thermal conductivity of the arc tube filling were varied. The nominal values can be found in Section 4.2 and especially in Figure 4.3. The curves as well as the absolute pressure of 2.8 MPa were multiplied with 0.8, 0.9, 1.1 and 1.2. The results of the investigations are shown in Table 5.1.

When the absolute pressure inside the arc tube is higher than the reference pres-

Table 5.1. Influence of material functions on important arc tube characteristics. V_{drop} is the voltage drop between the electrodes, $T_{\max}$ the maximal temperature inside the arc tube, $u_{\max}$ the maximal velocity and $f_{2\mathrm{nd}}$ the frequency of the second eigenmode. The values in parentheses are the relative differences to the nominal value at 100 %.

		80 %	90 %	100 %	110 %	120 %
Absolute pressure	V_{drop} (V)	80.5 (−2.9 %)	81.6 (−1.5 %)	82.8	83.9 (+1.3 %)	85.1 (+2.7 %)
	$T_{\max}$ (K)	4829 (+0.2 %)	4822 (+0.1 %)	4818	4818 (0.0 %)	4817 (0.0 %)
	$u_{\max}$ (mm s^{-1})	80.0 (−6.4 %)	83.5 (−1.9 %)	85.1	85.5 (+0.5 %)	86.1 (+1.2 %)
	$f_{2\mathrm{nd}}$ (kHz)	48.4 (+1.2 %)	48.1 (+0.6 %)	47.8	47.5 (−0.6 %)	47.2 (−1.3 %)
Radiation loss	V_{drop} (V)	80.1 (−3.4 %)	81.5 (−1.6 %)	82.8	83.8 (+1.2 %)	84.7 (+2.2 %)
	$T_{\max}$ (K)	4947 (+2.6 %)	4872 (+1.1 %)	4818	4798 (−0.4 %)	4782 (−0.8 %)
	$u_{\max}$ (mm s^{-1})	86.9 (+2.1 %)	85.7 (+0.7 %)	85.1	84.4 (−0.8 %)	84.0 (−1.3 %)
	$f_{2\mathrm{nd}}$ (kHz)	47.4 (−0.8 %)	47.6 (−0.4 %)	47.8	47.8 (0.0 %)	47.9 (+0.2 %)
Electric conductivity	V_{drop} (V)	92.5 (+10.5 %)	87.3 (+5.2 %)	82.8	78.9 (−4.9 %)	75.6 (−9.5 %)
	$T_{\max}$ (K)	4818 (0.0 %)	4818 (0.0 %)	4818	4818 (0.0 %)	4818 (0.0 %)
	$u_{\max}$ (mm s^{-1})	85.1 (0.0 %)	85.1 (0.0 %)	85.1	85.1 (0.0 %)	85.1 (0.0 %)
	$f_{2\mathrm{nd}}$ (kHz)	47.8 (0.0 %)	47.8 (0.0 %)	47.8	47.8 (0.0 %)	47.8 (0.0 %)
Dynamic viscosity	V_{drop} (V)	84.0 (+1.4 %)	83.4 (+0.7 %)	82.8	82.2 (−0.7 %)	81.8 (−1.2 %)
	$T_{\max}$ (K)	4818 (0.0 %)	4818 (0.0 %)	4818	4819 (0.0 %)	4821 (+0.1 %)
	$u_{\max}$ (mm s^{-1})	94.0 (+9.5 %)	88.9 (+4.3 %)	85.1	81.2 (−4.8 %)	77.7 (−9.5 %)
	$f_{2\mathrm{nd}}$ (kHz)	47.4 (−0.8 %)	47.6 (−0.4 %)	47.8	47.9 (+0.2 %)	48.0 (+0.4 %)
Thermal conductivity	V_{drop} (V)	80.4 (−3.0 %)	81.6 (−1.5 %)	82.8	83.8 (+1.2 %)	84.7 (+2.2 %)
	$T_{\max}$ (K)	4977 (+3.2 %)	4888 (+1.4 %)	4818	4800 (−0.4 %)	4785 (−0.7 %)
	$u_{\max}$ (mm s^{-1})	79.2 (−7.4 %)	82.3 (−3.4 %)	85.1	87.4 (+2.6 %)	89.5 (+4.9 %)
	$f_{2\mathrm{nd}}$ (kHz)	48.1 (+0.6 %)	47.9 (+0.2 %)	47.8	47.6 (−0.4 %)	47.5 (−0.6 %)

sure, the mass density increases according to Equation 3.9. This leads to a higher gravitational force so that the maximal velocity increases. This is confirmed by the data in Table 5.1 and by experimental results of a high-pressure sodium lamp [186]. The higher velocity in turn increases the arc deflection, which results in an increased voltage drop between the electrodes and a decreasing second eigenfrequency at increasing pressure. In contrast to the altered temperature field that is characterised by the higher arc deflection, the maximal temperature of the hot plasma spots remains unchanged.

An increasing radiation loss in the arc tube leads to a lower peak temperature because more heat is radiated particularly from the hot spots. Furthermore, an increasing radiation loss results in a temperature field with smaller gradients in the whole arc tube leading to a slightly decreased maximal velocity. However, the voltage drop increases.

The electric potential drop is mainly determined by the electric conductivity of the arc tube content. A 20 % decrease of the electric conductivity increases the potential drop by almost 10 V. The voltage increases because a lower electric current can be transported through the plasma and, therefore, a higher voltage is necessary to keep the electric power constant. Surprisingly, $T_{\max}$, $u_{\max}$ and $f_{2\mathrm{nd}}$ are not changed at all by an altered electric conductivity. Hence, the temperature field and the heat source (Equation 3.16) remain constant when varying the electric conductivity. The reason is that the input power (35 W) is kept constant so that an increasing electric conductivity is compensated by a decreasing electric field (see Equation 3.2).

The impact of the dynamic viscosity is mainly restricted to the fluid velocity because this material parameter is necessary to solve the Navier-Stokes equation (Equation 3.6). Furthermore, it is important for the calculation of the acoustic loss due to shear stress (Equations 3.26 and 3.29). An increased velocity raises the arc deflection and, hence, results in a higher voltage drop. The influence on the maximal plasma temperature is negligibly small.

When the thermal conductivity is lower than its reference value, a higher maximal temperature occurs, which seems plausible. The higher temperature leads to a lower mass density because the absolute pressure is kept constant (Equation 3.9). Consequently, the buoyancy decreases, the arc straightens and a lower voltage is required to transport the electric current. The trend of the second eigenfrequency is always determined by the maximal fluid velocity: An increasing $u_{\max}$ decreases $f_{2\mathrm{nd}}$ and vice versa. Hence, the increasing maximal fluid velocity when increasing

the thermal conductivity leads to a decreasing second eigenfrequency.

Altogether, the impact of the altered material properties is limited. Despite a variation of up to 20 % referred to the reference value, the investigated parameters only change slightly. Particularly, the considered acoustic eigenfrequency remains approximately constant. The voltage drop is influenced by the electric conductivity and the maximal temperature by the radiation loss and the thermal conductivity.

Next to the impact of the materials, the sensitivity of the geometry on important arc tube properties was investigated. The complete model was shrunk and enlarged by ± 10 % and ± 5 %, respectively, the model was tilted by 5° and 10°, the electrode distance was varied from 4.32 mm in 0.24 mm-steps to 5.28 mm, and different inner diameter of the arc tube from 4.0 mm up to 6.0 mm were tested. The results are summarised in Table 5.2 except for the ones of the tilted model because its influence on the voltage drop, the maximal temperature, the maximal velocity and the second eigenfrequency even at 10° is insignificant.

The lamp size has major impacts on the physical fields of the arc tube filling. When increasing the lamp size, the voltage drop between the electrodes increases due to the enlarged electrode distance. Furthermore, the increasing maximal velocity leads to a higher arc deflection, which is experimentally confirmed by measurements of high-pressure sodium lamps with different sizes [186]. Remarkably, but expectable, is the shift of the second eigenfrequency when changing the lamp size; from a 10 % shrunk to a 10 % enlarged model, the frequency drops 11.2 kHz.

The nominal diameter of the inner arc tube wall is 5.0 mm. Changes of this geometrical dimension do not significantly alter the voltage drop and the maximal temperature because these values are mainly determined by the geometry of the electrodes and their gap. Contrarily, the maximal velocity increases with increasing tube radius, and the frequency of the second eigenmode simultaneously decreases.

A modification of the electrode distance results in a considerable variation of the discharge arc. As has already been detected in the investigation of the lamp size, a higher electrode distance increases the voltage drop and concurrently induces a lower peak temperature of the hot plasma spots. Moreover, an enlarged electrode gap leads to a lower velocity. As has already been derived from Table 5.1, a lower velocity is always connected to a higher second eigenfrequency. This can be confirmed by the data in Table 5.2.

More detailed investigations of the electrode simulate an HID lamp with different electrode shapes [101]. These describe the influence of the geometry on the temperature of the hot plasma spots and the electrodes as well as the electrode

Table 5.2. Influence of geometry on important arc tube characteristics. V_{drop} is the voltage drop between the electrodes, $T_{\max}$ the maximal temperature inside the arc tube, $u_{\max}$ the maximal velocity and $f_{2\mathrm{nd}}$ the frequency of the second eigenmode. The values in parentheses are the relative differences to the nominal value (100 % for the lamp size, 5.0 mm for the inner tube diameter and 4.80 mm for the electrode distance).

Lamp size	90 %	95 %	100 %	105 %	110 %
V_{drop} (V)	76.8 (−7.8 %)	80.2 (−3.2 %)	82.8	84.6 (+2.1 %)	86.5 (+4.3 %)
$T_{\max}$ (K)	5074 (+5.0 %)	4923 (+2.1 %)	4818	4756 (−1.3 %)	4674 (−3.1 %)
$u_{\max}$ (mm s^{-1})	79.9 (−6.5 %)	82.7 (−2.9 %)	85.1	86.8 (+2.0 %)	89.3 (+4.7 %)
$f_{2\mathrm{nd}}$ (kHz)	53.9 (+11.3 %)	50.7 (+5.7 %)	47.8	45.1 (−6.0 %)	42.7 (−11.9 %)
Inner tube diameter (mm)	4.0	4.5	5.0	5.5	6.0
V_{drop} (V)	83.2 (+0.5 %)	83.0 (+0.2 %)	82.8	82.8 (0.0 %)	82.5 (−0.4 %)
$T_{\max}$ (K)	4824 (+0.1 %)	4817 (0.0 %)	4818	4818 (0.0 %)	4818 (0.0 %)
$u_{\max}$ (mm s^{-1})	82.3 (−3.4 %)	83.7 (−1.7 %)	85.1	86.3 (+1.4 %)	87.3 (+2.5 %)
$f_{2\mathrm{nd}}$ (kHz)	48.3 (+1.0 %)	47.9 (+0.2 %)	47.8	47.2 (−1.3 %)	46.8 (−2.1 %)
Electrode distance (mm)	4.32	4.56	4.80	5.04	5.28
V_{drop} (V)	75.4 (−9.8 %)	79.6 (−4.0 %)	82.8	85.8 (+3.5 %)	89.8 (+7.9 %)
$T_{\max}$ (K)	5007 (+3.8 %)	4898 (+1.6 %)	4818	4783 (−0.7 %)	4723 (−2.0 %)
$u_{\max}$ (mm s^{-1})	95.1 (+10.5 %)	89.7 (+5.1 %)	85.1	80.6 (−5.6 %)	76.8 (−10.8 %)
$f_{2\mathrm{nd}}$ (kHz)	47.1 (−1.5 %)	47.4 (−0.8 %)	47.8	48.0 (+0.4 %)	48.2 (+0.8 %)

sheath voltages that were detected in the investigated HID lamp as well. Similar simulations with different electrode shapes were carried out previously, but these focus on the AR frequencies [58].

5.4 Flow Field at Instable Operating Conditions

The implementation of the acoustic streaming effect results in an additional body force that affects the velocity field inside the arc tube. This influence is investigated, and the results are linked to the arc flicker phenomenon. The feedback of AS on the temperature and further fields is not included at this stage. Hence, the resulting flow field is of hypothetical nature only, but it can already indicate the significance of the additional force. To obtain the correct stationary fields, the calculations were repeated recursively in the next step (Section 5.5).

5.4.1 Simulations at Different Acoustic Eigenmodes

The amplitude response function resulting from the inhomogeneous wave equation enables to determine the acoustic pressure amplitude at each excitation frequency for any point inside the arc tube. Additionally, the spatial pressure distribution in the vicinity of the eigenfrequencies practically equals the acoustic eigenmodes, but only when the modes are well separated from one another. The acoustic particle velocities in the x-, y- and z-direction can be calculated with the acoustic pressure distribution. These serve to calculate the AS force (Equation 3.32). Both forces, the AS and the gravitational force, drive the fluid in the following laminar flow simulation. The calculation procedure is described in Section 4.3.2.

The first acoustic eigenmode at 33.1 kHz is depicted in the left part of Figure 5.8. As has already been explained, the overlap integral of the acoustic pressure of this first mode and the power density results in a small excitation amplitude (Equation 3.21). The magnitude of the AS force is only a four-hundredth of the gravitational force in the centre of the arc tube. The velocity field in Figure 5.17 confirms that the AS force of the first mode is negligibly small because no significant changes compared to the purely buoyancy-driven flow in Figure 5.3 are discernible. The maximal velocity of 86 mm s^{-1} is just 1.4 % higher than the maximal velocity of the purely buoyancy-driven flow.

The investigations concerning the second eigenmode correspond to the lowest resonance that was excited in experiments. In contrast to the first eigenmode, a

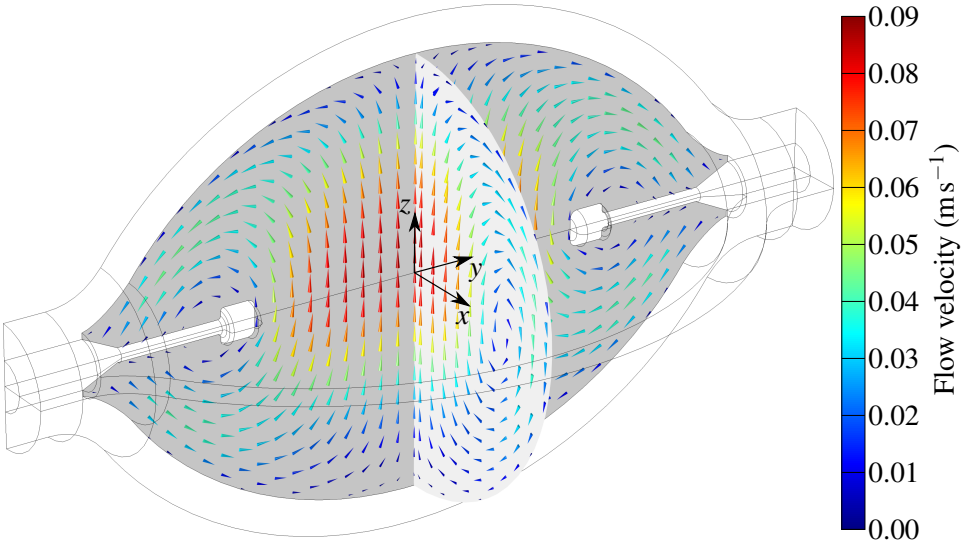

Figure 5.17. Flow pattern inside the arc tube driven by the gravitational and the AS force of the first eigenmode.

significant overlap of the pressure antinode and the power density exists. The resulting 3D AS force is symmetric to the vertical x-y-plane because the investigated eigenmode is symmetric to this plane as well. The magnitude of the AS force in the centre of the arc tube is more than 30 times higher than the gravitational force. Thus, the velocity field significantly changes when the AS effect is implemented.

Figure 5.18 as well as Figure 5.19 show the velocity field that ensues when a superposition of the buoyancy and the AS force of the second eigenmode drive the fluid. The flow patterns reveal a severe impact of the AS effect on the flow field. The maximal velocity is approximately $0.62\,\mathrm{m\,s^{-1}}$, which is seven times the buoyancy-driven flow ($0.085\,\mathrm{m\,s^{-1}}$). A 2D time-dependent simulation of an infinitely long arc tube with a diameter of 6 mm computes a maximal velocity of $1.0\,\mathrm{m\,s^{-1}}$ [57]. Here, the input power of 175 W oscillates by 30 % at the second azimuthal mode at 31.8 kHz. The maximal buoyancy velocities in both models are of similar order of magnitude; in the 2D simulation it is $80\,\mathrm{mm\,s^{-1}}$ and the simulation results obtained with the 3D stationary model show a velocity of $85\,\mathrm{mm\,s^{-1}}$. Since the tube geometry, the operating procedure, the material parameters and other properties differ in the two simulations, the similar resulting velocity values show a very satisfying accordance.

Beside an increasing velocity compared to the buoyancy-driven flow, the flow pattern changes essentially. The y-z-plane in Figure 5.19 shows four vortices. Two

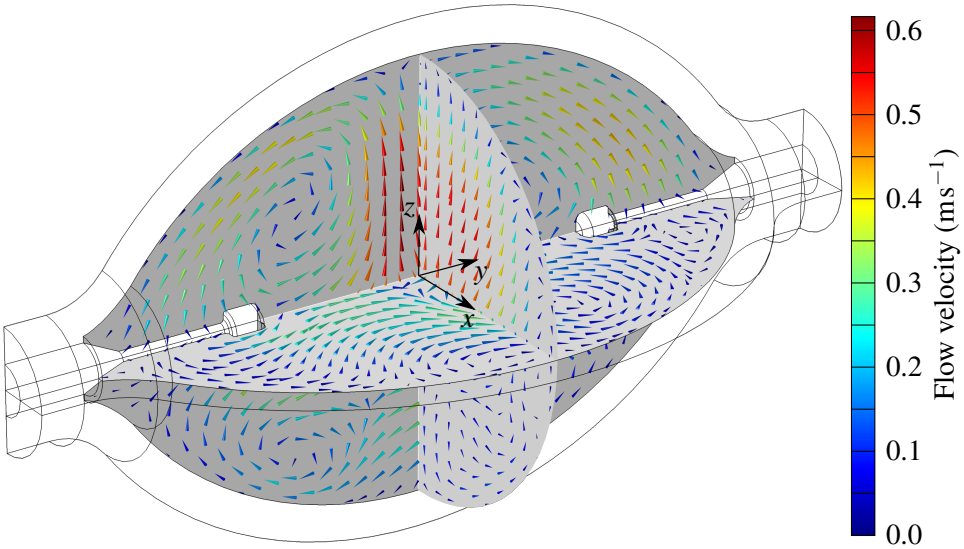

Figure 5.18. Flow pattern inside the arc tube driven by the gravitational and the AS force of the second eigenmode.

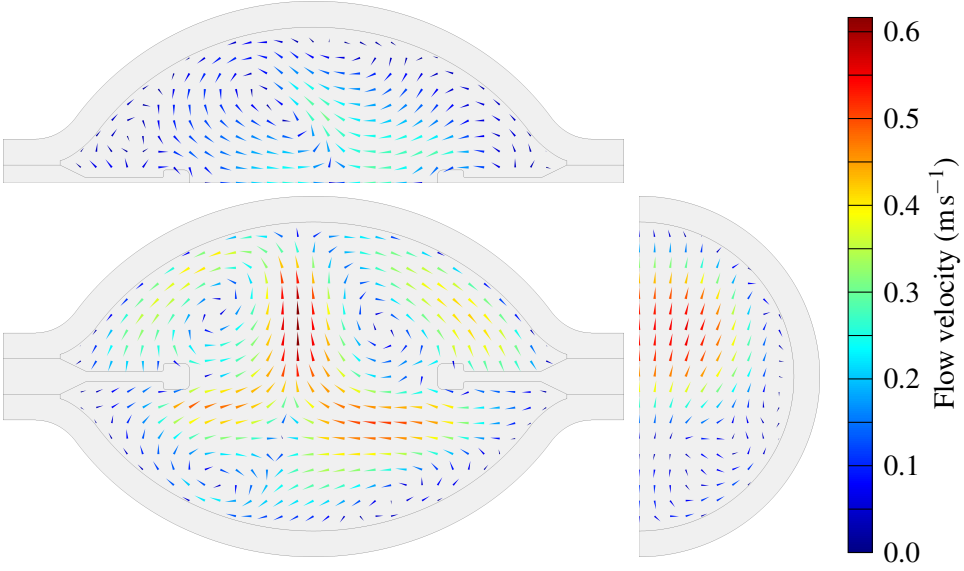

Figure 5.19. Flow pattern in three orthogonal planes through the arc tube's centre (top: x-y-plane; bottom left: y-z-plane; bottom right: x-z-plane) driven by the gravitational and the AS force of the second eigenmode.

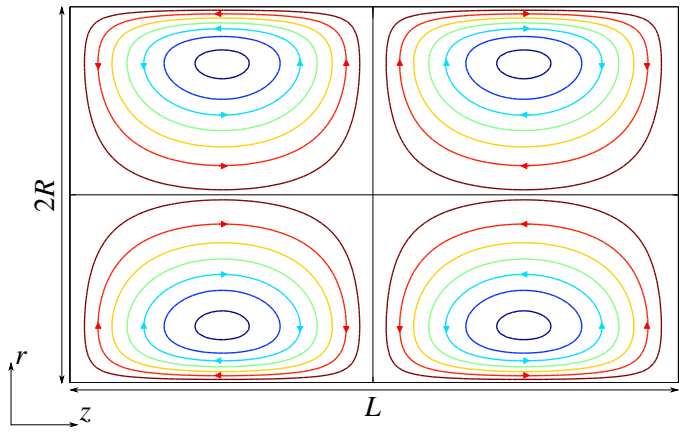

Figure 5.20. AS velocity field in a Kundt's tube [133,187]. r and z denote cylinder coordinates in arbitrary units.

of these are located in the lower part of the arc tube and two in the upper part. The top right vortex and bottom left vortex rotate clockwise, whereas the top left and the bottom right rotate counter-clockwise. In Figure 5.20 an AS flow pattern in a closed cylindrical tube (Kundt's tube) is schematically depicted. The flow is induced when the cylinder length corresponds to half a wavelength and a longitudinal mode is excited [133]. The vortices are caused by Rayleigh streaming [187] (see Section 3.2.2). The flow requires a pressure amplitude that exceeds a critical value so that the AS force is higher than the viscous force of the fluid [133]. Once the critical value is reached, the fluid elements start moving and form the four vortices.

The comparison to the pattern in the y-z-plane of Figure 5.19 reveals that both flow fields are qualitatively equivalent, although both systems differ in three important aspects. (1) the geometry of the Kundt's tube and the arc tube differ. (2) the temperature inside the Kundt's tube is constant so that no buoyancy-driven flow arises. (3) the pressure distribution of the acoustic mode in the Kundt's tube varies from the one in the arc tube of the HID lamp. Despite these differences, a similar flow pattern appears, which indicates that the simulation model is suitable for the calculation of the AS effect.

5.4.2 Symmetry Breaking and Critical Behaviour

The AS flow in the arc tube shows an interesting behaviour: The velocity field mainly driven by the AS force is not mirror-symmetric to the x-z-plane, although the model geometry and the boundary conditions are defined symmetrically. This symmetry breaking can occur in nonlinear dynamical systems [138]. The entropy

in these systems decreases locally because it is transferred to adjacent areas. Two examples, the Taylor-Couette flow and the Rayleigh-Bénard convection, have already been described in Section 3.3.

When the lamp is driven in outer space, the situation of the acoustically excited arc tube is similar to the one of the Kundt's tube. At stable operating conditions, the fluid elements are not transported by buoyancy because no gravitational force is present. Hence, the fluid velocity inside the arc tube is zero, i.e. the fluid is at rest. The operation near or at an eigenfrequency induces an AS force. When the force is beneath the critical value, it is compensated by the viscous force. When the AS force prevails the viscous force, a specific flow pattern arises. This pattern depends on the acoustic mode that is excited at the driving frequency. Differences to the flow in the Kundt's tube are limited to the arc tube geometry and the non-uniform temperature distribution.

In order to test if the situation in the arc tube of the HID lamp is similar to the one of the Taylor-Couette flow or the Rayleigh-Bénard convection, a control parameter S was introduced that gradually increased the amplitude of the AS force (see Equation 4.16). $\Delta S = 0.05$ was chosen as step size. The value $S = 0$ corresponds to a purely buoyancy-driven flow, which is depicted in Figure 5.3. The flow pattern at $S = 1$ is presented in Figures 5.18 and 5.19. Here, the buoyancy and the AS force drive the fluid.

The AS force of the second eigenmode and the spatial distribution of the acoustic pressure itself (see Figure 5.8 middle) are symmetric to the vertical x-z-plane that is located in the centre between the electrode. The force magnifies the upward-directed fluid movement in the middle upper part of the arc tube, whereas it counteracts the upward-directed flow in the middle lower part of the arc tube. Consequently, an increase of the control parameter S leads to an increase of the upward-directed velocity in the upper part as well as a decrease and reversal of the upward-directed velocity in the lower part. The reversal of the flow direction can be quantified by an order parameter

$$\Psi := \min_{z \in \mathscr{D}} u_z(0,0,z) \tag{5.2}$$

that determines the minimal velocity of u_z on the z-axis inside the arc tube ($\mathscr{D}$). Once S is high enough, the order parameter Ψ becomes negative and two additional vortices are formed in the bottom half.

Figure 5.21 shows the order parameter Ψ as a function of the control parameter

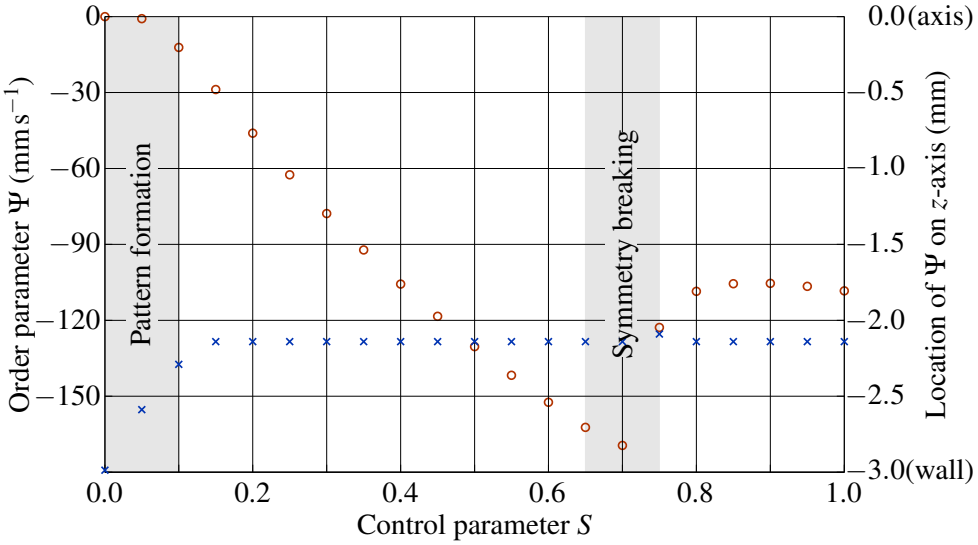

Figure 5.21. Order parameter Ψ as a function of the control parameter S (red circles). The corresponding axis is located on the left. Additionally, the z-position of the minimal value of u_z is displayed (blue crosses) with its corresponding axis on the right. The symmetry axis of the arc tube is located at $z = 0.0\,\mathrm{mm}$ and the arc tube wall at $z = -3.0\,\mathrm{mm}$.

(red circles). Additionally, the z-coordinate, where the minimum of u_z is located, is presented (blue crosses). The *pattern formation* region highlights the control parameter required for the formation of additional vortices. In the region labelled *symmetry breaking*, a transition from a mirror-symmetric to an asymmetrical state occurs. The velocity u_z at $S = 0$ is non-negative because the gravitational force dominates. The minimal velocity of $0\,\mathrm{mm\,s^{-1}}$ is located at $z = -3.0\,\mathrm{mm}$ and results from the no-slip condition of the wall. The influence of AS is already visible at $S = 0.05$. The minimum of Ψ is not located at the wall any more, but at $z = -2.6\,\mathrm{mm}$. The order parameter is negative ($\Psi = -0.8\,\mathrm{mm\,s^{-1}}$). A significant influence of AS can be observed at $S = 0.1$. The order parameter is approximately $-12\,\mathrm{mm\,s^{-1}}$ at this control parameter. As the order parameter is used to quantify the formation of additional vortices, this region is labelled *pattern formation*. In this region, the original buoyancy-driven state has become unstable. The critical point for this type of instability is ca. 0.05.

The order parameter further decreases to $\Psi = -170\,\mathrm{mm\,s^{-1}}$ when increasing the control parameter up to $S = 0.7$. The magnitude of the velocity of the vortices changes, but their positions remain unchanged. The location of minimum is at $z = -2.1\,\mathrm{mm}$. For $S > 0.7$, a qualitatively different flow behaviour occurs. The or-

der parameter Ψ jumps to a much higher value at $S = 0.75$ and stays approximately constant at $S > 0.75$. This jump is related to the symmetry loss of the flow field. The region in Figure 5.21 is therefore named *symmetry breaking*. Here, a second critical point occurs.

The iterations during the solving process show no stable solutions when simulating the completely symmetric model for $S \geq 0.75$. The velocity field significantly changes from one iteration to the other so that no convergence is reached. Two equivalent solutions appear that will be discussed later on in this section (Figure 5.22). The question arises, how the results of the order parameter in Figure 5.21 as well as of the velocity fields in Figures 5.18 and 5.19 were obtained. The solution to this problem is to introduce a certain asymmetry that leads to a convergent simulation process and a stable solution. This solution of the velocity field serves as an initial condition for the next simulation step, in which the asymmetry is reduced. At an asymmetry of zero, the model matches the original one, and the intended solution is obtained.

To introduce an asymmetry, the model was slightly tilted by $\vartheta = +10°$ according to the x-axis. Subsequently, the simulation process converges and results in a stable solution for all S-values. For the next runs, the asymmetry was reduced, i.e. the tilt angles were decreased to $+5°$, $+4°$, $+3°$, $+2°$ and $+1°$. In horizontal position ($\vartheta = +0°$)*, a completely symmetric model was simulated; only the initial conditions for the simulation of the velocity field are asymmetric because these are picked from the results of the previous simulation run ($\vartheta = +1°$). Similarly, simulation runs with negative tilt angles ($-10°$, $-5°$, $-4°$, $-3°$, $-2°$, $-1°$, $-0°$) were performed. The resulting velocity field at $S = 1$ for $\vartheta = +0°$ is shown in Figures 5.18 and 5.19. The velocity field, when approaching the horizontal alignment from negative tilt angles ($\vartheta = -0°$), can be transferred into the velocity field when approaching from positive tilt angles ($\vartheta = +0°$) by a mirroring at the x-z-plane.

The order parameter Ψ in Figure 5.21 shows two fundamental changes of the flow field. The pattern formation can be adequately described by Ψ because the flow pattern remains unaltered, only the velocity field near the arc tube wall changes its direction. However, in the region, in which symmetry breaking occurs, not only the velocity magnitude in negative z-direction changes but also the flow

*The leading $+$-sign indicates that the results were obtained with an initial condition for the velocity field, which was calculated with a positive tilt angle.

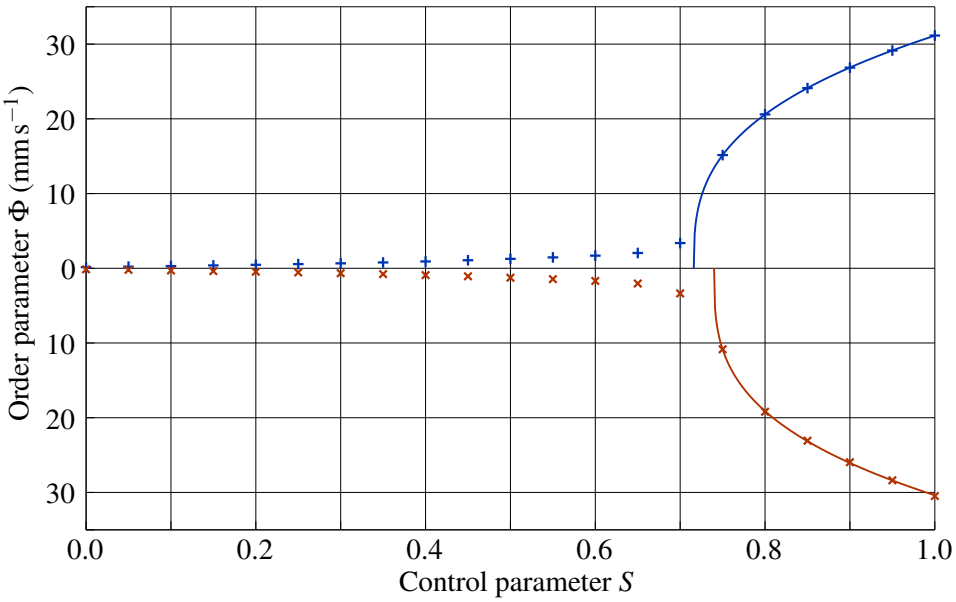

Figure 5.22. Results of the order parameter Φ (crosses) as a function of the control parameter S. The two fit functions (definition see text) are marked by a solid line. The results in the upper part (blue) are obtained by simulating with initial conditions that base on a model with a positive tilt angle ($\vartheta = +1°$). The results in the lower part (red) base on simulations with initial conditions from the solution of $\vartheta = -1°$. Note, that the y-axis only shows positive values because the order parameter is positive by definition.

pattern in the whole arc tube. Therefore, a second order parameter

$$\Phi := \frac{1}{V_\mathrm{r}} \int_{V_\mathrm{r}} |u - \tilde{u}| \, \mathrm{d}V, \tag{5.3}$$

is defined that measures the asymmetry. V_r denotes the right half (positive y-direction) of the interior volume of the arc tube, $u(x,y,z)$ is the velocity magnitude and $\tilde{u}(x,y,z)$ the velocity field $u(x,-y,z)$ that is mirrored at the x-z-plane. Hence, the order parameter Φ is a measure for the mean velocity difference between a point on the right-hand side (x,y,z) and its counterpart on the left-hand side $(x,-y,z)$. For example, the symmetric velocity field at the purely buoyancy-driven flow ($S = 0$) results in $\Phi = 0$, whereas Φ is greater than zero for the velocity field with the AS force ($S = 1$). Figure 5.22 shows the results of the order parameter Φ when approaching the horizontal arc tube position from a positive ($\vartheta = +1°$, blue curve) and from a negative tilt angle ($\vartheta = -1°$, red curve). The order parameters for $S \leq 0.7$ highlight that the velocity field is mirror-symmetric to the x-z-plane.

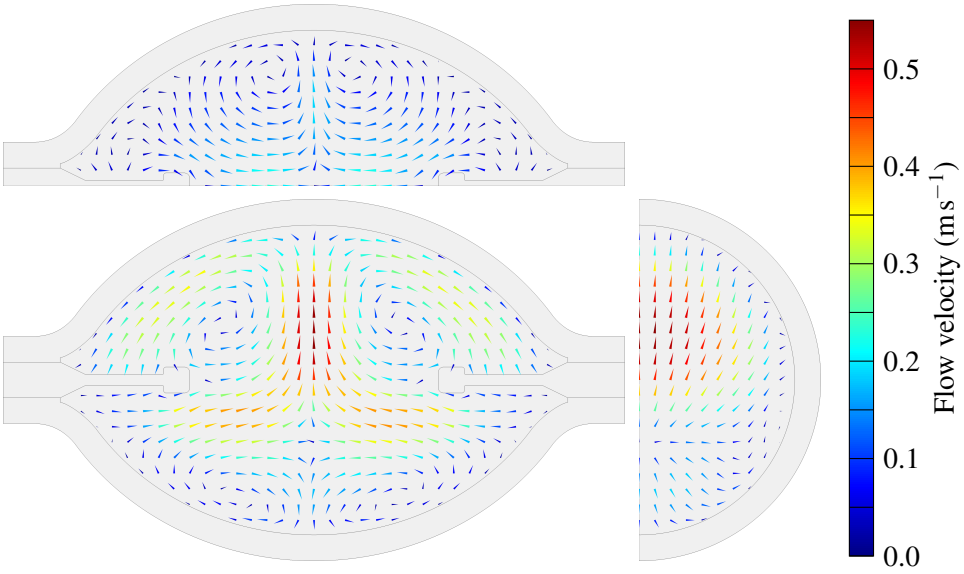

Figure 5.23. Velocity field in three orthogonal planes through the arc tube's centre (top: x-y-plane; bottom left: y-z-plane; bottom right: x-z-plane) driven by the gravitational force and a downscaled AS force ($S = 0.7$).

This symmetrical state is depicted by the y-z-plane and the x-y-plane in Figure 5.23. Compared to the maximal velocity of $0.62\,\mathrm{m\,s^{-1}}$ at $S = 1$ (Figure 5.19), the velocity at $S = 0.7$ is only $0.55\,\mathrm{m\,s^{-1}}$ because of the lower AS force. The small deviations from $\Phi = 0$ for $S < 0.75$ in Figure 5.22 are caused by simulation inaccuracies, especially by the unsymmetrical mesh. In both cases ($\vartheta = +0°$, $\vartheta = -0°$) a significant jump of Φ can be observed at ca. $S = 0.75$. Here, a transition from a mirror-symmetric to an asymmetric state can be observed. Moreover, the order parameter further increases with increasing control parameter S so that the mean velocity difference between a point on the right-hand side (x, y, z) and on the left-hand side $(x, -y, z)$ increases to ca. $30\,\mathrm{mm\,s^{-1}}$.

Furthermore, two functions for $S > 0.7$ are drawn in Figure 5.22. These functions were fitted to a power law $\Phi = a(S - S_{\mathrm{crit}})^{\zeta}$ with the prefactor a, the critical exponent ζ and the critical control parameter S_{crit}. Such a law is also used to describe stability in a ferromagnet [137,188]. The power law shows an excellent agreement with the simulation results. Between the upper and lower fit curve appears to be a considerable deviation, but this bases only on the simulation results at $S = 0.75$. Actually, the order parameters at $S \geq 0.8$ only show small differences. The reason for the discrepancies is the slightly unsymmetrical finite element mesh, which is also responsible for the minor differences of the order parameter from

zero for $S \leq 0.7$.

In the case of the order parameters for $\vartheta = +0^\circ$ (upper curve in Figure 5.22), a critical control parameter of $S_{\text{crit}} = 0.716$ and in the case of the order parameters for $\vartheta = -0^\circ$ (lower curve) $S_{\text{crit}} = 0.740$ results. Therefore, the mean value of the critical control parameter is 0.728. The resulting critical exponents are $\zeta = 0.339$ for the upper curve and $\zeta = 0.316$ for the lower curve. The corresponding mean value is 0.3275.

The mean values inserted in the power law characterise the region, in which no solution can be obtained. The region, which is bounded by the mean values of $\vartheta = +0^\circ$ and $\vartheta = -0^\circ$ of the fit function, is marked by a hatched area in Figure 5.24. Additionally, the figure shows three curves in the upper part of the diagram corresponding to positive tilt angles ($+10^\circ$, $+5^\circ$, $+1^\circ$) and three curves in the lower part of the diagram corresponding to negative tilt angles (-10°, -5°, -1°). Evidently, the results for positive and negative tilt angles also avoid this region. Instead of a jump at S_{crit} for $\vartheta = \pm 0^\circ$, the tilting induces a small asymmetry into the velocity field that is already verifiable at $S = 0$. The small asymmetry due to a $\vartheta = \pm 1^\circ$ tilting is already sufficient to avoid the jump. The resulting curves in Figure 5.24 show a smooth transition from small to high values of the order parameter Φ. As has already been mentioned, the tilting leads to two velocity fields that can be transferred into each other by a mirroring at the x-z-plane. Consequently, the two equivalent states form a supercritical pitchfork bifurcation (see Figure 3.4 (c)).

Figure 5.25 illustrates the conditions at constant S when tilting the lamp from positive (blue curves) to negative (red curves) tilt angles or vice versa. Except for a small jump at $\vartheta = 0$, that is referred to numerical noise, a smooth transition occurs in the subcritical region ($S = 0.6 < S_{\text{crit}}$, open circles). In the supercritical region ($S = 0.8 > S_{\text{crit}}$, full circles), a first order phase transition appears.

The buckling phenomenon, in which an increasing load leads to a mechanical failure [189], as well as a ferromagnet in an external magnetic field [137,188] show a similar behaviour. In the paramagnetic phase, in which the actual temperature T is higher than the Curie temperature T_{Curie}, the material itself is not magnetic. This corresponds to the symmetric velocity field in the subcritical region $S < S_{\text{crit}}$ for a horizontally operated lamp. When the lamp is tilted, the order parameter Φ is not zero. In case of the paramagnetic material, the lamp tilting corresponds to an external magnetic field that imprints a magnetisation. The supercritical region $S > S_{\text{crit}}$ equals the ferromagnetic phase, in which $T < T_{\text{Curie}}$. The magnetisation is

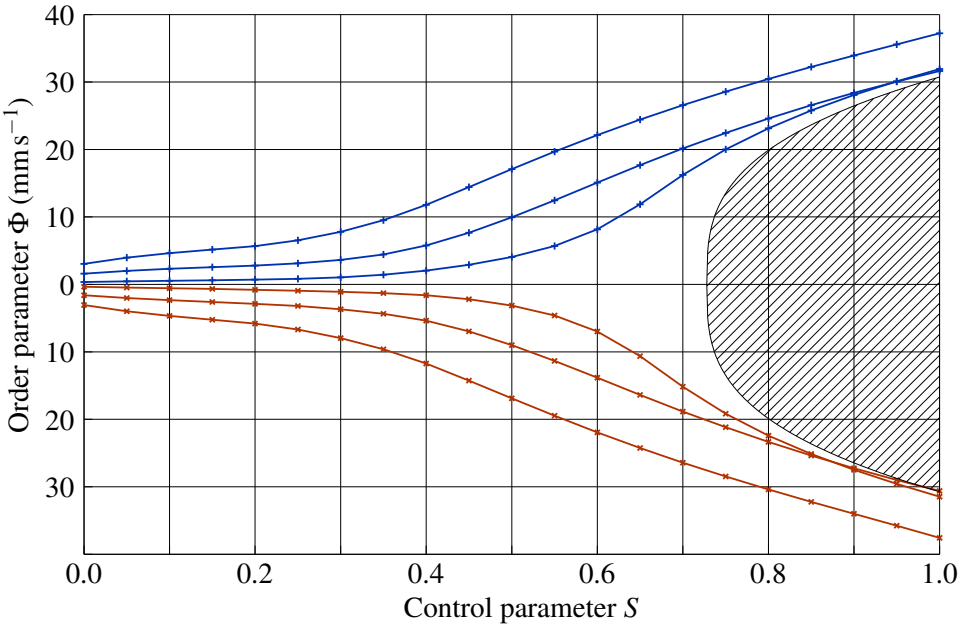

Figure 5.24. Results of the order parameter Φ as a function of the control parameter S for the tilted arc tube. The curves represent the tilt angles $\pm 10°$, $\pm 5°$ and $\pm 1°$. In the upper part, the results for positive tilt angles and in the lower part the results for negative tilt angles are presented. The shaded area is the region, in which no solution can be obtained.

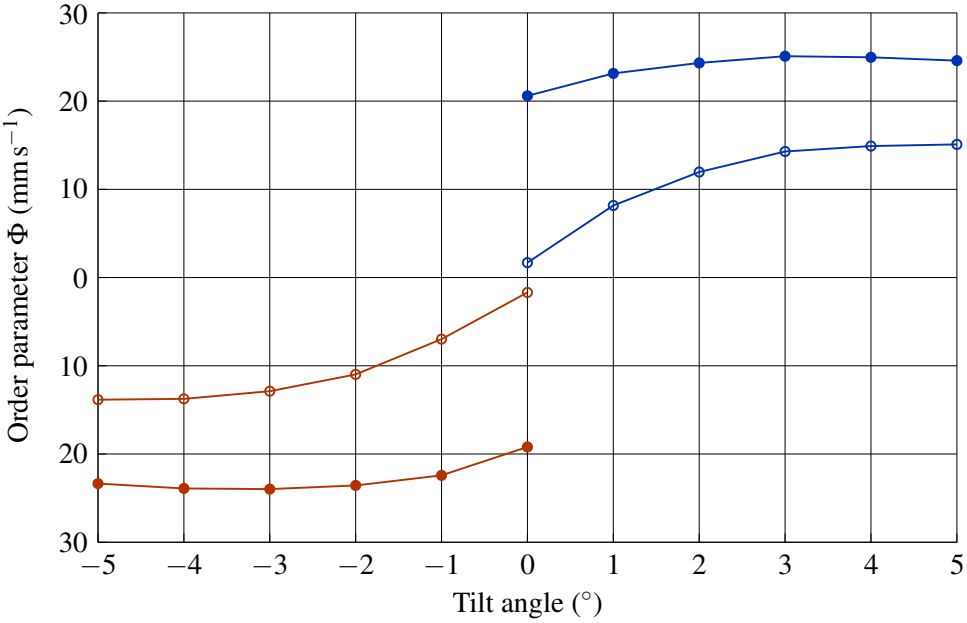

Figure 5.25. Results of the order parameter Φ as a function of the tilt angle ϑ for $S = 0.6 < S_{\text{crit}}$ (open circles) and for $S = 0.8 > S_{\text{crit}}$ (full circles).

unequal zero even though the external magnetic field is absent.

Ernst Ising mathematically described a model of ferromagnetism with statistical methods in 1925 [188]. Nowadays, the Ising model is an established, microscopic model for ferromagnets and many other systems. The magnetic dipole moments of atomic spins can adopt two states $(+1, -1)$ and are usually positioned on a lattice so that the spins of neighbouring nodes interact with each other. This simplified model enables to identify phase transitions for 2D or higher dimensional spaces. The critical exponent ζ for the magnetisation of a 3D Ising model is 0.3265 [190]. In the simulation of the velocity field under the influence of AS, a mean value of $\zeta = 0.3275$ was obtained so that the values differ by only 0.31 %. Nevertheless, this remarkable accordance does most probably not mean that the two systems belong to the same universality class because the systems are qualitatively different.

5.5 Recursion Loop

The preceding chapter considered the influence of the AS force on the velocity field inside the arc tube of the HID lamp. The results show a severe impact and a domination of the AS over the buoyancy-driven fluid flow. In a real lamp, this altered flow field substantially changes the arc position and the temperature field. Additionally, other physical entities, e.g. the electric field, the speed of sound, the eigenfrequencies and the eigenmodes and, therefore, the AS flow field itself, are modified. The simulation results in this chapter include the feedback of AS on these fields with the aid of a recursion loop. This procedure also enables to compare the simulation results to experimental results.

5.5.1 Numerical Investigations

The procedure used to calculate the fluid flow, has to be changed and extended to incorporate the impact of AS on the temperature field and other physical quantities. The general procedures are compared in Figure 4.8, and the single steps are described in detail in Section 4.3.2. In general, the calculation of the fields describing the thermal plasma are coupled with the calculation of the acoustic pressure field and the AS force. This coupling of stationary and eigenvalue simulations enables computation of the results at a certain driving frequency (excitation frequency). The strength of the AS force is controlled by the difference of the eigenfrequency and the selected excitation frequency.

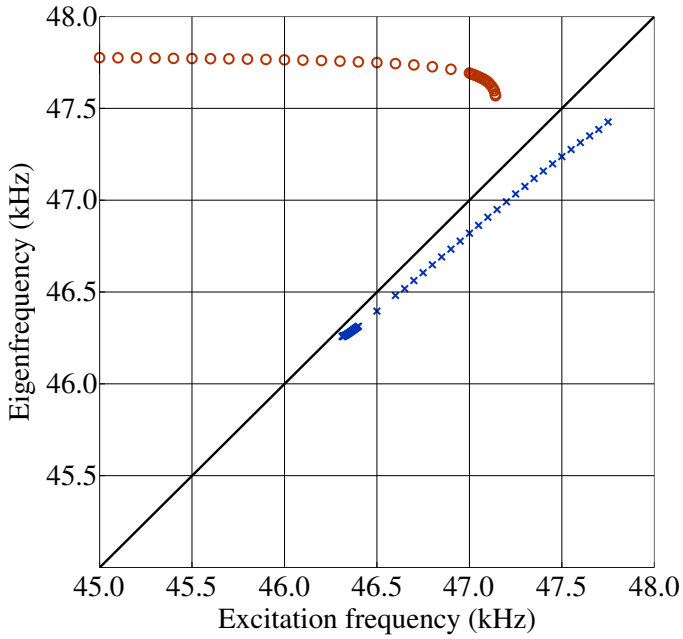

Figure 5.26. The acoustic eigenfrequency as a function of the excitation frequency. The blue crosses indicate simulation results for decreasing excitation frequencies, and the red circles correspond to results for increasing excitation frequencies. The excitation frequency and the eigenfrequency coincide at the black line (resonance).

Initially, the results at an excitation frequency of 47.750 kHz were calculated. The simulation converged quickly at this frequency; the recursion loop was only passed three times until the results of two successive eigenfrequencies differed less than 5 Hz (convergence criterion). The fast convergence originates from the relatively large difference of 324 Hz to the resulting eigenfrequency (47.426 kHz), i.e. the magnitude of the AS force is small. Subsequently, the excitation frequency was decreased by 50 Hz to $f_{\mathrm{ex}} = 47.700\,\mathrm{kHz}$ to approach the eigenfrequency, which results in a lower difference between excitation frequency and eigenfrequency of 315 Hz. The smaller distance to the eigenfrequency results in a stronger AS force that changes the physical conditions inside the arc tube and leads to a shift of the eigenfrequency. This process is further pursued. The results are presented in Figure 5.26. At decreasing excitation frequencies (blue crosses), the system behaves as if the eigenfrequency is repelled from the excitation frequency. However, the difference linearly decreases down to a minimum of 55 Hz at an excitation frequency of 46.313 kHz. The decreasing frequency difference is equivalent to an increasing strength of the AS force. Therefore, more recursion loops were necessary to

reach convergence. Hence, beneath 46.400 kHz a much smaller frequency step size was chosen. Finally, the simulation did not converge, and the iteration steps of the solving process show results that jump between two qualitatively different states. A reason for this behaviour might be that no stationary solution exists so that the model and the stationary solver are inappropriate[†].

Additionally, the whole procedure (multiple recursion loops) was repeated, but in opposite direction. Starting at an excitation frequency of 45.000 kHz, the frequency was increased up to 47.141 kHz. The results (red circles) depicted in Figure 5.26 demonstrate a different behaviour. When increasing the excitation frequency, the eigenfrequency remains nearly unaltered because of a weak AS force. Above 47.000 kHz the eigenfrequency gradually decreases. Here, the step size of the frequency was decreased because otherwise the simulation jumps to the results obtained for decreasing frequency. This indicates that a jump phenomenon exists. It will be treated in detail later on.

In the following, the simulation results of the voltage drop between the electrodes, the acoustic pressure at an antinode, the fluid flow and the temperature field are evaluated. Figure 5.27 shows the voltage drop between the electrodes as a function of the excitation frequency. As Figure 5.26 already highlighted, the results at increasing excitation frequencies (up-ramping) differentiate from those at decreasing excitation frequencies (down-ramping). In case of the ascending frequency, up to $f_{\mathrm{ex}} = 47.000\,\mathrm{kHz}$ the voltage almost remains constant at approximately 84.0 V and increases only 1.0 V when the frequency is increased to $f_1 = 47.141\,\mathrm{kHz}$. A further small raise of the excitation frequency leads to simulation results that correspond to the upper solution branch (blue crosses in Figure 5.27) so that at f_1 the voltage jumps to 87.6 V. In case of the descending frequency, a significant voltage increase of 7.0 V from $f_{\mathrm{ex}} = 47.800\,\mathrm{kHz}$ down to $f_2 = 46.313\,\mathrm{kHz}$ occurs. At even lower frequencies, the simulation did not converge.

The emerging picture is similar to Figure 3.8 that shows the Duffing oscillator with a softening spring ($\beta < 0$). The peak of the response curve tilts to low frequencies leading to an overlap of the upper (down-ramping) and lower (up-ramping) branch. Consequently, more than one stable solution occurs in a certain frequency range (region of bistability). However, the branch representing the unstable solution only appears in the mathematical model and does not naturally result in the

[†] A similar situation appears in the Taylor-Couette flow, in which a transition of the stationary Taylor cells to time-periodic wavy vortices occurs [138].

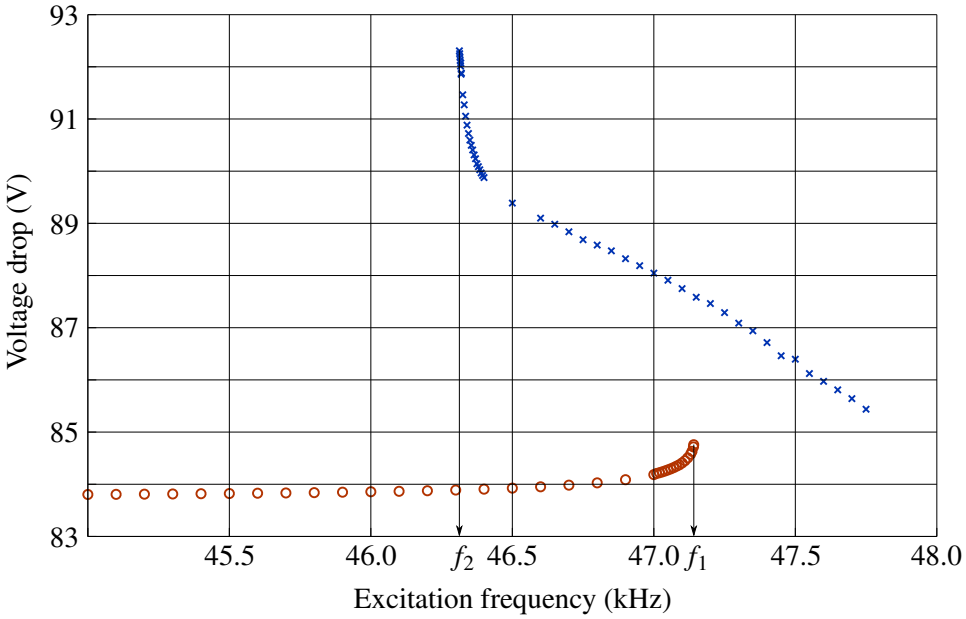

Figure 5.27. The voltage drop between the electrodes as a function of the excitation frequency. The blue crosses mark voltage drops at decreasing excitation frequencies, and the red circles indicate voltage drops at increasing excitation frequencies. Two jumps occur at $f_2 = 46.313\,\mathrm{kHz}$ and $f_1 = 47.141\,\mathrm{kHz}$.

simulation. At the jump frequencies, the solution jumps from the upper to the lower branch or vice versa. The frequencies ω_1 ($f_1 = \omega_1/(2\pi) = 47.141\,\mathrm{kHz}$) and ω_2 ($f_2 = \omega_2/(2\pi) = 46.313\,\mathrm{kHz}$) correspond to the boundaries of the region of bistability. Exactly two solutions coexist at these boundaries. Inside the region of bistability $\omega_2 < \omega < \omega_1$, two stable and one unstable solution exist; outside the region one solution exists.

In Figure 5.28 the acoustic pressure at an antinode as a function of the excitation frequency (acoustic response function) is depicted. The position of the antinode is visualised in Figure 5.9. The up- and down-ramping curves are similar to those of the voltage drop. The results correlate to experimental investigations [63,64], which state a strong hysteresis of the acoustic intensity between an increasing and a decreasing frequency in the vicinity of a resonance. Additionally, the acoustic pressure as a function of the eigenfrequency is shown in Figure 5.28 (green circles and orange crosses). The conversion was conducted with the aid of the data underlying Figure 5.26. Under the reasonable assumption that the resonance frequency and the eigenfrequency lie close to each other, the backbone curve of the Duffing oscillator arises (Figure 3.8).

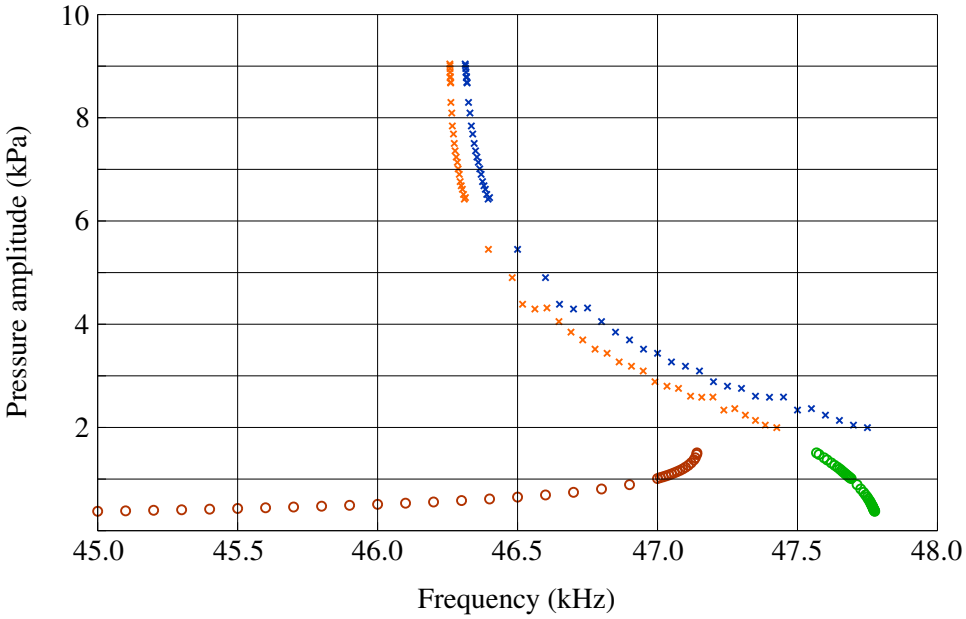

Figure 5.28. Acoustic pressure at an antinode (located at $\vec{r}_5 = (0,0,-2.9)^T$ mm, see Figure 5.9) as a function of the excitation frequency for increasing (red circles) and decreasing (blue crosses) excitation frequencies. Additionally, the acoustic pressure is plotted as a function of the eigenfrequency for increasing (green circles) and decreasing (orange crosses) excitation frequencies.

A qualitative difference to the Duffing oscillator occurs at high pressure amplitudes. The acoustic response curve steepens and even shows a vertical tangent. The softening effect is saturated. The modulus of compression that is equal to the inverse of the compressibility, which is the acoustical analogue of a mechanical spring constant, increases to an altered constant value when the system approaches the eigenfrequency.

To quantify the accordance of the acoustic streaming effect in the HID lamp with the Duffing oscillator, the connecting parameters are estimated. The drop of the mean temperature in the arc tube, which will be discussed later (Figure 5.32), is connected to a decrease of the static pressure P. As the pressure is related to the modulus of compression K [109], a power series around its nominal value is done:

$$K(P) = K_1 + K_2(P - P_0) + K_3(P - P_0)^2 + \dots \tag{5.4}$$

K and K_1 have the unit of measure of a pressure. K_2 is set to zero to be compatible to the Duffing oscillator (Equation 3.43), and K_3 has the unit of measure inverse to a pressure. The acoustic pressure p correlates with the displacement x in the Duffing equation.

Converting Equation 3.47 of the backbone curve to acoustics, results in

$$p_{\mathrm{P}}(\Omega_{\mathrm{P}}) = \sqrt{\frac{8K_1(\Omega_{\mathrm{P}} - 1)}{3K_3}}, \tag{5.5}$$

in which p_{P} stands for the peak acoustic pressure amplitude.

To fit Equation 5.5 to the backbone curve depicted in Figure 5.28, two fit parameters ω_0 and K_1/K_3 are adjusted. The fit bases on the data of the increasing excitation frequency only because of the qualitative difference to the Duffing oscillator at high pressure amplitudes.

Figure 5.29 shows the excellent agreement of the simulated pressure amplitude and the fit with the parameters $f_0 = \omega_0/(2\pi) = 47.8\,\mathrm{kHz}$ and $K_1/K_3 = -191\,\mathrm{kPa}^2$. To estimate K_1 from $c = \sqrt{K_1/\rho}$, the averaged speed of sound $c = 414\,\mathrm{m\,s^{-1}}$ and the averaged mass density $\rho = 24.9\,\mathrm{kg\,m^{-3}}$ of the plasma are evaluated, which results in $K_1 \approx 4260\,\mathrm{kPa}$ and $K_3 \approx -22.3\,\mathrm{kPa^{-1}}$. The negative sign of K_3 characterises the softening effect.

When the discharge arc is acoustically excited, the velocity field inside the arc tube changes. Figure 5.30 shows two simulated velocity fields at approximately

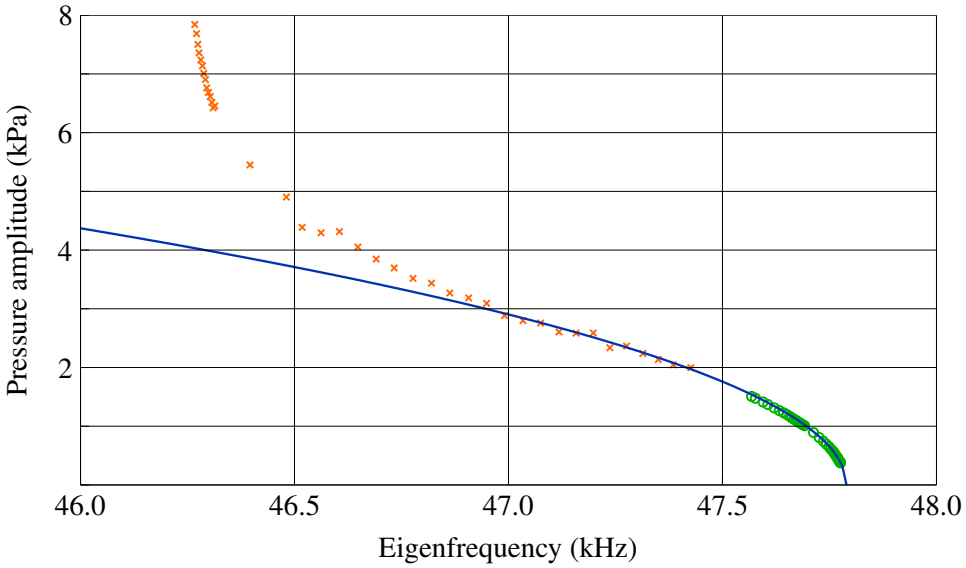

Figure 5.29. Acoustic pressure at an antinode as a function of the eigenfrequency for decreasing (orange crosses) and increasing (green circles) excitation frequencies. The fit curve (blue curve) bases on the increasing values only.

the same excitation frequency, but at different branches of the response curve. The upper set of images presents the velocity field at the lower branch of the response curve. The chosen excitation frequency is 46.300 kHz, which is in direct vicinity of the jump frequency $f_2 = 46.313\,\mathrm{kHz}$. The velocity field is essentially characterised by the buoyancy flow because two counter-rotating vortices appear in the y-z-plane and the flow is upward-directed in the inter-electrode region. Moreover, the maximal velocity of $90\,\mathrm{mm\,s^{-1}}$ is only insignificantly higher than the one of the purely buoyancy-driven flow of $85\,\mathrm{mm\,s^{-1}}$ (Section 5.1.1). The x-y-plane reveals that the velocity field is not fully symmetric, which is caused by the 5° tilting of the model against the horizontal axis. The tilting prevents that the simulation runs into stability problems related to the symmetry breaking transition detected in Section 5.4.2. In addition, the small inclination angle induces an asymmetry that better approximates realistic lamp operating conditions.

The lower set of images in Figure 5.30 corresponds to the upper branch of the response curve at the jump frequency f_2. A completely different velocity field appears that demonstrates the domination of the AS flow over the buoyancy flow. The y-z-plane shows two vortices (right: Clockwise; left: Counterclockwise) in the upper part of the arc tube, whereas the flow in the lower part of the arc tube shows no vortices. Here, the flow points in the direction of the vertical z-axis. Additionally,

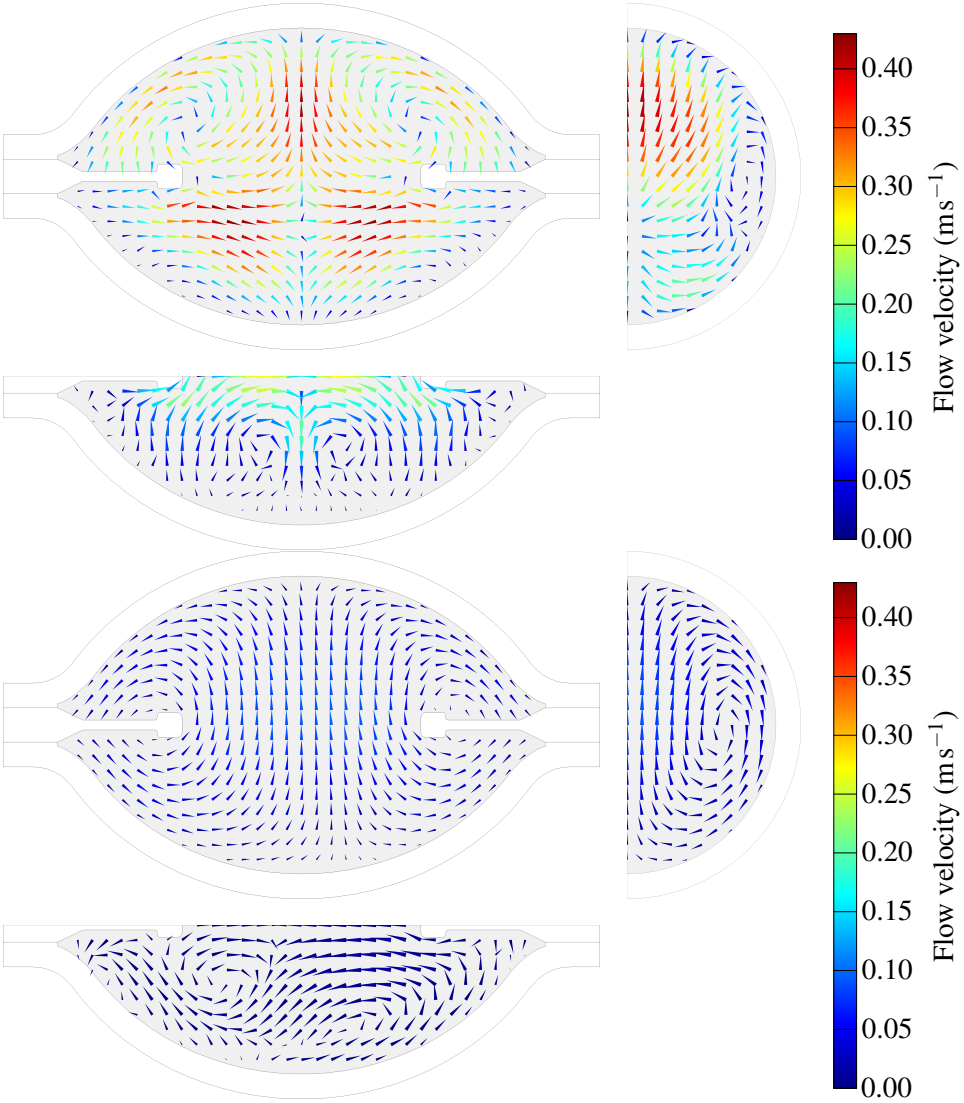

Figure 5.30. Fluid flow inside the arc tube in three orthogonal planes through the centre of the arc tube. The top left image shows the y-z-plane, the top right the x-z-plane and the bottom image the x-y-plane. The upper images depict results from the lower branch of the response curve at an excitation frequency of 46.300 kHz. The lower images belong to the results of the upper branch at the jump frequency $f_2 = 46.313\,\mathrm{kHz}$.

the horizontal plane reveals two counter-rotating vortices. However, the asymmetry in this plane due to the 5° tilting is not visible any more because the AS force is not affected by the model tilting. The maximal velocity is $0.42\,\mathrm{m\,s^{-1}}$, which is 4.7 times larger than the maximal velocity at the lower branch. Nevertheless, the maximal velocity of $0.62\,\mathrm{m\,s^{-1}}$, which resulted in the simulation without the recursion (Figure 5.18), is not reached. The lower velocity is caused by a smaller amplitude of the AS force, which originates because the model in the coupled simulation is excited 55 Hz off the resonance frequency (see above).

Furthermore, the lower set of images in Figure 5.30 clearly illustrates that no symmetry breaking occurs. In the Duffing oscillator (Section 3.3), a symmetry breaking bifurcation arises when the excitation amplitude x_0 exceeds a critical value. Such a bifurcation of the velocity field is observed when just the flow field driven by the AS and the gravitational force is computed (see Section 5.4.2). The symmetry breaking was quantified by the order parameter Φ as a function of the artificial control parameter S. Φ is a measure for the mean velocity difference between a point on the right-hand side (x,y,z) and its counterpart on the left-hand side $(x,-y,z)$. S adjusts the magnitude of the AS force from zero ($S=0$) to maximum ($S=1$). At the critical point $S_{\mathrm{crit}} \approx 0.7$, symmetry breaking sets in. The minimal velocity of u_z on the z-axis at S_{crit} is $\Psi \approx -170\,\mathrm{mm\,s^{-1}}$ (see Figure 5.21).

As the flow field resulting from the recursion loop also shows a downward-directed velocity on the z-axis, Ψ is evaluated for this flow field as well. The difference between the excitation frequency and eigenfrequency serves as a natural control parameter instead of the artificial control parameter S used previously. While up-ramping the excitation frequency, the AS force is negligibly small. Consequently, Ψ is zero for all frequencies, which highlights that the velocity u_z is always upward-directed on the z-axis and only zero at the tube wall.

As opposed to this, Ψ attains negative values when ramping the excitation frequency down. The results are depicted in Figure 5.31 that shows the order parameter Ψ as a function of the control parameter (red circles). Additionally, the z-coordinate, where the minimum of u_z is located, is presented (blue crosses). AS is insignificant for frequencies larger than 47.000 kHz, which can be concluded from $\Psi = 0$. The order parameter decreases to $\Psi = -136\,\mathrm{mm\,s^{-1}}$ from 47.000 kHz to $f_2 = 46.313\,\mathrm{kHz}$. The AS force considerably changes the velocity field, but it is not strong enough to induce symmetry breaking because the minimum limit of $\Psi \approx -170\,\mathrm{mm\,s^{-1}}$ is not reached. The jump phenomenon at f_2 down to the lower branch prevents a symmetry breaking bifurcation.

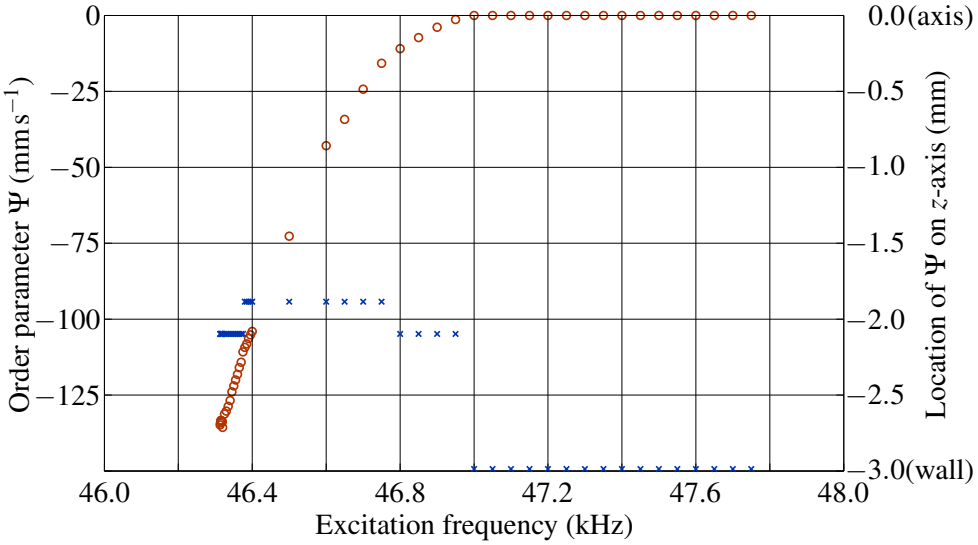

Figure 5.31. Order parameter Ψ as a function of the excitation frequency for decreasing excitation frequencies (red circles). The corresponding axis is located on the left. Additionally, the z-position of the minimal value of u_z is displayed (blue crosses) with its corresponding axis on the right. The symmetry axis of the arc tube is located at $z = 0.0\,\text{mm}$ and the arc tube wall at $z = -3.0\,\text{mm}$.

The altered fluid flow is accompanied by changes of the temperature field. Figure 5.32 shows various temperature profiles for the lower and upper branch of the response curve.

The three images representing the temperature profiles of the lower branch are not distinguishable. Hence, the AS effect is so small that the temperature inside the arc tube is not significantly influenced. The effect is so small that no considerable differences to the temperature field in Figure 5.2, which incorporates the gravitational force only, are discernible. The temperature profile at an excitation frequency of 47.750 kHz, which is well above the region of bistability, is similar to the three profiles related to the lower branch, but already differentiates in detail. In particular, the contour lines in the lower part of the arc tube are slightly deformed into the downward direction. When approaching the jump frequency $f_2 = 46.313\,\text{kHz}$ by decreasing the excitation frequency, the domination of the AS force becomes obvious. This is visualised by the temperature profiles at $f_{\text{ex}} = 46.700\,\text{kHz}$ and $f_{\text{ex}} = 46.313\,\text{kHz}$ that illustrate substantial changes to the original, undisturbed profile. The plasma, that is represented by a high temperature, is dragged towards the bottom wall in the lower part of the arc tube and towards the top wall in the

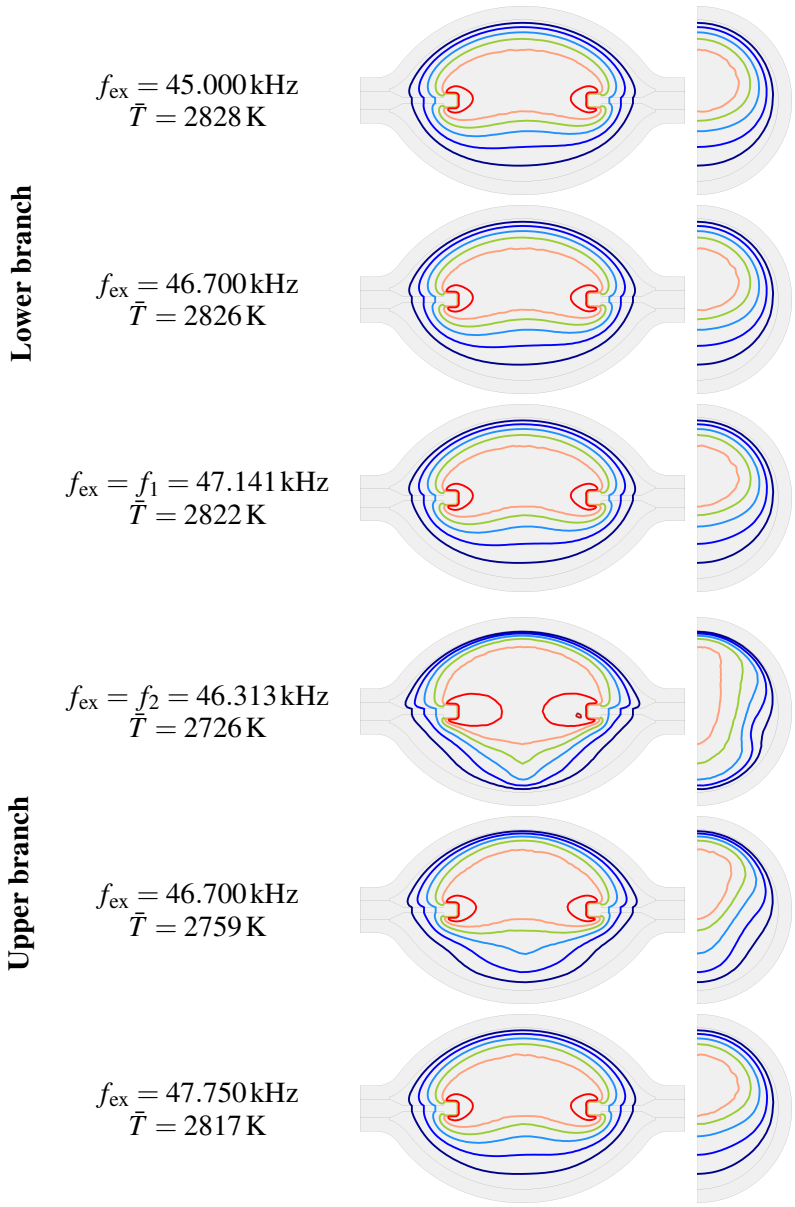

Figure 5.32. Temperature profiles in the y-z- (left) and x-z-plane (right) at three different excitation frequencies f_{ex} for the lower and upper branch, respectively. For the lower branch, $f_{ex} = 45.000\,\mathrm{kHz}$ is located below the region of bistability, $f_{ex} = 46.700\,\mathrm{kHz}$ is inside this region and $f_{ex} = f_1 = 47.141\,\mathrm{kHz}$ denotes the high frequency limit of the region of bistability. For the upper branch, the low frequency limit is located at $f_{ex} = f_2 = 46.313\,\mathrm{kHz}$, $f_{ex} = 46.700\,\mathrm{kHz}$ lies inside the region of bistability and $f_{ex} = 47.750\,\mathrm{kHz}$ is located above this region. The dark blue contour lines correspond to a temperature of 2000 K and the dark red contour lines to 5000 K (step size 500 K). The mean temperature $\bar{T}$ was determined over the interior of the arc tube.

upper part of the arc tube. Both effects are confirmed by the resulting velocity field depicted in Figure 5.30 that shows an increased upward-directed velocity in the upper part and a decreased or even reversed velocity in the lower part compared to the velocity field far off the jump frequency f_2. Consequently, the discharge arc is stretched in the vertical direction and is simultaneously restricted in its horizontal extension.

The maximal temperatures $T_{\max}$ of the hot spots increase with increasing AS force. A maximal temperature of 4818 K occurs without this force (Section 5.1.1), at $f_{\text{ex}} = 45.000\,\text{kHz}$ the maximal value is 4852 K and at the jump frequency f_2 it is 5012 K. Nevertheless, the mean temperature $\bar{T}$ inside the arc tube, which is additionally displayed in Figure 5.32, decreases with increasing AS force. The mean temperature values corresponding to the lower branch (2828 K, 2826 K, 2822 K) as well as $\bar{T} = 2817\,\text{K}$ at $f_{\text{ex}} = 47.750\,\text{kHz}$ (upper branch) are almost identical, whereas the other two mean temperatures (2759 K, 2726 K) are essentially lower. Hence, the strength of the AS correlates to the drop of $\bar{T}$. The reasons for the drop are the large temperature gradients near the walls inside the arc tube that are associated with an increased heat loss [36], which in turn decreases the temperature. This simulated heat flow increase at the onset of arc flicker was also detected in experiments in 1982 [63].

Moreover, the mean temperature $\bar{T}$ enables to find a plausible explanation for the increasing voltage drop between the electrodes in Figure 5.27. A decreasing mean temperature causes a decreasing electric conductivity (see Figure 4.3). Accordingly, a temperature drop implies an increase of the electric resistance of the plasma R_{plasma}. As the nominal lamp power P_{lamp} is kept constant, the voltage drop V_{drop} increases because of the relation $P_{\text{lamp}} = V_{\text{drop}}^2 / R_{\text{plasma}}$.

5.5.2 Experimental Investigations

To validate the results of the numerical simulations, experiments at the lowest frequency, that acoustically excites the discharge arc, were conducted. The voltage drop between the electrodes was measured, and the light intensity distribution was recorded by camera.

In contrast to various other physical quantities, e.g. the acoustic pressure or the fluid flow, the voltage drop between the electrodes can easily be measured experimentally. The experimental measurement method was slightly changed compared to the one used in Section 5.2.2. This time the modulation depth was kept constant, and the excitation frequency was tuned. For the modulation depth, a value of 2 %

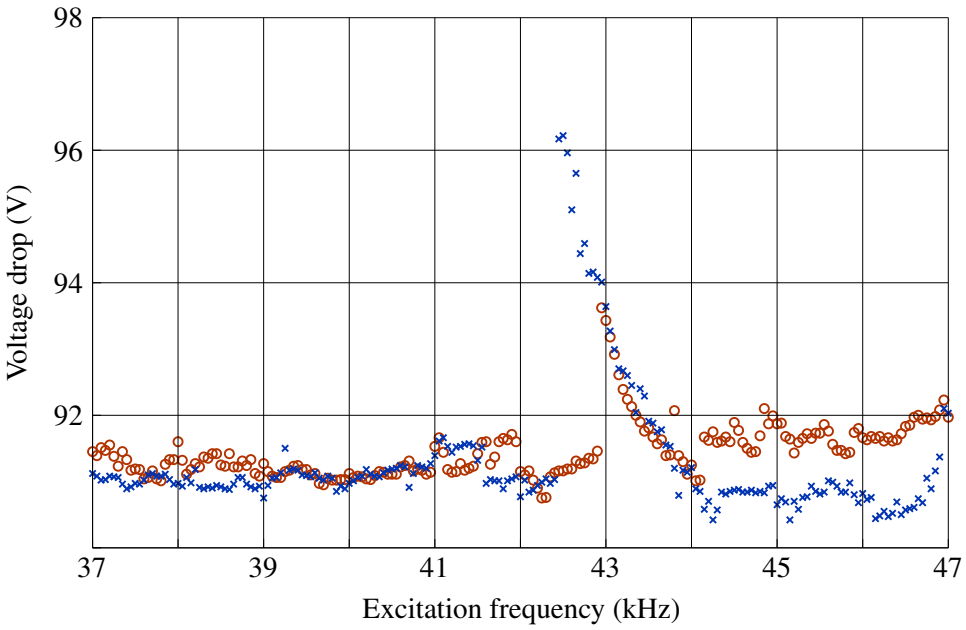

Figure 5.33. Measurement of the voltage drop as a function of the excitation frequency of lamp number 8. The modulation depth in the experiment was $\alpha = 2\,\%$. The red circles correspond to increasing and the blue crosses to decreasing excitation frequencies.

was chosen. The following results show that this value is high enough to stimulate the discharge arc. The frequency was increased from 37 kHz to 47 kHz and decreased again in a second experiment. The resonance at approximately 41.4 kHz (Section 5.2.2) is passed in both cases.

Figure 5.33 shows characteristic measurements of the voltage drop when up- and down-ramping the excitation frequency. In case of the up-ramping (red circles), the voltage initially stays constant at approximately 91.2 V before jumping to 93.6 V at ca. 43.0 kHz. When further increasing the frequency, the voltage decreases back to a lower voltage of ca. 91.7 V. When down-ramping the frequency (blue crosses), the behaviour is similar, but differs in certain key aspects. The voltage increases up to 96.2 V, and, therefore, achieves a much higher value as in case of the up-ramping. Furthermore, the peak voltage occurs at a lower excitation frequency of 42.5 kHz. The significantly higher voltage corresponds to the excitation of an acoustic mode. The fluid flow has changed leading to an altered temperature field and, consequently, to an increased voltage. The results show two voltage jumps: A small jump, when up-ramping the frequency, and a large jump, when down-ramping the frequency. This hysteresis effect appears because the jumps

occur at different excitation frequencies.

The resulting voltage qualitatively accords with experimental investigations of high pressure sodium lamps [62]. Here, a dependence of the AR on the direction of voltage ramping was also detected. The resonances were more pronounced when down-ramping the frequency. Additionally, the measured voltage reached higher values and showed a downward voltage jump when descending the frequency. All these observations correspond to the present investigation, only the absolute values differ because of differences between each lamp.

The voltage measurements were repeated for five other 35 W lamps at a modulation depth of 2 %. These results are presented and discussed in Section 5.5.3.

As a second experimental investigation, the light intensity distribution of the discharge arc during light flicker was recorded by camera. The observed distribution changes were also determined with a photodetector. It confirms that the discharge arc movements recorded by camera coincide with the light intensity fluctuations detected by the photodiode [56]. Similar observations with two cameras were conducted for a vertically operated high-pressure sodium lamp with a nominal power of 70 W [191]. Here, the 3D images highlight that the position of the discharge arc changes when approaching an acoustic resonance frequency and that a lateral deflection can be observed in two directions.

Figure 5.34 shows two exemplary images of the investigated 35 W lamp. The image on the left-hand side presents an intensity distribution at stable operating conditions, i.e. the lamp is driven by a square-wave voltage with a carrier frequency of 400 Hz. The upward bending is caused by the buoyancy, and no acoustically induced flow is present. Contrarily, the impact of AS becomes visible when the operating frequency is tuned to an acoustic eigenfrequency, and a sufficiently high modulation depth is set. The results show that the discharge arc oscillates between its undisturbed position (Figure 5.34, left) and a state with a higher arc deflection at a motion frequency of 9 Hz to 12 Hz [56]. When the modulation depth is further increased to 12 % or higher (depending on the lamp sample), the amplitude of the oscillation increases, and a "movement" of the arc towards the lower part of the arc tube occurs. This transition is depicted in the image on the right-hand side of Figure 5.34. Immediately afterwards the discharge arc started to rotate around the y-axis, and the lamp finally exploded.

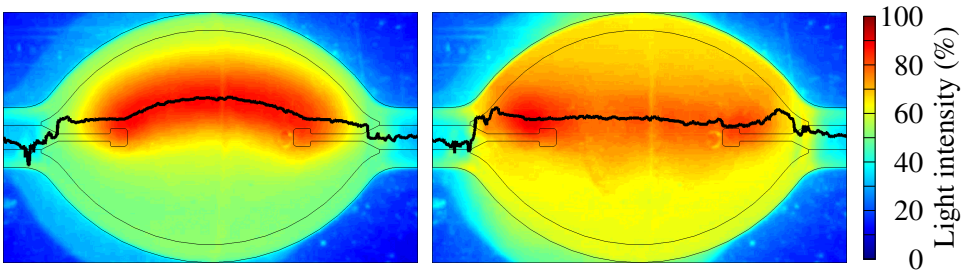

Figure 5.34. Measurements of the light intensity of the discharge arc during stable (left) and unstable (right) operation. The light intensity measurement during unstable operation shows an image of the discharge arc before rotating violently around the lamp axis. The black line indicates the mean position of all light intensity values that are larger than 95 % times the highest light intensity as a function of the y-coordinate.

5.5.3 Comparison and Discussion

In the following, the simulation results of the recursion loop are compared to the experimental results of the eigenfrequency, the voltage and the light intensity measurement.

The eigenfrequencies were already compared in Section 5.2.3. It was detected that the lowest frequency, at which arc flicker in the experiment is induced, corresponds to the second simulated eigenfrequency. The simulation only incorporates the gravitational force, which results in a 6.4 kHz higher frequency compared to the experimental result. The inclusion of the AS force shifts the second eigenfrequency from 47.8 kHz to 46.3 kHz so that the difference reduces to 4.9 kHz. Hence, the simulated eigenfrequency is only 11.8 % higher than the experimental one instead of 15.5 %. The reasons for the remaining difference have already been discussed in Section 5.2.3.

The shape of the discharge arc can be compared by considering the light intensity measurements in Figure 5.34 and the simulated temperature profiles in Figure 5.32. At stable operating conditions or at an excitation frequency far away from resonance, the simulation and the experiment show qualitatively the same distribution that is characterised by the upward bending of the discharge arc caused by buoyancy. At unstable conditions, the experimental light intensity measurement strongly resembles the temperature distribution in the y-z-plane of the upper branch at $f_2 = 46.313\,\mathrm{kHz}$. The discharge arc moves towards the tube centre. In the simulation, no convergence is reached at excitation frequencies lower than f_2 for the upper branch (higher AS force). In the experiment, the arc starts to flicker

chaotically, and finally the arc tube breaks.

Figure 5.35 compares the averaged voltages of the experiment with the resulting voltage of the simulation. In both cases, the excitation frequency is normalised according to $f_\mathrm{n} = (f_\mathrm{ex} - \hat{f}_\mathrm{ex})/\hat{f}_\mathrm{ex}$. $\hat{f}_\mathrm{ex}$ is the frequency at which the highest voltage (down-ramping) occurs. The upper part shows the mean voltages of the experimental results of six lamps. The absolute values essentially vary between the individual lamps; the standard deviation is 2.6 V (see also Section 5.1.2). In the lower part of the figure, the voltage data from the simulation are depicted as a function of the normalised excitation frequency, which is equal to the jump frequency f_2.

Obviously, the behaviour is similar. In both investigations, the hysteresis and the jump phenomenon emerge. Furthermore, the downward voltage jump, when down-ramping the frequency, is in both methods approximately three times higher than the upward voltage jump, when up-ramping the frequency. Nevertheless, the absolute values of the voltage differ. The jump at $f_\mathrm{n} = 1.0$ is 8.4 V in the simulation and 6.5 V in the experiment, and the corresponding jumps at a higher excitation frequency have a height of 2.8 V and 2.1 V, respectively. Moreover, the region of bistability in the simulation ($\Delta f_\mathrm{n} = 0.018$) is wider than its corresponding experimental value ($\Delta f_\mathrm{n} = 0.010$). A reason for this difference is the choice of a modulation depth of 2 % for the experiments. A higher modulation depth increases the region of bistability in the experiment.

The results show very good accordance. However, the electric operating conditions of the experiment and the simulation differ essentially. The square-wave voltage in the experiments was modulated with a 2 % high-frequency sinusoidal voltage (see Section 4.4, Equation 4.17), to detect the jumps and the hysteresis. In the simulation, a direct current was used so that the results corresponds to a modulation depth of 100 %. Consequently, the model underestimates the impact of AS on the discharge arc. This might have various reasons.

First of all, the low temperature of the arc tube filling in the simulation might be a reason. This is caused by simplifications of the electrode geometry and by deviations of the temperature-dependent material parameters (see also Section 5.1.3). Inaccuracies in the temperature field induce errors in the calculation of the four incorporated loss factors (Equations 3.25, 3.26, 3.29, 3.31) used to determine the absolute acoustic pressure. The material properties, e.g. the heat conductivity and the viscosity, as well as the acoustic mode and its corresponding frequency would also change when modifying the temperature of the arc tube filling. All these effects would impact the magnitude of the AS force.

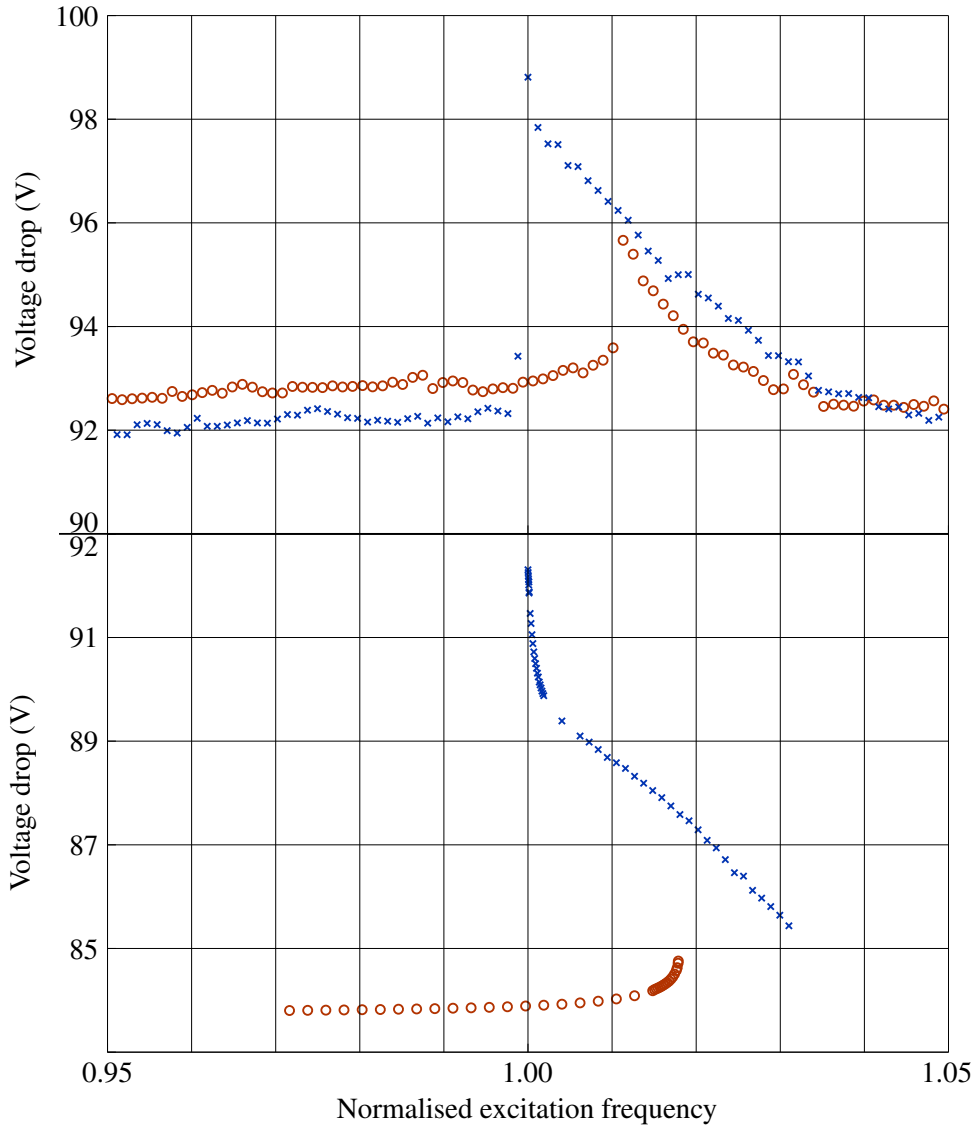

Figure 5.35. Summary of the measurement (top) and the simulation results (bottom) of the voltage drop between the electrodes as a function of the normalised excitation frequency f_n. The red circles mark results for ascending and the blue crosses for descending excitation frequencies.

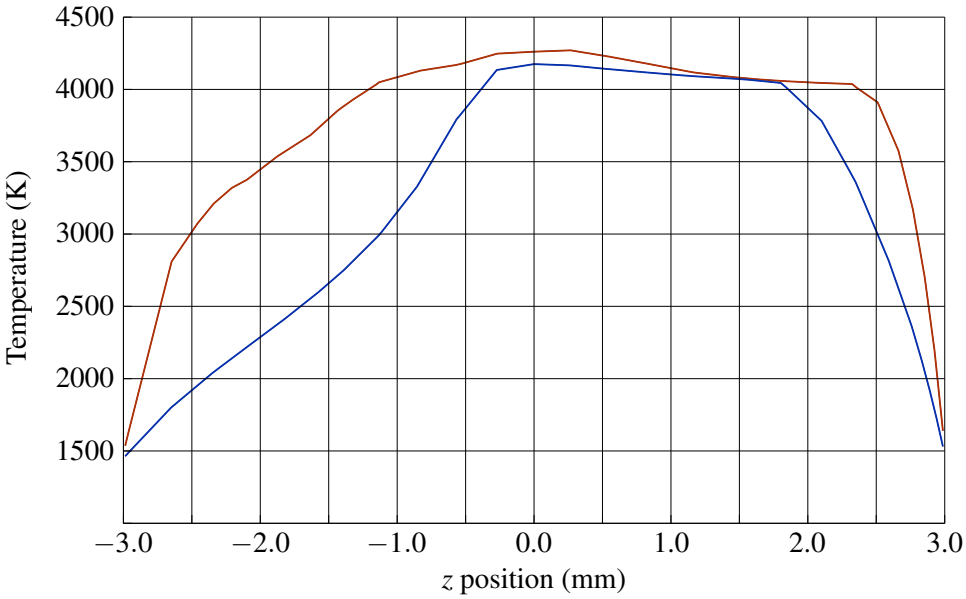

Figure 5.36. Temperature in the arc tube on the vertical axis ($\vec{r} = (0,0,z)^{\mathrm{T}}$ mm). The blue curve corresponds to the simulation driven by the gravitational force only. The red curve represents the resulting temperature of the upper branch at the jump frequency f_2, which additionally includes the AS force.

Another reason for the difference might originate from changes of the chemical composition of the arc tube filling due to the excitation of the discharge arc. The resulting minimal temperature (coldest spot temperature) in the simulation without the AS effect (Section 5.1.1) is 1450 K and, therefore, matches the coldest spot temperature designated to adjust the chemical composition of the arc tube filling. The blue curve in Figure 5.36 corresponds to the simulation driven by the gravitational force only and reveals that the coldest spot is positioned at the bottom of the arc tube ($\vec{r} = (0,0,-3)^{\mathrm{T}}$ mm). Here, the reservoir of liquid metal halides is located. When the discharge arc is acoustically excited at the jump frequency $f_2 = 46.313$ kHz, the coldest spot temperature increases to 1493 K. The red curve in Figure 5.36 shows that this spot is not located at the bottom of the arc tube any more. The minimal temperature of the arc tube fillings shifts to a position close to the electrode ground ($\vec{r} \approx (0,4.9,0)^{\mathrm{T}}$ mm). The temperature at the location of the former coldest spot ($\vec{r} \approx (0,0,-3)^{\mathrm{T}}$ mm) increases to 1536 K. Both effects, the position change and the higher temperature, will cause an additional evaporation of metal halides leading to an altered chemical composition of the arc tube filling. Consequently, the material parameters will change. This can cause an amplifica-

tion of the AS effect, which is not considered by the model because it is based on unalterable material definitions.

Chapter 6

Conclusion and Outlook

A model of the arc tube of a high-intensity discharge lamp was created, whose solution was calculated by the finite element method. To adequately describe the stable discharge arc, the equations comprise the conservation of mass, momentum, energy and charge. For the simulation of the instable behaviour, the inhomogeneous wave equation was solved, and the acoustic streaming effect was implemented. Thus, the model is able to systematically investigate the mechanisms that lead to the origin of the plasma instabilities. The stationary approach enables the solution of a detailed three dimensional arc tube model in horizontal operation in reasonable computing times. On the other hand, only time-independent solutions can be computed so that transient problems cannot be addressed.

The simulation results at stable operating conditions were compared to experimental results of the voltage drop between the electrodes, and the light intensity of the discharge arc that was recorded by camera. Additionally, relevant results of other researchers were used to validate the simulation. The comparison shows that the model can qualitatively describe the crucial physical phenomena. Quantitatively, the simulation computes a 9.1 % lower voltage drop compared to experimental findings. The difference is caused by deviations of the temperature inside the arc tube that are in turn a consequence of geometrical simplifications and inaccurate transport coefficients. The sensitivity analysis reveals the influence of important geometrical dimensions and crucial, mainly temperature-dependent material parameters. The effects are diverse: Changes of the material parameters primarily affect the voltage drop, whereas geometrical modifications also alter the fluid velocity as well as the temperature field inside the arc tube. Overall, the impact of geometrical changes is higher compared to the altered material parame-

ters. The sensitivity analysis reveals explanations for the differences between the simulation results and experimental findings.

The modes obtained in this way were used to solve the inhomogeneous wave equation with a loss factor approach. Naturally, the results contain the impact of the stable fields so that the second eigenfrequency of the simulation and the experiment differ by 15.5 %, when the fluid inside the arc tube is driven by the gravitational force only. Further investigations show that this difference reduces to 11.8 %, when both forces, the gravitational and the acoustic streaming force, drive the fluid. The sensitivity analysis demonstrates that the frequency of the second eigenmode, which was further investigated, is mainly influenced by the arc tube size and only in second instance by the temperature field. The acoustic pressure amplitude was computed assuming a Lorentzian shape of the response function and incorporating heat conduction as well as shear stress losses that occur in the boundary layer and in the bulk of the fluid.

The acoustic response function, i.e. the acoustic pressure as a function of the excitation frequency, enables computation of the acoustic streaming force so that its influence on the discharge arc could be analysed. The impact of the additional acoustic streaming force of the first eigenmode at approximately 33.1 kHz on the velocity field is negligibly small, which is in agreement with experimental results that do not experience an altered flow field in this frequency range. The limited impact originates from the small overlap of the first acoustic mode with the power density of heat generation. Contrarily, the velocity field of the second eigenmode at approximately 47.8 kHz significantly changes under the influence of acoustic streaming. The maximal velocity inside the arc tube with an inner diameter of 6 mm is approximately $0.62\,\mathrm{m\,s^{-1}}$, which is seven times higher than the purely buoyancy-driven flow field. The flow pattern is in accordance with theoretical expectations of an acoustically induced flow in a Kundt's tube. The results additionally reveal a phase transition of the fluid flow from a stable to an unstable state when increasing the magnitude of the acoustic streaming force. A symmetry breaking of the flow field occurs at the critical point so that a transcritical bifurcation appears.

As the movement of the discharge arc is accompanied by changes of the temperature field and the electric field, a recursion loop was implemented to investigate the impact of acoustic streaming on these fields. This procedure enables computation of the correct stationary fields at specified excitation frequencies.

The resulting voltage drop, temperature distribution and velocity field show a severe impact caused by the acoustic streaming force of the second eigenmode.

The maximal velocity is more than four times higher than the purely buoyancy-driven flow. This induces an altered temperature distribution, which is confirmed by experimental measurements of the light intensity distribution. The voltage drop is in very good accordance to experimental results. Both show a significant increase when approaching the resonance frequency.

Furthermore, a jump phenomenon and a hysteresis were detected by simulations and experiments. When the excitation frequency is increased from a frequency below the second eigenfrequency, the voltage initially remains constant before jumping to a significantly higher voltage. Contrarily, the voltage drop between the electrodes initially increases when decreasing the excitation frequency from a frequency above the second eigenfrequency. The voltage drop jumps down to a significantly lower value at a certain frequency. The hysteresis develops because the two jumps appear at different excitation frequencies. The upward voltage jump occurs at ca. 47.1 kHz and the downward jump at ca. 46.3 kHz in the simulation. These effects are similar to those of a Duffing oscillator with a softening spring. The results of the model and the experiment are in good accordance. However, the impact of acoustic streaming is strongly underestimated by the simulations. This has various reasons: (1) deviations of the simulated temperature field to the real temperature, (2) approximations in the loss factor approach when calculating the absolute pressure of the acoustic mode and (3) material functions that do not consider the changing chemical composition inside the arc tube when the temperature distribution inside the arc tube changes.

The violent changes of the discharge arc, when the lamp is operated near an acoustic resonance, result in flicker. During flicker, the discharge arc jumps between both stable solutions, which are characterised by different discharge arc positions, different voltage drops and, consequently, different light intensities. The model represents this behaviour. Furthermore, it enables investigation of light flicker at different operating conditions. This study has conclusively shown that a numerical model can be used to investigate the arc flicker phenomenon in high-intensity discharge lamps.

In the following, the research questions asked in Section 2.4 are answered:

- Can the acoustic streaming effect qualitatively and quantitatively explain the arc flicker phenomenon in the HID lamp?
  The results show that acoustic streaming inside the arc tube causes movements of the discharge arc which are accompanied by undesirable light fluctuations. A consideration of the acoustic streaming effect in the simulation

reveals its severe impact on various physical quantities, e.g. the electric potential drop between the electrodes changes significantly at the investigated acoustic eigenfrequency. The simulation results qualitatively coincide with experimental measurements that show movements of the discharge arc at the investigated acoustic eigenfrequency. Quantitatively, a difference between the simulation results and the experimental measurements was detected.

- Which simulation data and/or experimental parameters enable quantification of the acoustic streaming effect?
  The acoustic streaming effect changes the flow field inside the arc tube because an additional force is induced at an acoustic eigenfrequency. The alteration of the velocity field was extensively investigated by simulations. Direct measurements of the flow field are difficult to realise because of the small dimension of the arc tube, the material of the tube wall and the light emission. For an experimental quantification of the acoustic streaming effect, the voltage drop between the electrodes during flicker was measured. This quantity is also available in the simulations. Light intensity measurements and simulated temperature fields provide additional information about the impact of acoustic streaming.

- Why does not every acoustic resonance excite visible discharge arc motions?
  The pressure distribution of every acoustic eigenmode is different, whereas the spatial distribution of the source term inside the arc tube responsible for the acoustic excitation remains constant. A prerequisite for visible light flicker is that the source term and the pressure antinodes of the eigenmode overlap. Hence, light flicker occurs at the second eigenfrequency but not at the first eigenfrequency.

- How do geometries and materials in the HID lamp influence the physical fields inside the arc tube and the acoustic resonance frequencies that deteriorate the light quality?
  A modification of the electric conductivity of the plasma affects the voltage drop between the electrodes, and a changed dynamic viscosity as well as thermal conductivity changes the maximal velocity. Apart from that, the simulations show no significant changes when modifying the material properties of the plasma. Geometrical modifications of the arc tube and of the electrode distance show significantly higher changes on the physical fields inside the arc tube as well as the second eigenfrequency compared to the

altered material properties, e.g. a small enlargement of the overall lamp size significantly decreases the frequency of the second eigenmode.

- Which experimental data (optical, electrical and acoustical) can verify the numerical results, and are the results of the experiment and the simulation consistent?
  In the experimental setup, optical and electrical measurement devices were implemented. Acoustical measurements were not conducted. In case of the electrical measurement, the voltage drop between the electrodes was chosen to verify the numerical results. The results of the experiment and the simulation were qualitatively consistent during stable as well as instable operation. In the absolute values of the voltage drop, a difference between the simulation results and the experimental measurements occurred. This qualitative accordance and quantitative difference was also detected between optical measurements of the discharge arc by camera and simulation results of the temperature distribution or, respectively, the integrated Planck radiation.

The developed and verified simulation model facilitates the study of acoustic resonances that lead to light flicker in high-intensity discharge lamps. The findings help to understand the underlying physical processes considerably better, which is crucial for an improvement of the lamp and driver design. The validated model enables development of new lamp systems that operate at stable conditions, possess an improved energy efficiency, are less bulky, are characterised by lower costs and have a reduced amount of mercury or even avoid this heavy metal. The simulation of instable discharge arc behaviour allows to design new electronic drivers that operate in the high frequency range and, therefore, have a significantly higher energy efficiency compared to state-of-the-art lamps. Moreover, the model is helpful to identify acoustic eigenmodes that induce a fluid flow that causes arc straightening, which is equivalent to a stabilisation of the discharge arc and leads to a further increased energy efficiency.

For further investigation of the acoustically induced streaming field in high-intensity discharge lamps, some advancements are recommended. First, it would be beneficial to compare the simulation results to additional experimental data. Especially, the velocity field inside the arc tube is of interest because it induces the arc flicker. Instead of an indirect detection of the fluid flow by voltage and light intensity measurements or by theoretical considerations, experimental results

would be useful in benchmarking the simulation. The laser Doppler anemometry enables such measurements, but requires special lamp types with a transparent arc tube material and, therefore, necessitates a simulation model with a different geometry and adjusted transport coefficients.

Further investigations should address the deviations of the simulated temperature field to experimental findings. The simplified electrode geometry should be modelled in detail to compute its influence. Furthermore, the current-carrying electrode surface and additional effects on the electrodes (radiation cooling, heating by ion current, cooling by electron emission, etc.) should be investigated to increase the accuracy of the simulation.

The simulation of the recursion loop did not converge if the excitation and resonance frequency lie very close to one another and, consequently, the magnitude of the acoustic streaming force is high. It would be interesting to investigate whether the resulting flow field at this conditions is stable or not. This can be accomplished with the aid of a linear stability analysis. Moreover, the results of the recursion loop reveal multiple solutions at certain excitation frequencies and a hysteresis. The multiplicity of solutions and the hysteresis effect are supposed to be responsible for light flicker. Furthermore, the results are similar to those of a Duffing oscillator with a softening spring. Hence, an interesting topic is the suppression or, respectively, the reversal of the softening effect. These might be appropriate remedies to solve the light flicker problem in high-intensity discharge lamps.

To develop new, energy-efficient, ecologically sustainable and compact electronic drivers, the simulation can be extended to test the influence of acoustic streaming on further acoustic modes so that a map of prohibited frequencies areas would result. An optimisation of the arc tube geometry would then be able to enlarge the frequency ranges, at which stable lamp operation is possible. Similarly acoustic modes, which straighten the discharge arc, can be detected, and the frequency areas can be enlarged by an optimisation process.

Appendix A

Technical Drawings

Figure A.1 shows technical drawings of the simulation and the CAD model. The drawings belong to the investigated *Philips* MASTERColour CDM-T Elite 35 W/930. Both models are compared in Section 4.3.2.

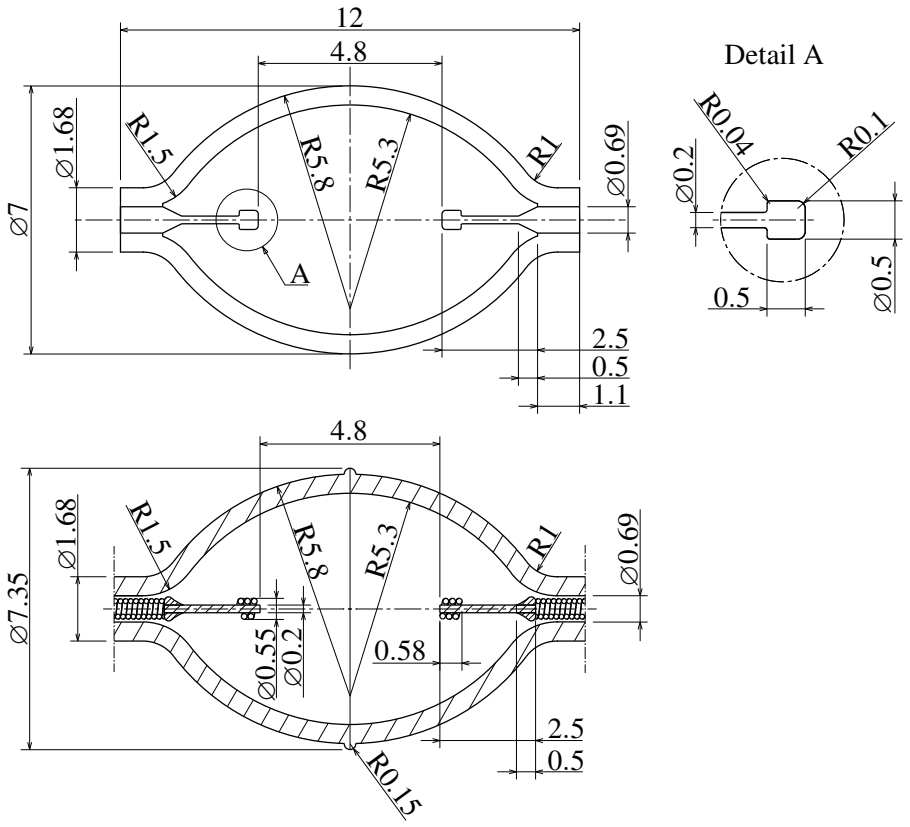

Figure A.1. Technical drawings of the simulation model (top) and of the CAD model (bottom) in the y-z-plane. All dimensions are shown in mm.

Appendix B

Simulation Process

Figure B.1 shows the course of the residual, which is defined in Equation 4.8. The parameters used to create the finite element mesh lists Table 4.1. The computing time for the eight iterations was 2002 s. The solution was approximated with the *PARDISO* solver (see Section 4.3.1)

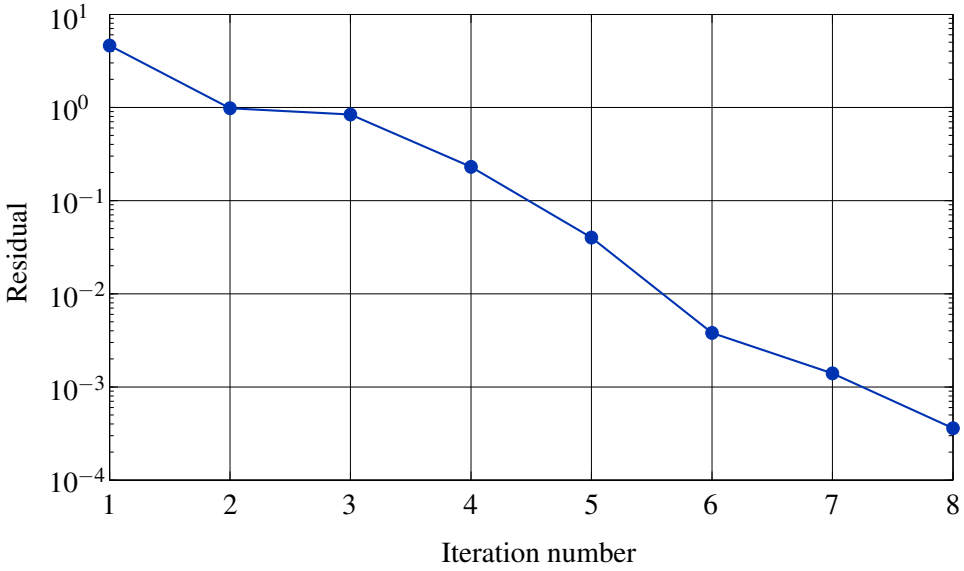

Figure B.1. Course of the residual during the solving process of the stationary simulation. The simulation is considered successful when the residual is below 10^{-3}.

Bibliography

[1] W. W. Stoffels, A. H. F. M. Baede, J. A. M. van der Mullen, M. Haverlag, and G. Zissis. Definition of a high intensity metal halide discharge reference lamp. *Meas. Sci. Technol.*, 17(11):N67–N70, 2006.

[2] G. Zissis and M. Haverlag. Diagnostics for electrical discharge light sources: Pushing the limits. *J. Phys. D: Appl. Phys.*, 43(23):230301, 2010.

[3] P. Waide and S. Tanishima. *Light's labour's lost: Policies for energy-efficient lighting*. OECD and International Energy Agency, Paris, France, 2006.

[4] R. Dohlus. *Lichtquellen*. De Gruyter, Berlin, Germany, 2015.

[5] McKinsey & Company. Lighting the way: Perspectives on the global lighting market, 2012. URL http://www.mckinsey.de/sites/mck_files/files/Lighting_the_way_Perspectives_on_global_lighting_market_2012.pdf. Last visited 15. Apr. 2016.

[6] K. Stockwald, H. Kaestle, and H. Weiss. Significant efficacy enhancement of low wattage metal halide HID lamp systems by acoustically induced convection configuration. In *Proc. Int. Conf. Plasma Sci.*, page 1, Piscataway, 2008. IEEE.

[7] K. Stockwald, H. Kaestle, and H. Ernst. Highly efficient metal halide HID systems with acoustically stabilized convection. *IEEE Trans. Ind. Appl.*, 50 (1):94–103, 2014.

[8] National Electrical Manufacturers Association. NEMA standards publication LSD 54-2010: The strengths and potentials of metal halide lighting systems, 2010.

[9] M. Kettlitz, J. Rarbach, and J. Zalach. Investigation of acoustic resonances in high-power lamps. *J. Phys. D: Appl. Phys.*, 44(14):145205, 2011.

[10] U.S. Department of Energy. High intensity discharge lighting technology report, 2005. URL http://apps1.eere.energy.gov/buildings/publications/pdfs/corporate/hid_workshop-report.pdf. Last visited 16. Apr. 2016.

[11] T. Yasuda, T. Suwa, S. Naoki, A. Saito, A. Maehara, A. Okada, N. Komatsu, and H. Asano. Light sources and lighting circuits. *J. Light & Vis. Env.*, 33 (3):161–177, 2009.

[12] A. Lamouri, A. Naruka, J. Sulcs, C. V. Varanasi, and T. R. Brumleve. Influence of electrode, buffer gas and control gear on metal halide lamp performance. *J. Phys. D: Appl. Phys.*, 38(17):3028–3032, 2005.

[13] J. F. Waymouth. Metal halide lamps. *Proc. IEEE*, 59(4):629–633, 1971.

[14] H.-P. Stormberg. Axial and radial segregation in metal halide arcs. *J. Appl. Phys.*, 52(5):3233–3237, 1981.

[15] E. Fischer. Axial segregation of additives in mercury-metal-halide arcs. *J. Appl. Phys.*, 47(7):2954–2960, 1976.

[16] J. J. Curry, H. G. Adler, W.-K. Lee, and S. D. Shastri. Direct observation of de-mixing in a ceramic metal-halide arc lamp. *J. Phys. D: Appl. Phys.*, 36 (13):1529–1534, 2003.

[17] W. W. Stoffels, T. Nimalasuriya, A. J. Flikweert, and H. C. J. Mulders. Discharges for lighting. *Plasma Phys. Control. Fusion*, 49(12B):B505–B512, 2007.

[18] M. L. Beks, J. van Dijk, B. Hartgers, and J. J. A. M. van der Mullen. A study on the effects of geometry on demixing in metal–halide lamps. *IEEE Trans. Plasma Sci.*, 35(5):1335–1340, 2007.

[19] R. J. Zollweg, R. W. Liebermann, and D. K. McLain. A radiation and convection model of the vertical mercury arc containing sodium and scandium iodides. *J. Appl. Phys.*, 52(5):3293–3303, 1981.

[20] W. M. Keeffe. Recent progress in metal halide discharge-lamp research. *IEE Proc. A: Phys. Sci. Meas. Instrum. Manag. Educ. Rev.*, 127(3):181–189, 1980.

[21] Nobel Media AB. The Nobel Prize in Physics 2014, 2014. URL http://www.nobelprize.org/nobel_prizes/physics/laureates/2014/. Last visited 16. Apr. 2016.

[22] U.S. Department of Energy. Solid-state lighting research and development: Multi-year program plan, 2014. URL http://apps1.eere.energy.gov/buildings/publications/pdfs/ssl/ssl_mypp2014_web.pdf. Last visited 16. Apr. 2016.

[23] Y. Narukawa, M. Ichikawa, D. Sanga, M. Sano, and T. Mukai. White light emitting diodes with super-high luminous efficacy. *J. Phys. D: Appl. Phys.*, 43(35):354002, 2010.

[24] J.-K. Sheu, F.-B. Chen, Y.-C. Wang, C.-C. Chang, S.-H. Huang, C.-N. Liu, and M.-L. Lee. Warm-white light-emitting diode with high color rendering index fabricated by combining trichromatic InGaN emitter with single red phosphor. *Opt. Express*, 23(7):A232, 2015.

[25] E. F. Schubert. *Light-emitting diodes*. Cambridge University Press, Cambridge, UK, 2nd edition, 2006.

[26] G. A. Trestman. Minimizing cost of HID lamp electronic ballast. In *Proc. Ind. Electron. Soc. Ann. Conf.*, pages 1214–1218, Piscataway, 2002. IEEE.

[27] J. Olsen and T. D. Dreeben. Experimental and simulated straightening of metal halide arcs using power modulation. *IEEE Trans. Ind. Appl.*, 47(1): 368–375, 2011.

[28] M. Born. Investigations on the replacement of mercury in high-pressure discharge lamps by metallic zinc. *J. Phys. D: Appl. Phys.*, 34(6):909–924, 2001.

[29] T. G. M. M. Kappen. Status quo of ceramic material for metal halide discharge lamps. *J. Phys. D: Appl. Phys.*, 38(17):3033–3039, 2005.

[30] G. M. J. F. Luijks, S. Nijdam, and H. A. van Esveld. Electrode diagnostics and modelling for ceramic metal halide lamps. *J. Phys. D: Appl. Phys.*, 38 (17):3163–3169, 2005.

[31] G. M. J. F. Luijks, H. A. van Esveld, S. Nijdam, and P. A. M. Weerdesteijn. AC electrode diagnostics in AC-operated metal halide lamps. *J. Phys. D: Appl. Phys.*, 41(14):144006, 2008.

[32] M. W. Fellows. A study of the high intensity discharge lamp-electronic ballast interface. In *Proc. Ind. Appl. Soc. Ann. Meeting*, pages 1043–1048, Piscataway, 2003. IEEE.

[33] P. Flesch and M. Neiger. AC modelling of D2 automotive HID lamps including plasma and electrodes. *J. Phys. D: Appl. Phys.*, 37(20):2848–2862, 2004.

[34] E. Fischer. The column of a DC arc burning in a metal halide atmosphere. *J. Appl. Phys.*, 45(8):3365–3373, 1974.

[35] W. van Erk. Transport processes in metal halide gas discharge lamps. *Pure Appl. Chem.*, 72(11):2159–2166, 2000.

[36] J. F. Waymouth. *Electric discharge lamps*. M.I.T. Press, Cambridge, UK, 1971.

[37] Y. P. Raizer. *Gas discharge physics*. Springer, Berlin, Germany, 1991.

[38] P. Flesch. *Light and light sources: High-intensity discharge lamps*. Springer, Berlin, Germany, 2006.

[39] A. Kloss, H. Schneidenbach, H. Schöpp, H. Hess, L. Hitzschke, and B. Schalk. Electrode-sheath voltages in high-pressure mercury arcs. *J. Appl. Phys.*, 88(3):1271–1275, 2000.

[40] W. Elenbaas. *The high pressure mercury vapor discharge*. North-Holland, Amsterdam, Holland, 1951.

[41] J. C. A. Antón, C. Blanco, F. J. Ferrero, J. C. Viera, and G. Zissis. Measurement system for characterization of high intensity discharge lamps (HID) operating at high frequency. In *Proc. Instrum. & Meas. Technol. Conf.*, pages 1359–1363, Piscataway, 2003. IEEE.

[42] J. Zhou, L. Ma, and Z. Qian. A novel method for testing acoustic resonance of HID lamps. In *Proc. Appl. Power Electron. Conf.*, pages 480–485, Piscataway, 1999. IEEE.

[43] Y. C. Hsieh, C. S. Moo, H. W. Chen, and M. J. Soong. Detection of acoustic resonance in metal halide lamps. In *Proc. Int. Symp. Ind. Electron.*, pages 881–885, Piscataway, 2001. IEEE.

[44] W. Yan, E. Y. K. Ho, and S. Y. R. Hui. Investigation on methods of eliminating acoustic resonance in small wattage high-intensity-discharge (HID) lamps. In *Proc. Ind. Appl. Soc. Ann. Meeting*, pages 3399–3406, Piscataway, 2000. IEEE.

[45] W. Yan, E. Y. K. Ho, and S. Y. R. Hui. Stability study and control methods for small-wattage high-intensity-discharge (HID) lamps. *IEEE Trans. Ind. Appl.*, 37(5):1522–1530, 2001.

[46] R. Redl and J. D. Paul. A new high-frequency and high-efficiency electronic ballast for HID lamps: Topology, analysis, design, and experimental results. In *Proc. Appl. Power Electron. Conf.*, pages 486–492, Piscataway, 1999. IEEE.

[47] M. H. Ohsato, Q. Mao, H. Ohguchi, T. Shimizu, G. Kimura, and H. Takagi. Megahertz operation of voltage-fed inverter for HID lamps using distributed constant line. *IEEE Trans. Ind. Appl.*, 34(4):747–751, 1998.

[48] A. J. Flikweert, T. Nimalasuriya, C. H. J. M. Groothuis, G. M. W. Kroesen, and W. W. Stoffels. Axial segregation in high intensity discharge lamps measured by laser absorption spectroscopy. *J. Appl. Phys.*, 98(7):073301, 2005.

[49] J. T. Dakin, T. H. Rautenberg, and E. M. Goldfield. Anatomy of a vertical metal halide discharge. *J. Appl. Phys.*, 66(9):4074–4088, 1989.

[50] L. Laskai, P. N. Enjeti, and I. J. Pitel. White-noise modulation of high-frequency high-intensity discharge lamp ballasts. *IEEE Trans. Ind. Appl.*, 34(3):597–605, 1998.

[51] H. de Sá, L. M. F. Morais, P. F. Donoso-Garcia, S. I. Seleme, and P. C. Cortizo. Harmonic current injection to avoid acoustic resonance in 70W HPS lamps. In *Proc. 11th Power Electron. Conf.*, pages 372–377, Piscataway, 2011. IEEE.

[52] H. Peng, S. Ratanapanachote, P. N. Enjeti, L. Laskai, and I. J. Pitel. Evaluation of acoustic resonance in metal halide (MH) lamps and an approach to detect its occurrence. In *Proc. Ind. Appl. Soc. Ann. Meeting*, pages 2276–2283, Piscataway, 1997. IEEE.

[53] R. F. Lovasoa, R. A. Zely, L. D. Dorin, and D. Elena. Energetic aspects of the HID ballast used in the outdoor lighting. In *Proc. Int. Conf. Ele. & Power Eng.*, pages 340–346, Piscataway, 2012. IEEE.

[54] J. Cardesín, J. García-García, J. Ribas, J. M. Alonso, A. J. Calleja, E. Corominas, M. Rico-Secades, and M. Dalla. Low-cost PFC electronic ballast for 250W HID lamps operating as constant power source with 400kHz switching frequency. In *Proc. Power Electron. Spec. Conf.*, pages 1130–1135, Piscataway, 2005. IEEE.

[55] J. C. A. Antón, C. Blanco, F. J. Ferrero, J. C. Viera, N. Bordel, A. Martín, and G. Zissis. An acoustic resonance band detection workbench for HID lamps. *IEEE Trans. Ind. Appl.*, 43(5):1191–1198, 2007.

[56] J. Schwieger, M. Wolff, B. Baumann, F. Manders, and J. Suijker. Characterization of discharge arc flicker in high-intensity discharge lamps. *IEEE Trans. Ind. Appl.*, 51(3):2544–2547, 2015.

[57] T. D. Dreeben. Modelling of fluid-mechanical arc instability in pure-mercury HID lamps. *J. Phys. D: Appl. Phys.*, 41(14):144023, 2008.

[58] A. Okada, S. Morii, and S. Wada. Study of HID lamps with reduced acoustic resonances. *J. Illum. Eng. Inst. Japan*, 71(6):339–343, 1987.

[59] F. Afshar. Measurement of the onset time of acoustic resonance instabilities in HID lamps. *J. Illum. Eng. Soc.*, 3(3):229–242, 2007.

[60] W. W. Stoffels, F. van den Hout, G. M. W. Kroesen, M. Haverlag, and R. Keijser. Helical instability in metal halide lamps under micro and hypergravity conditions. *Appl. Phys. Lett.*, 88(9):091502, 2006.

[61] F. Afshar. The theory of acoustic resonance and acoustic instability in HID lamps. *J. Illum. Eng. Soc.*, 5(1):27–38, 2008.

[62] L. Chhun, P. Maussion, S. Bhosle, and G. Zissis. Characterization of acoustic resonance in a high pressure sodium lamp. *IEEE Trans. Ind. Appl.*, 47 (2):1071–1076, 2011.

[63] R. Schäfer and H.-P. Stormberg. Investigations on the fundamental longitudinal acoustic resonance of high pressure discharge lamps. *J. Appl. Phys.*, 53(5):3476–3480, 1982.

[64] H.-P. Stormberg and R. Schäfer. Excitation of acoustic instabilities in discharge lamps with pulsed supply voltage. *Light. Res. & Technol.*, 15(3): 127–132, 1983.

[65] W. Yan and S. Y. R. Hui. Ageing effects on the stability performance of small wattage metal-halide (MH) lamps. In *Proc. Appl. Power Electron. Conf.*, pages 978–983, Piscataway, 2004. IEEE.

[66] M. A. D. Costa, J. M. Alonso, J. García-García, J. Cardesín, and M. Rico-Secades. Acoustic resonance characterization of low-wattage metal-halide lamps under low-frequency square-waveform operation. *IEEE Trans. Power Electron.*, 22(3):735–743, 2007.

[67] R. Ruscassié, J.-B. B. Rouffet, S. Bhosle, G. Zissis, and C. Glaize. Defining acoustic resonances in dimmed HID lamps using a finite element model. In *Proc. Ind. Appl. Soc. Ann. Meeting*, pages 1588–1592, Piscataway, 2005. IEEE.

[68] S. D. Strickler and A. B. Stewart. Radial and azimuthal standing sound waves in a glow discharge. *Phys. Rev. Lett.*, 11(12):527–529, 1963.

[69] C. F. Gallo and J. E. Courtney. Acoustical resonances in modulated xenon and krypton compact arc lamps. *Appl. Opt.*, 6(5):939–940, 1967.

[70] H. L. Witting. Acoustic resonances in cylindrical high-pressure arc discharges. *J. Appl. Phys.*, 49(5):2680–2683, 1978.

[71] J. Hirsch, B. Baumann, M. Wolff, S. Bhosle, and R. V. Barrientos. Acoustic resonances in HID lamps: Model and measurement. *J. Phys. D: Appl. Phys.*, 43(23):234002, 2010.

[72] J. C. A. Antón, C. Blanco, F. J. Ferrero, A. Martín, N. Bordel, G. Zissis, and S. Bhosle. Acoustic resonance effects in high pressure sodium lamps. In *Proc. Ind. Appl. Soc. Ann. Meeting*, pages 479–483, Piscataway, 2007. IEEE.

[73] J. Olsen and W. P. Moskowitz. Optical measurement of acoustic resonance frequencies in HID lamps. In *Proc. Ind. Appl. Soc. Ann. Meeting*, pages 2263–2269, Piscataway, 1997. IEEE.

[74] J. Olsen and W. P. Moskowitz. Time resolved measurements of HID lamp acoustic frequency spectra. In *Proc. Ind. Appl. Soc. Ann. Meeting*, pages 2111–2116, Piscataway, 1998. IEEE.

[75] A. Burgio and D. Menniti. HID lamp acoustic resonance detection: A simple current-based method using sample-hold circuits. In *Proc. 10th Int. Conf. Environ. Elec. Eng.*, pages 1–4, Piscataway, 2011. IEEE.

[76] L. Chhun, P. Maussion, S. Bhosle, and G. Zissis. Interpolation modelling of acoustic resonance in high pressure sodium lamp. In *Proc. Ann. Conf. Ind. Electron. Soc.*, pages 1974–1979, Piscataway, 2008. IEEE.

[77] M. J. Jongerius, A. J. M. J. Ras, and Q. H. F. Vrehen. Optogalvanic detection of acoustic resonances in a high-pressure sodium discharge. *J. Appl. Phys.*, 55(7):2685–2692, 1984.

[78] J.-B. B. Rouffet, S. Bhosle, G. Zissis, and R. Ruscassié. Using COMSOL Multiphysics to modelling high pressure discharge lamps. In *Proc. Comsol Users Conf.*, Stockholm, 2006. COMSOL Multiphysics.

[79] S. Bhosle, J.-B. B. Rouffet, D. Buso, M. Aubès, and G. Zissis. Modeling of acoustic resonances in HID lamps - coupling between standing waves and arc bending. In *Proc. Ind. Appl. Soc. Ann. Meeting*, page 478, Piscataway, 2007. IEEE.

[80] A. Vágvölgyi, Á. Böröczki, S. Gyimóthy, and I. Sebestyén. Modeling acoustic resonance in high-pressure discharge lamp arc chambers. *Int. J. Appl. Electrom.*, 13(1):427–430, 2002.

[81] B. Baumann, M. Wolff, J. Hirsch, P. Antonis, S. Bhosle, and R. V. Barrientos. Finite element estimation of acoustical response functions in HID lamps. *J. Phys. D: Appl. Phys.*, 42(22):225209, 2009.

[82] T. D. Dreeben and G. P. Chini. Two-dimensional streaming flows in high-intensity discharge lamps. *Phys. Fluids*, 23(5):056101, 2011.

[83] A. Toumi, L. Chhun, S. Bhosle, G. Zissis, P. Maussion, and J. Hirsch. Acoustic resonance characterization and numerical model including acoustic streaming in an HPS lamp. In *Proc. Ind. Appl. Soc. Ann. Meeting*, pages 1–6, Piscataway, 2011. IEEE.

[84] A. Toumi, L. Chhun, S. Bhosle, G. Zissis, P. Maussion, B. Baumann, and M. Wolff. Acoustic resonance characterization and numerical model including acoustic streaming in an HPS lamp. *IEEE Trans. Ind. Appl.*, 49(3): 1154–1160, 2013.

[85] D. C. Fromm and J. Seehawer. Elimination of arc curvature by standing radial acoustic waves. *Light. Res. & Technol.*, 27(1):17–26, 1995.

[86] D. P. Y. Chang and W. Shyy. A study of three-dimensional natural convection in high-pressure mercury lamps - III. Arc centering by magnetic field. *Int. J. Heat Mass Trans.*, 35(8):1857–1864, 1992.

[87] A. A. Fridman. *Plasma chemistry*. Cambridge University Press, Cambridge, UK, 2008.

[88] A. A. Fridman and L. A. Kennedy. *Plasma physics and engineering*. CRC Press, Boca Raton, USA, 2nd edition, 2011.

[89] K. H. Kingdon and I. Langmuir. The removal of thorium from the surface of a thoriated tungsten filament by positive ion bombardment. *Phys. Rev.*, 22(2):148–160, 1923.

[90] M. N. Saha. LIII. Ionization in the solar chromosphere. *Phil. Mag. Ser. 6*, 40(238):472–488, 1920.

[91] K. Charrada, G. Zissis, and M. Aubès. Two-temperature, two-dimensional fluid modelling of mercury plasma in high-pressure lamps. *J. Phys. D: Appl. Phys.*, 29(9):2432–2438, 1996.

[92] H. Elloumi, E. Kindel, C. Schimke, and G. Zissis. Experimental investigation of deviations from local thermodynamic equilibrium in high-pressure mercury discharges. *J. Appl. Phys.*, 86(8):4134, 1999.

[93] J. J. Lowke. Calculated properties of vertical arcs stabilized by natural convection. *J. Appl. Phys.*, 50(1):147–157, 1979.

[94] M. B. Ben Hamida and K. Charrada. Application of a three-dimensional model for a study of the energy transfer of a high-pressure mercury horizontal lamp. *Phys. Plasmas*, 19(6):063504, 2012.

[95] M. Galvez. Ray-tracing model for radiation transport in three-dimensional LTE systems. *J. Phys. D: Appl. Phys.*, 38(17):3011–3015, 2005.

[96] J. O. Hirschfelder, C. F. Curtiss, and R. B. Bird. *Molecular theory of gases and liquids*. Wiley, London, UK, 1964.

[97] K. Charrada and G. Zissis. Spatio-temporal study of the deviations from thermal equilibrium in a high-pressure mercury plasma working under an AC power supply. *J. Phys. D: Appl. Phys.*, 33(8):968–976, 2000.

[98] P. Flesch and M. Neiger. Investigations on the influence of pressure, current and electrode gap in high-pressure mercury lamps. *J. Phys. D: Appl. Phys.*, 38(20):3792–3803, 2005.

[99] P. Flesch and M. Neiger. Numerical simulation of DC high-pressure discharge lamps including electrodes. *J. Phys. D: Appl. Phys.*, 35(14):1681–1694, 2002.

[100] P. Flesch and M. Neiger. Understanding anode and cathode behaviour in high-pressure discharge lamps. *J. Phys. D: Appl. Phys.*, 38(17):3098–3111, 2005.

[101] P. Flesch and M. Neiger. Time-dependent simulation of plasma and electrodes in high-intensity discharge lamps with different electrode shapes. *J. Phys. D: Appl. Phys.*, 36(7):849–860, 2003.

[102] R. Bötticher and W. Bötticher. Numerical modelling of arc attachment to cathodes of high-intensity discharge lamps. *J. Phys. D: Appl. Phys.*, 33(4): 367–374, 2000.

[103] R. Bötticher and W. Bötticher. Numerical modelling of a dynamic mode change of arc attachment to cathodes of high-intensity discharge lamps. *J. Phys. D: Appl. Phys.*, 34(7):1110–1115, 2001.

[104] R. Bötticher, W. Graser, and A. Kloss. Cathodic arc attachment in a HID model lamp during a current step. *J. Phys. D: Appl. Phys.*, 37(1):55–63, 2004.

[105] S. Lichtenberg, L. Dabringhausen, O. Langenscheidt, and J. Mentel. The plasma boundary layer of HID-cathodes: Modelling and numerical results. *J. Phys. D: Appl. Phys.*, 38(17):3112–3127, 2005.

[106] J. Wendelstorf. *Ab initio modelling of thermal plasma gas discharges (electric arcs)*. PhD thesis, Technische Universität Carolo-Wilhelmina zu Braunschweig, Braunschweig, Germany, 2000.

[107] L. Dabringhausen, O. Langenscheidt, S. Lichtenberg, M. Redwitz, and J. Mentel. Different modes of arc attachment at HID cathodes: Simulation and comparison with measurements. *J. Phys. D: Appl. Phys.*, 38(17): 3128–3142, 2005.

[108] R. Siegel and J. R. Howell. *Thermal radiation heat transfer*. Taylor & Francis, Washington, USA, 3rd edition, 1983.

[109] P. M. Morse and K. U. Ingard. *Theoretical acoustics*. McGraw-Hill, New York, USA, 1968.

[110] L. B. Kreuzer. The physics of signal generation and detection. In Y.-H. Pao, editor, *Optoacoustic spectroscopy and detection*, pages 1–25. Academic Press, New York, USA, 1977.

[111] B. Baumann, B. Kost, M. Wolff, and H. Groninga. Modeling and numerical investigation of photoacoustic resonators. In G. Petrone and G. Cammarata, editors, *Recent advances in modelling and simulation*, pages 17–38. I-Tech Education and Publishing, Vienna, Austria, 2008.

[112] B. Baumann, M. Wolff, B. Kost, and H. Groninga. Finite element calculation of photoacoustic signals. *Appl. Opt.*, 46(7):1120–1125, 2007.

[113] M. Schulz and K. U. Ingard. Acoustic kink instability in an argon discharge. *Phys. Fluids*, 10(5):1031–1036, 1967.

[114] M. Wiklund, R. Green, and M. Ohlin. Acoustofluidics 14: Applications of acoustic streaming in microfluidic devices. *Lab Chip*, 12(14):2438–2451, 2012.

[115] D. Sastrapradja. *Rayleigh streaming simulation using the vorticity transport equation*. PhD thesis, The Pennsylvania State University, Pennsylvania, USA, 2004.

[116] G. W. Swift. *Thermoacoustics: A unifying perspective for some engines and refrigerators*. Acoustical Society of America, Melville, USA, 2002.

[117] S. Boluriaan and P. J. Morris. Acoustic streaming: From Rayleigh to today. *Int. J. Aeroac.*, 2(3):255–292, 2003.

[118] L. Rayleigh. On the circulation of air observed in Kundt's tubes, and on some allied acoustical problems. *Phil. Trans. R. Soc. Lond.*, 175(1):1–21, 1884.

[119] M. Faraday. On a peculiar class of acoustical figures; and on certain forms assumed by groups of particles upon vibrating elastic surfaces. *Phil. Trans. R. Soc. Lond.*, 121:299–340, 1831.

[120] V. Dvořák. Ueber die akustische Anziehung und Abstossung. *Ann. Phys. Chem.*, 233(1):42–73, 1876.

[121] H. Mitome. The mechanism of generation of acoustic streaming. *Electron. Commun. Japan Part 3*, 81(10):1–8, 1998.

[122] W. L. Nyborg. Acoustic streaming due to attenuated plane waves. *J. Acoust. Soc. Am.*, 25(1):68–75, 1953.

[123] P. J. Westervelt. The theory of steady rotational flow generated by a sound field. *J. Acoust. Soc. Am.*, 25(1):60–67, 1953.

[124] H. Schlichting. Berechnung ebener periodischer Grenzschichtströmungen. *Phys. Z.*, 33(8):327–335, 1932.

[125] C. Eckart. Vortices and streams caused by sound waves. *Phys. Rev.*, 73(1): 68–76, 1948.

[126] D. Gedeon. DC gas flows in stirling and pulse tube cryocoolers. In R. G. Ross, editor, *Cryocoolers 9*, pages 385–392. Springer, Boston, USA, 1997.

[127] M. F. Hamilton, Y. A. Ilinskii, and E. A. Zabolotskaya. Acoustic streaming generated by standing waves in two-dimensional channels of arbitrary width. *J. Acoust. Soc. Am.*, 113(1):153–160, 2003.

[128] H. Bailliet, V. Gusev, R. Raspet, and R. A. Hiller. Acoustic streaming in closed thermoacoustic devices. *J. Acoust. Soc. Am.*, 110(4):1808–1821, 2001.

[129] P. Poćwiardowski. *Influence of acoustic streaming on electrochemical deposition*. PhD thesis, Gdansk University of Technology, Gdansk, Poland, 2003.

[130] H. Bruus. Acoustofluidics 2: Perturbation theory and ultrasound resonance modes. *Lab Chip*, 12(1):20–28, 2012.

[131] J. Lighthill. Acoustic streaming. *J. Sound Vib.*, 61(3):391–418, 1978.

[132] S. Temkin. *Elements of acoustics*. Wiley, New York, USA, 1981.

[133] K. Schuster and W. Matz. Über stationäre Strömungen im Kundtschen Rohr. *Akus. Zeits.*, 5:349–352, 1940.

[134] P. G. Drazin. *Introduction to hydrodynamic stability*. Cambridge University Press, Cambridge, UK, 2002.

[135] I. Rehberg. Phasenübergänge und hydrodynamische Instabilitäten. *Phys. unserer Zeit*, 12(5):131–137, 1981.

[136] H. Oertel. *Strömungsmechanische Instabilitäten*. Universitätsverlag, Karlsruhe, Germany, 2005.

[137] S. H. Strogatz. *Nonlinear dynamics and chaos: With applications to physics, biology, chemistry, and engineering*. Westview Press, New York, USA, 2008.

[138] M. Cross and H. Greenside. *Pattern formation and dynamics in nonequilibrium systems*. Cambridge University Press, Cambridge, UK, 2009.

[139] M. S. Benilov. Nonlinear surface heating of a plane sample and modes of current transfer to hot arc cathodes. *Phys. Rev. E*, 58(5):6480–6494, 1998.

[140] M. S. Benilov and M. D. Cunha. Bifurcation points in the theory of axially symmetric arc cathodes. *Phys. Rev. E*, 68(5):056407, 2003.

[141] P. G. C. Almeida, M. S. Benilov, M. D. Cunha, and M. J. Faria. Analysing bifurcations encountered in numerical modelling of current transfer to cathodes of DC glow and arc discharges. *J. Phys. D: Appl. Phys.*, 42(19):194010, 2009.

[142] G. Duffing. *Erzwungene Schwingungen bei veränderlicher Eigenfrequenz und ihre technische Bedeutung*, volume 41/42. Vieweg & Sohn, Braunschweig, Germany, 1918.

[143] K. Magnus, K. A. Popp, and W. Sextro. *Schwingungen: Physikalische Grundlagen und mathematische Behandlung von Schwingungen*. Springer Vieweg, Wiesbaden, Germany, 9th edition, 2013.

[144] T. Kalmár-Nagy and B. Balachandran. Forced harmonic vibration of a Duffing oscillator with linear viscous damping. In I. Kovacic and M. J. Brennan, editors, *The Duffing equation*, pages 139–174. John Wiley & Sons Inc., Chichester, UK, 2011.

[145] Philips Lighting Holding B.V. Material database: MASTERColour CDM-T Elite 35W/930 G12 1CT/12, 2012.

[146] L. Troudi, R. B. Ahmed, S. E. Aissi, K. Charrada, G. Zissis, and M. Sassi. Numerical modelling of a HgTlI discharge lamp: Transport coefficients and thermodynamic properties. *J. Phys. D: Appl. Phys.*, 37(4):610–622, 2004.

[147] S. Hashiguchi, K. Hatase, S. Mori, and K. Tachibana. Numerical simulation of metal-halide lamp using a time-dependent two-dimensional model. *J. Appl. Phys.*, 92(1):45–54, 2002.

[148] M. Westermeier, O. Langenscheidt, J. Reinelt, J. Mentel, and P. Awakowicz. Visualization of the gas-phase emitter effect of dysprosium in ceramic metal halide lamps. *IEEE Trans. Plasma Sci.*, 36(4):1176–1177, 2008.

[149] H. Wiesmann. *Zweidimensionale Simulation von Hochdruckgasentladungslampen unter Berücksichtigung der Elektrodenbereiche mit der Finite-Elemente-Methode*. Shaker, Aachen, Germany, 1997.

[150] J. Schwieger, B. Baumann, M. Wolff, F. Manders, and J. Suijker. Influence of thermal conductivity and plasma pressure on temperature distribution and acoustical eigenfrequencies of high-intensity discharge lamps. In *Proc. Comsol Users Conf.*, Stockholm, 2013. COMSOL Multiphysics.

[151] M. Gnybida, J. J. F. J. Janssen, J. van Dijk, J. Suijker, K. S. C. Peerenboom, A. J. Rijke, M. Gendre, and G. M. W. Kroesen. Numerical investigation on the replacement of mercury by indium iodide in high-intensity discharge lamps. *J. Phys. D: Appl. Phys.*, 47(12):125201, 2014.

[152] M. Born. An evaluation of the contribution of radiation diffusion to thermal conductivity in high-pressure discharge lamps from operating-voltage and wall-temperature measurements. *J. Phys. D: Appl. Phys.*, 32(8):876–885, 1999.

[153] National Bureau of Standards. Update of thermal conductivity and electrical resistivity of electrolytic iron, tungsten, and stainless steel, 1984. URL http://www.nist.gov/srm/upload/SP260-90.PDF. Last visited 15. Apr. 2016.

[154] G. K. White and M. L. Minges. Thermophysical properties of some key solids: An update. *Int. J. Thermophys.*, 18(5):1269–1327, 1997.

[155] R. Courant. Variational methods for the solution of problems of equilibrium and vibrations. *Bull. Amer. Math. Soc.*, 49(1):1–24, 1943.

[156] J. H. Argyris. Energy theorems and structural analysis. *Aircr. Eng. & Aerosp. Tech.*, 27(4):125–134, 1955.

[157] O. C. Zienkiewicz. *The finite element method in structural and continuum mechanics*. McGraw-Hill, New York, USA, 1967.

[158] S. V. Patankar. *Numerical heat transfer and fluid flow*. McGraw-Hill, New York, USA, 1980.

[159] K.-J. Bathe. *Finite element procedures for solids and structures: Nonlinear analysis*. MIT, Center for Advanced Engineering Study, Cambridge, UK, 1986.

[160] C.-D. Munz and T. Westermann. *Numerische Behandlung gewöhnlicher und partieller Differenzialgleichungen*. Springer, Berlin, Germany, 2012.

[161] C. Hirsch. *Numerical computation of internal and external flows: Fundamentals of computational fluid dynamics*. Butterworth-Heinemann, Burlington, USA, 2nd edition, 2007.

[162] A. Kuzmin, M. Luisier, and O. Schenk. Fast methods for computing selected elements of the green's function in massively parallel nanoelectronic device simulations. In F. Wolf, B. Mohr, and D. an Mey, editors, *Euro-Par 2013 Parallel Processing*, volume 8097, pages 533–544. Springer, Berlin, Germany, 2013.

[163] O. Schenk and K. Gärtner. Solving unsymmetric sparse systems of linear equations with PARDISO. *J. Future Gener. Comp. Sy.*, 20(3):475–487, 2004.

[164] COMSOL Multiphysics GmbH. Reference Manual 5.0, October 2014.

[165] Philips Lighting Holding B.V. MASTERColour CDM-T Elite 35W/930 G12 1CT/12, 2016. URL http://download.p4c.philips.com/lfb/f/fp-928185205131/fp-928185205131_pss_en_aa_001.pdf. Last visited 9. April 2016.

[166] K. Charrada, G. Zissis, and M. Stambouli. A study of the convective flow as a function of external parameters in high-pressure mercury lamps. *J. Phys. D: Appl. Phys.*, 29(3):753–760, 1996.

[167] P. Flesch and M. Neiger. Modeling of high pressure discharge lamps including electrodes. *IEEE Trans. Plasma Sci.*, 27(1):18–19, 1999.

[168] A. J. Flikweert, M. L. Beks, T. Nimalasuriya, G. M. W. Kroesen, J. A. M. van der Mullen, and W. W. Stoffels. 2-D Images of the metal-halide lamp obtained by experiment and model. *IEEE Trans. Plasma Sci.*, 36(4), 2008.

[169] P. Flesch and M. Neiger. Numerical investigation of time-dependent electrode-plasma interaction in commercial HID lamps. *IEEE Trans. Plasma Sci.*, 33(2):508–509, 2005.

[170] H.-P. Stormberg and R. Schäfer. Time-dependent behavior of high-pressure mercury discharges. *J. Appl. Phys.*, 54(8):4338–4347, 1983.

[171] D. P. Y. Chang, W. Shyy, and J. T. Dakin. A study of three-dimensional natural convection in high-pressure mercury lamps - I. Parametric variations with horizontal mounting. *Int. J. Heat Mass Trans.*, 33(3):483–493, 1990.

[172] D. P. Y. Chang and W. Shyy. Three-dimensional heat transfer and fluid flow in the modern discharge lamp. *Int. J. Heat Mass Trans.*, 34(7):1811–1822, 1991.

[173] K. C. Paul, T. Takemura, T. Hiramoto, M. Yoshioka, and T. Igarashi. Three-dimensional modeling of a direct current operated Hg-Ar lamp. *IEEE Trans. Plasma Sci.*, 34(2):254–262, 2006.

[174] W. Shyy and J. T. Dakin. Three-dimensional natural convection in a high-pressure mercury discharge lamp. *Int. Commun. Heat Mass Trans.*, 15(1): 51–58, 1988.

[175] W. Shyy and D. P. Y. Chang. Effects of convection and electric field on thermofluid transport in horizontal high-pressure mercury arcs. *J. Appl. Phys.*, 67(4):1712–1719, 1990.

[176] W. Shyy and D. P. Y. Chang. A study of three-dimensional natural convection in high-pressure mercury lamps - II. Wall temperature profiles and inclination angles. *Int. J. Heat Mass Trans.*, 33(3):495–506, 1990.

[177] M. B. Ben Hamida, H. Helali, Z. Araoud, and K. Charrada. Contrast between the vertical and horizontal mercury discharge lamps. *Phys. Plasmas*, 18(6):063506, 2011.

[178] Fujitsu Ltd. Data Sheet: FUJITSU CELSIUS R920 Workstation, 2012. URL http://sp.ts.fujitsu.com/dmsp/Publications/public/ds-CELSIUS-R920.pdf. Last visited 11. April 2016.

[179] Agilent Technologies, Inc. Agilent 33220A: 20 MHz Function/Arbitrary Waveform Generator User's Guide, 2007. URL http://www.bu.edu/eng/courses/ek307/documents/agilent33220.pdf. Last visited 9. April 2016.

[180] Wavetek Ltd. Maintenance Manual Model 29: 10 MHz DDS Function Generator, 1997.

[181] MT MedTech Engineering GmbH. DC-Hochspannungsverstärker DCU 2250 - 28 / DCU 750 Bedienungsanleitung.

[182] Yokogawa Electric Corporation. PZ4000 Power Analyzer User's Manual, 2000. URL http://www.electro-meters.com/Assets/pdf2_files/Yokogawa/Power_meters/PZ4000_pdfs/PZ4000_manual.pdf. Last visited 9. April 2016.

[183] IDS Imaging Development Systems GmbH. USB UI-1120SE, 2015. URL http://www.stemmer-imaging.co.uk/media/uploads/websites/documents/products/cameras/IDS/en_US-IDS-uEye-UI-1120-SE-USB-CMOS-HDR-cameras.pdf. Last visited 15. Apr. 2016.

[184] Thorlabs Inc. DET100A user guide: Large area Si biased detector, 2015. URL https://www.thorlabs.de/thorcat/13000/DET100A-Manual.pdf. Last visited 16. Apr. 2016.

[185] Tektronix, Inc. TDS1000B and TDS2000B Series Digital Storage Oscilloscopes: User Manual, 2003. URL http://www.sophphx.caltech.edu/Lab_Equipment/Tektronix_TDS1000_2000_User_Manual.pdf. Last visited 9. April 2016.

[186] K. Otani. The convection phenomena in the high pressure sodium lamp. *J. Light & Vis. Env.*, 7(2):1–6, 1983.

[187] A. Doehle, J. Hoffelner, H. Landes, and R. Lerch. Numerical simulation of high-intensity standing wave fields. In *Proc. Ultrasonics Symp.*, pages 543–546, Piscataway, 2002. IEEE.

[188] E. Ising. Beitrag zur Theorie des Ferromagnetismus. *Z. Phys.*, 31(1):253–258, 1925.

[189] G. Hunt. Buckling in space and time. *Nonlinear Dyn.*, 43(1-2):29–46, 2006.

[190] A. Pelissetto and E. Vicari. Critical phenomena and renormalization-group theory. *Phys. Rep.*, 368(6):549–727, 2002.

[191] W. Kaiser, R. P. Marques, and A. F. Correa. An alternative optical method for acoustic resonance detection in HID lamps. *IEEE Trans. Ind. Appl.*, 47 (3):1142–1148, 2011.